MICROCOPY RESOLUTION TEST CHART

BUREAU OF STANDARDS-1963-A

UNCLASSIFIED

REPORT DOCUMENTATION PAGE

Form Approved
OMB No. 0704-0188

1a REPORT SECURITY CLASSIFICATION UNCLASSIFIED	1b RESTRICTIVE MARKINGS
2a SECURITY CLASSIFICATION AUTHORITY	3 DISTRIBUTION / AVAILABILITY OF REPORT Approved for public release; distribution is unlimited.
2b DECLASSIFICATION / DOWNGRADING SCHEDULE	

4 PERFORMING ORGANIZATION REPORT NUMBER(S) ARL-TR-88-1	5 MONITORING ORGANIZATION REPORT NUMBER(S)

6a NAME OF PERFORMING ORGANIZATION Applied Research Laboratories	6b OFFICE SYMBOL (If applicable) ARL:UT	7a NAME OF MONITORING ORGANIZATION Office of Naval Research
6c ADDRESS (City, State, and ZIP Code) The University of Texas at Austin P. O. Box 8029 Austin, Texas 78713-8029		7b ADDRESS (City, State, and ZIP Code) Department of the Navy Arlington, Virginia 22217

8a NAME OF FUNDING / SPONSORING ORGANIZATION	8b OFFICE SYMBOL (If applicable)	9 PROCUREMENT INSTRUMENT IDENTIFICATION NUMBER N00014-86-K-0176

| 8c ADDRESS (City, State, and ZIP Code) | 10 SOURCE OF FUNDING NUMBERS |

PROGRAM ELEMENT NO	PROJECT NO	TASK NO	WORK UNIT ACCESSION NO

11 TITLE (Include Security Classification)

Nonlinear Optoacoustic Underwater Sound

12 PERSONAL AUTHOR(S)
Nicholas P. Chotiros

13a TYPE OF REPORT final report	13b TIME COVERED FROM 86-2-1 TO 87-7-31	14 DATE OF REPORT (Year, Month, Day) 88-1-11	15 PAGE COUNT 135

16 SUPPLEMENTARY NOTATION

17 COSATI CODES			18 SUBJECT TERMS (Continue on reverse if necessary and identify by block number)
FIELD	GROUP	SUB-GROUP	

19 ABSTRACT (Continue on reverse if necessary and identify by block number)
The objective of this study is to investigate nonlinear optoacoustic generation process-es. The initiative for this project arose out of the findings from a previous ONR funded project on the thermoacoustic sound source. A new theoretical model was developed, called the equilibrium blast model, which is based on the hydrodynamic equations of equilibrium. The conditions at the shock fronts are determined by the maximum entropy condition. The distribution of energy within the blast is assumed to be through thermal conduction. Experiments were carried out to test the model, and the model was also compared with experimental data. The experimental data showed that more than one process was involved. So far, three distinct blast processes have been identified, the weak blast, the thermal conduction limited equilibrium blast, and the emission limited equilibrium blast. The last is deserving of further study from a basic physics point of view and from an application standpoint.

20 DISTRIBUTION / AVAILABILITY OF ABSTRACT ☐ UNCLASSIFIED/UNLIMITED ☒ SAME AS RPT ☐ DTIC USERS	21 ABSTRACT SECURITY CLASSIFICATION UNCLASSIFIED
22a NAME OF RESPONSIBLE INDIVIDUAL Robert Culbertson	22b TELEPHONE (Include Area Code) 512-835-3316	22c OFFICE SYMBOL ASD

DD Form 1473, JUN 86 Previous editions are obsolete. SECURITY CLASSIFICATION OF THIS PAGE

UNCLASSIFIED

TABLE OF CONTENTS

LIST OF FIGURES

LIST OF TABLES

LIST OF SYMBOLS

α acoustic absorption coefficient

α_{oa} low intensity laser absorption coefficient

α_{ob} laser absorption coefficient in plasma cutoff regime

β coefficient of nonlinearity of water

β_k intensity correction factor for thermal conduction limited condition in the one-dimensional stage

β_k' intensity correction factor for thermal conduction limited condition in the two-dimensional stage

β_u intensity correction factor for two-dimensional expansion

C_a thermoacoustic conversion constant, determined by physical constants, including specific heat, thermal expansion coefficient, etc.

C_c pressure coupling coefficient from air blast to solid surface (Pirri's model)

c_o velocity of small amplitude sound in the undisturbed medium

c_{wo} velocity of small amplitude sound in the undisturbed water

c_v specific heat at constant volume

c_{wv} specific heat at constant volume of water

D front velocity

D_a diffraction loss, determined by the geometry and orientation of laser beam, the laser beamwidth, and absorption length (Section III)

D_a velocity of air blast front (Section II)

D_{ao} velocity of air blast front in the one-dimensional stage

D_{bo} velocity of blast front in the one-dimensional stage (Pirri's model)

D_u	velocity of underwater blast front
D_{uo}	velocity of underwater blast front in the one-dimensional stage
d_o	diameter of laser beam
e	electron charge
E_b	electron band gap of water
E_p	laser photon energy
ε_o	permittivity
ε_{sh}	latent of vaporization of water at ambient density and pressure
ε_{sv}	latent heat of vaporization of water at constant volume and temperature
γ	ratio of specific heats
γ_a	ratio of specific heats of air
γ_s	ratio of specific heats of steam in the gas regime
γ_w	adiabatic exponent of water
h	height of front above interface
h_a	distance traveled by the air front
h_g	enthalpy density rate required in the blast interior to maintain pressure equilibrium
h_g'	initial enthalpy density rate entering the blast interior from both fronts
h_u	distance traveled by the underwater front
η	coefficient of expansion
η_a	coefficient of expansion of air behind the air blast
η_s	coefficient of expansion of steam behind the underwater front
η_w	coefficient of expansion of water behind the underwater blast
I_a	laser intensity driving the air blast front

I_o	laser intensity
I_{oa}	laser intensity driving the air blast front in the one-dimensional stage
I_{KB}	impulse of a shock wave according to the Kirkwood-Bethe model
I_g	laser intensity required to maintain pressure equilibrium
I_{og}	laser intensity required to maintain pressure equilibrium in the interior in the one-dimensional stage
I_{ou}	laser intensity driving the underwater blast front in the one-dimensional stage
I_{tot}	total laser intensity
I_u	laser intensity driving the underwater blast front
k	thermal conductivity (Section II)
k	acoustic wave number (Section III)
k_o	*constant component of thermal conductivity*
k_1	linear temperature component of thermal conductivity
λ	laser wavelength
λ_o	initial characteristic length of a shock pulse
m	molecular weight
m_a	molecular weight of air
m_e	electron mass
m_s	molecular weight of steam
μ_o	permeability
N	carrier density
N_{ce}	available carrier density
n	number of independent resolvable areas in a laser spot
p	pressure

$p(E_o,n)$ probability that a laser spot with mean energy density E_o and n independent resolvable areas has at least one resolvable area with energy density greater than the ionization threshold E_t

$P(\omega)$ energy density spectrum of acoustic shock

p_{ao} pressure behind the one-dimensional front in air

p_{bo} pressure behind blast front in the one-dimensional stage (Pirri's model)

p_{go} interior pressure of blast

p_m peak acoustic pressure of shock wave

p_o ambient pressure of undisturbed medium

p_s pressure at solid surface (Pirri's model)

p_{so} pressure on the solid surface in the one-dimensional stage (Section II.A)

p_{so} steam pressure behind the front in the one-dimensional stage (Section II.B)

p_{wo} water pressure behind the front in the one-dimensional stage

p_u pressure behind the underwater front in the one-dimensional stage

p_o' isentropic pressure

Q volumetric radiation source density

q independent parameter of concentric ellipsoids

R universal gas constant (Section II)

R range from sound source to point of observation (Section III)

R_c radius of curvature

R_o initial radius of curvature of a shock front

r radial coordinate of point on constant temperature ellipsoid (Section II)

r_o	range from optoacoustic source
r	position vector of point of observation
ρ	density
ρ_o	density of unperturbed medium (Pirri's model)
ρ_{ag}	density of the air in the blast interior at equilibrium
ρ_{oa}	density of the unperturbed air
ρ_{ow}	density of the unperturbed water
ρ_{sv}	interpolated density of steam at ambient temperature and pressure assuming perfect gas behavior
ρ_{ug}	density of the water or steam in the blast interior at equilibrium
S	specific entropy
s	asymptotic power of the time dependence of the front velocities
s	position vector of a point on the interface
t	time after first arrival of laser pulse
t_e	1/e life of the electrons in the higher energy state
t_{ob}	time to achieve complete ionization after plasma cutoff
T	temperature
T_a	temperature behind air front
T_{ao}	temperature behind air front in the one-dimensional stage
T_{bo}	temperature behind blast front in the one-dimensional stage (Pirri's model)
T_s	steam temperature
T_{sh}	interpolated steam temperature at ambient pressure and density assuming perfect gas behavior
T_o'	isentropic temperature
t_{oa}	time required to achieve the plasma cutoff

T_u	temperature behind underwater front
T_{uo}	temperature behind underwater front in the one-dimensional stage
τ	1/e time constant of a shock wave
τ_k	start time of thermal conduction limited condition in the one-dimensional stage
τ_p	duration of laser pulse
τ_u	time constant for the combined thermal conduction and expansion effects
τ_{2D}	start time of two-dimensional stage
u	particle velocity relative to front
$W(\omega)$	the Fourier transform of the laser power function
W_a	weighting factor related to the relative energy consumption rate of the air front
W_{ao}	weighting factor W_a in the one-dimensional stage
W_u	weighting factor related to the relative energy consumption rate of the underwater front
W_{uo}	weighting factor W_u in the one-dimensional stage
ω	specific enthalpy (Section II)
ω	angular frequency (Section III)
ω_a	specific enthalpy of air exiting the air front
ω_{ag}	specific enthalpy of air in the blast interior at equilibrium
ω_l	laser frequency
ω_p	plasma frequency
ω_u	specific enthalpy of water or steam exiting the underwater front
ω_{ug}	specific enthalpy of water or steam in the blast interior at equilibrium

ω_w	specific enthalpy of water in the liquid regime
ω_s	specific enthalpy of steam in the gas regime
x	vertical distance
x_c	critical thickness for thermal conduction limited condition
Y	electron yield per photon
z	vertical coordinate of a point on a constant temperature ellipsoid

ACKNOWLEDGMENTS

I. INTRODUCTION

Applied Research Laboratories, The University of Texas at Austin (ARL:UT), has been conducting research under Contracts N00014-82-K-0425 and N00014-86-K-0176 to investigate both theoretically and experimentally the basic properties of the optoacoustic sound source. This report pertains to the latter contract.

Several mechanisms of sound generation may be identified under the general title of optoacoustic sound sources. The simplest one is the thermoacoustic process which employs direct heating of the acoustic medium to produce a controlled local thermal expansion which in turn generates sound waves.[1] The thermal energy is delivered by a laser beam to the water surface without mechanical contact. A moving thermoacoustic source may be obtained by deflecting the laser beam with a rotating mirror, causing the position of the thermal sound source to change as a function of time. This allows the signal to be Doppler shifted much more than it can be with conventional sound projectors, which have to be in physical contact with the acoustic medium. The study was pursued from two directions, the fundamental physical processes and the feasibility for sonar applications. The results of the investigations have been reported.[2,3,4]

Although it had been speculated that the moving thermoacoustic source may be more efficient than the stationary source, the feasibility study found the efficiency upperbounds to be identical for both cases. The upperbounds were found to be constrained by the physical properties of the medium and the energy output of the thermal source. Furthermore, the conversion efficiency upperbounds were found to be too low to be useful at sonar frequencies at the levels of laser energy that are considered to be practical.[3] To obtain higher efficiencies without requiring impractically high levels of laser energy, the focus of the study has shifted under Contract N00014-86-K-0176 to nonlinear optoacoustic processes. Nonlinear processes have been found experimentally to be more efficient,[5] but they are not well understood.

1

There have been a number of publications on this topic. A large proportion of the reported works have been for cases where most of the energy is spread over several megahertz.[6,7] The results reported by Hickman[8] were in the range of sonar frequencies but they were very sparse, and the experimental conditions appeared to be imprecise. The most extensive set of results were reported by Maccabee and Bell.[9,10,11,12] Their data covered a wide range of operating conditions. Their results showed significant finite amplitude distortion and extra attenuation of the acoustic pressure. They used a "rocket" model to estimate the reactive pressure on the water surface, and linear superposition to construct the acoustic pressure signal; they have found that the model predictions are not consistent with the experimental results.[12] More suitable blast models are those of A. N. Pirri[13,14] who successfully used them to model the momentum transfer between a high power laser blast on the surface of a solid. Unlike some models that have been reported that are specific to solid surfaces,[15] the Pirri models are general enough to be adapted for laser induced blasts over water.

The theory of the nonlinear optoacoustic generation process has only been partially analyzed in existing publications. Wu[16] made a theoretical analysis using linear superposition and a model similar to Pirri's model but without any experimental verification. Lyamshev and Naugol'nykh[17] produced a similar, but one-dimensional, model. Feiock and Goodwin[18] also produced a one-dimensional model which included a numerical solution of the pressure wave. In all cases, they ignored backscatter and absorption of the laser energy by the water vapor, and the effects of the deformation of the water surface.

Sigrist and Kneubuhl[19] made excellent experimental measurements of the axial acoustic pressure in the nearfield but did not proceed beyond the linear thermoacoustic model of Hu.[20] Their equipment did not allow the measurement of beam patterns, and therefore it was not possible to analyze the spatial character of the sound source. Maccabee and Bell[9,10] have made extensive experimental studies but they have not gone beyond the "rocket" model and linear superposition in their analysis.[12] Moreover, it is not possible to bring the experimental results of Maccabee and Bell and the available theoretical

2

analyses together in a satisfactory manner because of a number of conflicts including the following: (1) most of the results were in the form of peak pressure measurements which can be very misleading because the peak pressure of a wideband signal is critically dependent on the response characteristics of the receiving system, and (2) the experimental results obtained in the nearfield of the source are extremely sensitive to position; consequently, they were very variable.

Finally, the transition from the linear thermal expansion process to the nonlinear evaporative processes appears not to have been studied at all. The transition appears to be caused by a drastic change in the absorption coefficient of the optical radiation. In the linear region of operation, the absorption coefficient for 1.06 μm infrared radiation has been measured[21] to be in the region of 15 m-1, but in the nonlinear region it is reported[19] to be 9×10^4 m-1. Without this change in the absorption coefficient, the evaporative processes would not be observable at the currently reported values of optical energy density.

The objective of this study is to bridge some of these gaps in the current understanding of the nonlinear optoacoustic generation processes. At the outset of this study, it was proposed that the work be approached in the following sequence.

(1) The blast model should be developed as far as possible within the linear propagation regime of the acoustic signal. The development was actually completed under the previous contract.[22] The validity of this approach will be limited to relatively low laser intensities. The main advantage in this approach is that it would allow linear superposition to be used in the reconstruction of the sound field and would avoid problems associated with nonlinear propagation.

(2) The model will then be extended to include nonlinear acoustic propagation effects. This will allow the effects of higher laser intensities to be analyzed. The extended model will be tested under controlled conditions to obtain an evaluation of its accuracy. The results obtained will be

complementary to those of Maccabee and Bell.

(3) After the model has been verified against experimental results, a feasibility study will be made for sonar applications, in terms of energy conversion efficiency, source levels that can be realistically achieved, and range penetration capabilities.

As it turned out, the extension of the model to include nonlinear propagation effects produced a completely new blast model. This work is described in Section II. The model predictions were compared with experimental results, as described in Section III. When attempts were made to test the model at very high laser intensities, the experimental results obtained were quite unexpected. Certainly, they could not be explained by the blast model. Indeed, the acoustic output measured was significantly higher than that predicted by the blast model. Therefore, at this point, the project deviated from the stated course. A new optoacoustic generation process was hypothesized. It was deduced that an essential ingredient of the hypothesis is plasma formation. To investigate the process of plasma formation, an experiment was carried out to measure the photoconductivity of water in the presence of 1.06μ laser illumination to infer the characteristics of the carriers generated. The results of this experiment are shown in Section IV. Final conclusions are drawn in Section V.

II. THEORY

A mathematical model of the explosive reaction that leads to the generation of sound in water will be derived. The reaction is not self-starting. It is necessary to assume that there exists a mechanism to absorb the laser energy into the gases that drive the blast. In the case of laser irradiation of a solid surface, the surface must be sufficiently absorptive to cause local vaporization, the formation of a thin layer of absorptive vapor above the surface. This layer then expands explosively as it absorbs increasing amounts of laser energy. In the case of the air-water interface, it must be assumed that a mechanism exists that allows the laser energy to generate a thin film of an absorptive substance from which the blast is launched. This mechanism is not well understood; it is believed to involve dielectric breakdown of the water molecules. Let us for the moment assume that a starter mechanism exists and proceed to analyze the basic dynamics of the blast process. We will return to the starter mechanism later.

A. Pirri's Blast Model

In the previous project, a blast model developed by Pirri[14] was applied to the problem. For completeness, this model will be reviewed briefly. The model was originally developed to predict the impulse imparted by a laser pulse to a solid surface. Pirri's model treats the explosive reaction, or blast process, in two stages as shown in Fig. 1. The first stage is the one-dimensional expansion stage in which the blast expands outward from the surface. Since the gases within the blast volume are highly energized, and since the blast gases are in a state of dynamic equilibrium, it is fair to expect that the pressure and temperature within the expanding blast volume are approximately uniform. With this constraint, the velocity D_{bo} of the blast front in the one-dimensional stage can be shown to be given by[14]

$$D_{bo} = [\, 2(\gamma^2 - 1)I_o / \rho_o \,]^{1/3} \; . \tag{1}$$

and the pressure p_{bo} behind the front is given by[14]

5

LASER BEAM

AIR

BLAST FRONT

SOLID

FIRST STAGE

LASER BEAM

BLAST
FRONT

AIR

SOLID

SECOND STAGE
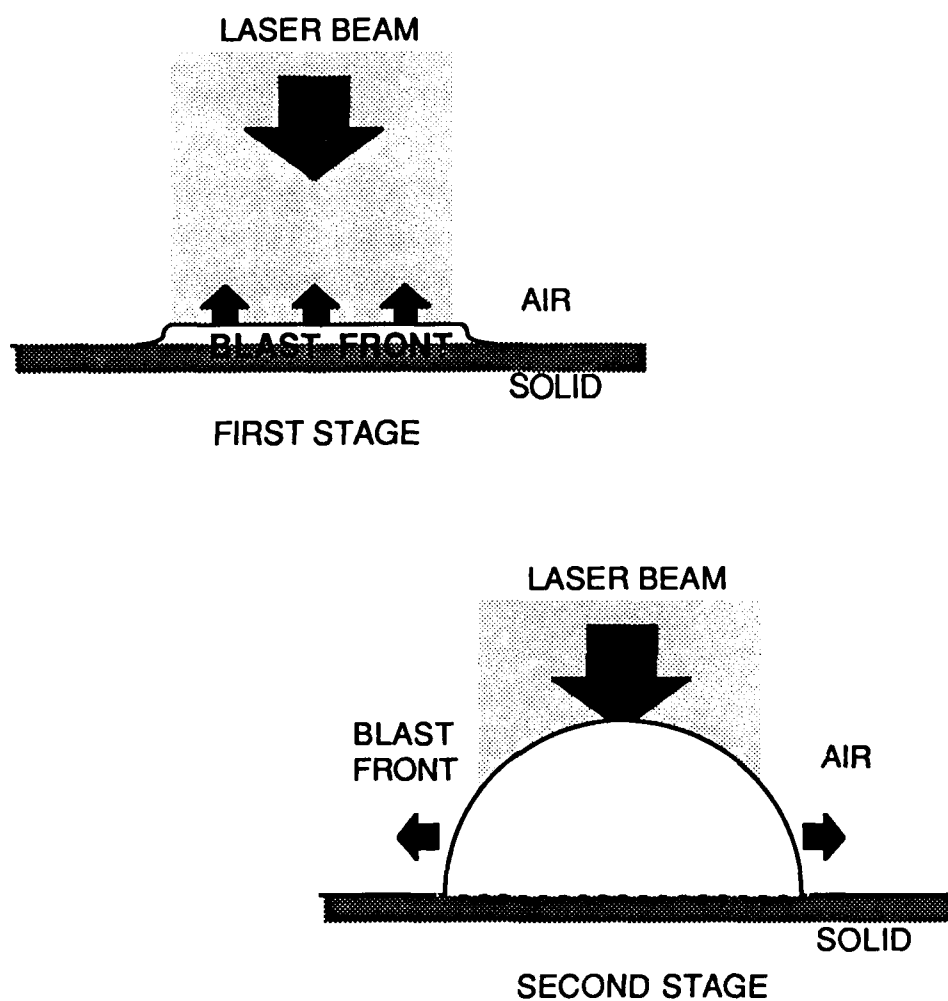
FIGURE 1
PIRRI'S BLAST MODEL

$$p_{bo} = \rho_o D_{bo}{}^2 / (\gamma + 1) \; , \tag{2}$$

where I_o is the laser intensity, ρ_o is the density of the surrounding undisturbed medium at rest and γ the ratio of specific heats of the blast gas. Using the gas equation, the blast temperature T_{bo} in $^{\circ}K$ is given by

$$T_{bo} = T_o(1 + (p_{bo}/p_o)) \; , \tag{3}$$

where T_o is the ambient temperature in $^{\circ}K$ and p_o the ambient pressure.

The pressure at the solid surface p_{so} is related to the pressure behind the blast wavefront by a coupling coefficient C_c,

$$p_{so} = C_c p_{bo} \; , \tag{4}$$

where C_c is given by[14]

$$C_c = [(\gamma + 1)/ 2 \gamma]^{2\gamma/(\gamma-1)} \; . \tag{5}$$

The one-dimensional stage terminates when the height of the blast is approximately equal to its width. At this point the blast enters the two-dimensional stage. The time τ_{2D} at which the changeover takes place is, according to Pirri, given by[14]

$$\tau_{2D} = \int_o^{d_o} (1/D) \; dh \; , \tag{6}$$

where D is the velocity of the blast front and d_o the diameter of the blast front. While the laser beam is on, D is equal to D_{bo}, in which case τ_{2D} is given by

$$\tau_{2D} = d_o/D_{bo} \; . \tag{7}$$

Should the laser pulse cease before the displacement h is equal to d_o, the blast will still expand in a one-dimensional mode but at a declining rate and the surface pressure $p_s(t)$ will decline according to[14]

$$p_s(t) = p_{so} (t/\tau_p)^{-2/3} \qquad ; \quad \text{for } \tau_{2D} > t > \tau_p . \tag{8}$$

In this case, τ_{2D} is given by

$$\tau_{2D} = \tau_{2D}[2/(3\, D_{bo}{}^{3/2}\, \tau_p{}^{1/2})][(\, d_o{}^{3/2} - (\, D_{bo}\, \tau_p\,)^{3/2}] + \tau_p . \tag{9}$$

The second stage is the two-dimensional expansion phase of the blast in which the pressure decays rapidly as the blast area expands. A cylindrically expanding blast is assumed. The pressure $p_s(t)$ is given by[14]

$$p_s(t) = p_s(\tau_{2D}) (\tau_{2D}/t) \qquad ; \quad \text{for } t > \tau_{2D} . \tag{10}$$

As can be seen in the above equations, the highest pressures are generated in the one-dimensional stage. Case studies of the one-dimensional stage of Pirri's blast model are shown in Table I. Three representative cases are shown. In each case, the laser pulse is modeled as having a peak power of 4.5 MW and a pulse length of 0.15 µs, giving a total of energy of 0.7 J. The laser beam is focused onto a spot on a solid surface. The three cases shown correspond to three different spot sizes, and hence different laser intensities. While the results shown in Table I do not signify any remarkable differences between the three cases, it will be shown in subsequent sections that these three cases give very different results for the reaction at the air-water interface, and give some insight to the processes involved. In addition, these cases also match the conditions of the accompanying experimental studies of laser sound generation in water, the results of which will also be presented.

First of all, it is seen that not all the laser energy is used to drive the blast. According to Pirri's theory, once the blast reaches the second stage, further laser energy arrivals will not influence the blast pressure at the solid surface, which at that point will begin its decline. Thus, the ratio between τ_{2D} and the

8

TABLE I

CASE STUDIES OF PIRRI'S MODEL FOR THE AIR-SOLID INTERFACE

CONDITIONS

Ambient temperature	°C	25		
Incident laser power	W	4.5E+6		
Pulse duration	s	1.50E-07		
Energy	J	0.7		

CASE		1	2	3
Spot diameter	m	3.2E-3	6.6E-4	1.7E-4
Spot area	m²	8.0E-6	3.4E-7	2.3E-8
Incident intensity	W/m²	5.6E+11	1.3E+13	2.0E+14
Energy density	MJ/m²	0.03	1.0	14

AIR BLAST OVER RIGID SOLID

Medium		Solid	Air	Solid	Air	Solid	Air
Molecular weight	g mole	∞	32	∞	32	∞	32
Medium density	kg/m³	∞	1.31	∞	1.31	∞	1.31
Ratio of specific heats		N/A	1.4	N/A	1.4	N/A	1.4
Blast velocity	m/s	N/A	1.8E+4	N/A	2.6E+4	N/A	3.6E+4
Blast pressure	Pa	5.9E+7	1.7E+8	1.2E+8	3.6E+8	2.4E+8	7.0E+8
Blast temperature	°C	N/A	5.2E+5	N/A	1.1E+6	N/A	2.1E+6
τ_{2D} $(\tau_p > \tau_{2D})$	s	N/A	1.8E-7	N/A	2.6E-8	N/A	4.7E-9
τ_{2D}	s	N/A	2.1E-7	N/A	2.6E-8	N/A	4.7E-9
Blast front displacement at τ_{2D}	m	N/A	3.1E-3	N/A	6.6E-4	N/A	1.7E-4
Proportion of useful energy	%	100		17.2		3.16	

laser pulse length τ_p may be taken as an approximate indication of the useful fraction of the laser energy. It is seen that, while 100% of the energy is utilized in case 1, in cases 2 and 3 only small percentages of the laser energy, 17.2% and 3.16%, respectively, are effectively utilized. This is because, in cases 2 and 3, the duration of the first stage of the blast τ_{2D} is very short compared to the laser pulse length. The computed blast pressures, velocities, and temperatures are also shown. It can be seen that the computed blast velocities are all supersonic. The blast pressures and the pressures transmitted to the solid surface are all estimated to be in excess of 100 atmospheres (1 atmosphere = 10^5 Pa). The values are most extreme in the third case, where the laser spot is smallest and the laser intensity is highest. The computed temperatures of the blast gases range from 0.52 to 2.1 million $^{\circ}$C.

In a preliminary study,[23] this model was applied with little modification to the optoacoustic sound generation process. It was assumed that, for the most significant part of the blast, the water surface remained unperturbed and therefore, for practical purposes, behaved as a solid surface. The surface pressure that the model predicted would form a distributed source function of the underwater acoustic signal. The acoustic signal was then constructed by linear superposition of the Green's function from each elemental source point. Although it was a very crude model, it gave very reasonable results. The following is a more rigorous treatment of the process of optoacoustic sound generation, starting from the basic hydrodynamic principles.

B.   Blast Model Development for the Air-Water Interface

To overcome the shortcomings of the Pirri model, a new model will be derived from the basic hydrodynamic equations. Let us start by considering the very beginning of an optically induced reaction at the air-water interface. At the very start of the reaction, any activity would be confined to a thin layer whose vertical dimension is expected to be on the order of a wavelength of the laser light or the size of a water molecule, whichever is greater. In comparison, the laser beam would be much wider; therefore, the initial process may be

considered as a one-dimensional process. It is postulated that there is a pressure buildup due to thermal absorption. Therefore, there must be a pressure discontinuity propagating into the air counter-balanced by a pressure front propagating into the water. Initially, this may be considered as a one-dimensional process. When the vertical separation of the two fronts reaches a value where it begins to significantly affect the course of the reaction, then the one-dimensional assumption will break down. The division of the evolution into one- and two-dimensional stages is a useful simplification that is helpful in gaining an insight into the problem.

The new model for the one-dimensional stage, as shown in Fig. 2, shows a discontinuity front traveling into the air and another into the water from the interface. For equilibrium, the pressures behind the two fronts must be equal. At this point, the two separate fronts are launched outward from the interface. The fronts will be called blast fronts or waves, since they are driven by hot gases which are energized by the laser beam.

First of all, consider the equations governing each front. The hydrodynamic equations governing a well defined planar discontinuity can be found in a number of well-known texts.[23,24] They are as follows.

The conservation of mass equation,

$$\rho u = \rho_o D, \tag{11}$$

the momentum equation,

$$p + \rho u^2 = \rho_o D^2, \tag{12}$$

and the energy equation,

$$I_o/(\rho_o D) = \omega + 0.5u^2 - 0.5D^2 . \tag{13}$$

LASER BEAM
INTENSITY : I_{tot}

AIR
DENSITY : ρ_{oa}

AIR FRONT
VELOCITY : D_{ao}

AIR/WATER MIXTURE
PRESSURE : P_g

UNDERWATER
FRONT
VELOCITY : D_{uo}
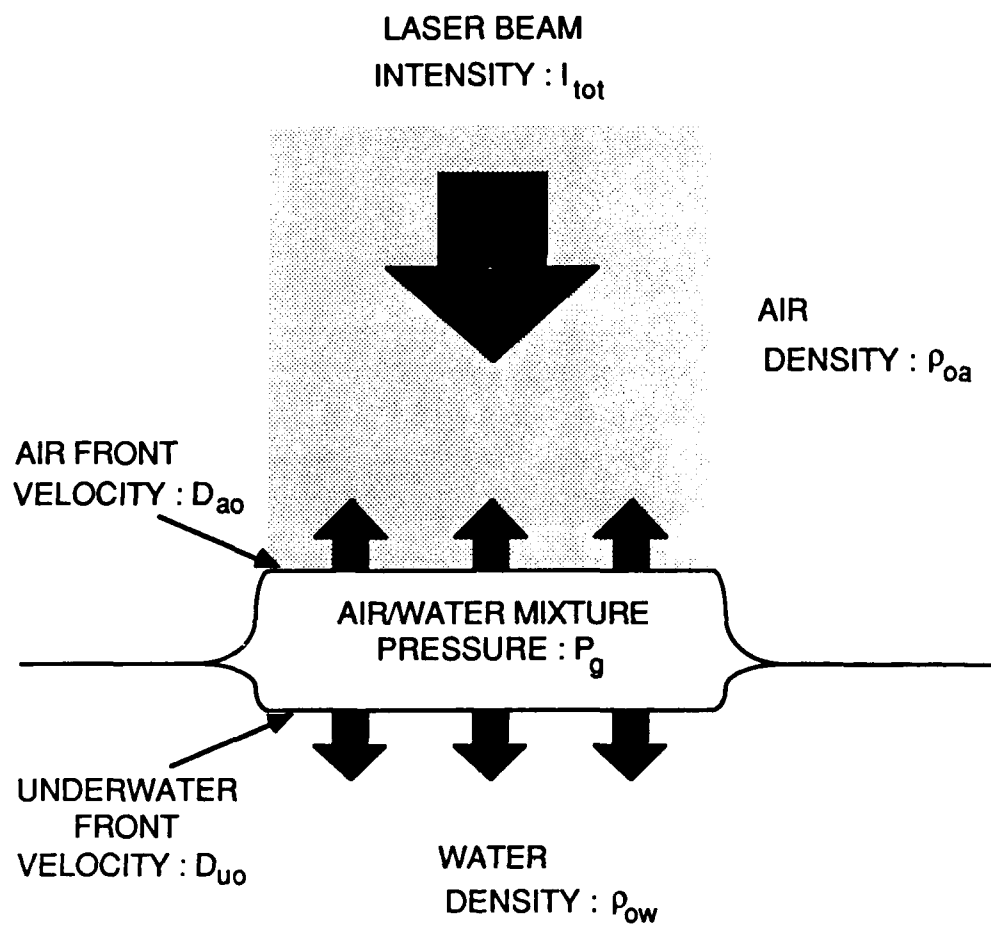
WATER
DENSITY : ρ_{ow}

FIGURE 2
ONE-DIMENSIONAL BLAST AT THE WATER SURFACE

12

where p is the excess pressure above the ambient pressure p_o, ρ and u are the density and particle velocity of the gas behind the front, u is measured relative to the moving front, I_o is the power supplied to the planar discontinuity per unit area, ρ_o is the density of the unperturbed fluid (gas or liquid) which is assumed to be at rest, D is the velocity of the front relative to the unperturbed fluid, and ω is the specific enthalpy increase.

1.   Maximum Entropy Condition

    For a gas, the specific enthalpy ω increase is of the form

$$\omega = (R/m)(T - T_o)\gamma/((\gamma - 1)$$

$$= (p + p_o)\gamma/((\gamma - 1)\rho) - p_o\gamma/((\gamma - 1)\rho_o), \tag{14}$$

where T is the gas temperature, T_o and p_o the ambient temperature and pressure, R the universal gas constant, and m the molecular weight.

If it can be assumed that $p \gg p_o$, then it is seen that p_o may be neglected. Eliminating D and u from the above equations, Raizer[23] showed that a simple solution of the pressure may be found in terms of the laser intensity I_o, the physical constants ρ_o and γ, and the expansion coefficient η. Giving the pressure term p subscripts "bo" to indicate that it pertains to the pressure behind the blast front in the one-dimensional stage, the solution is given by

$$p_{bo} \approx [(2(1-\eta)^{1/2} \rho_o^{1/2} I_o) /(\eta(\gamma+1)/(\gamma-1) - 1)]^{2/3} , \tag{15}$$

where η is defined as

$$\eta = \rho_o/\rho . \tag{16}$$

13

The expansion coefficient η needs to be addressed at some length. There is nothing in the above equations that can determine the value of η. According to Raizer[23] and Cole,[24] the value is determined by the Chapman-Jouguet condition. While Chapman[25] simply assumed that the front must travel at the minimum velocity consistent with the above equations, Jouguet[26] postulated that the front must travel at a velocity equal to $c_o + (D-u)$, that is, the velocity of small amplitude waves c_o plus the absolute particle velocity $(D-u)$. Both conditions are equivalent and lead to identical results. There are a number of physical arguments that can be made in support of the Chapman-Jouguet condition.

In general, the value of η may be explained by the principle of increasing entropy, a corollary of the second law of thermodynamics. Since the front is a discontinuity, the thermodynamic state of the fluid, as it passes through the discontinuity, must for a very brief moment be indeterminate. That is, it can go through the full range of possible states. Since the principle of increasing entropy only allows transitions to states with higher entropy, it follows that the final state will be the one with the maximum entropy. Therefore, the fluid emerges from the discontinuity at the maximum entropy allowed by the governing equations.

The maximum entropy condition may be simply found by taking the partial derivative of the entropy S with respect to η and setting $\partial S/\partial \eta$ equal to zero. For a gas initially at pressure p_o and density ρ_o, and arriving at the state given by $p+p_o$ and η, the entropy increase may be computed by considering the transition to be in two stages: an isentropic expansion to p_o' and η followed by a constant volume heating to the final state. From the adiabatic gas equation, the pressure p_o' is given by

$$p_o' = p_o \, \eta^{-\gamma} \tag{17}$$

at an absolute temperature T_o' of

$$T_o' = (p_o'\eta/\rho_o)(m/R) \quad , \tag{18}$$

where m is the molecular weight of the gas, and R the universal gas constant. In heating at constant volume from pressure p_o' to $p+p_o$, the final temperature T is given by

$$T = ((p_{bo}+p_o)\eta/\rho_o)(m/R) \quad . \tag{19}$$

The entropy increase S is given by

$$S = {}_{T_o}\!\!\int^T c_v / T \; dT$$

$$= c_v (\ln(T) - \ln(T_o')) \quad , \tag{20}$$

where c_v is the specific heat at constant volume. Substituting for T_o' and T from the above equations and differentiating with respect to η, the result is

$$\partial S/\partial\eta = c_v((\partial T/\partial\eta) /T) - (\partial T_o'/\partial\eta) /T_o'))$$

$$= (c_v/\eta)(\gamma + (\partial p/\partial\eta)\eta/(p_{bo}+p_o)) \quad . \tag{21}$$

Substituting for p_{bo} from Eq. (15), carrying out the partial derivative $\partial p/\partial\eta$, and then setting $\partial S/\partial\eta=0$, the value of η at the maximum entropy condition may be found. Cole[24] has shown that, where the pressure is large compared to the atmospheric pressure, the condition $\partial S/\partial\eta = 0$ is equivalent to the Chapman-Jouguet condition. Thus, the Chapman-Jouguet condition may be justified on the basis of the laws of thermodynamics. According to Raizer, the Chapman-Jouguet condition for a gas occurs when

$$\eta = \gamma/(\gamma+1) \quad . \tag{22}$$

2. Blast Fronts at the Air-Water Interface

Let us now return to the fundamental equations, Eqs. (11)-(13), and derive the solutions for the air-water interface without neglecting the ambient pressure term. Water, however, is far from being a perfect gas; therefore, it is necessary to deal with certain complications in the formulation of its pressure-density-temperature relationships.

It is not possible to give a complete description of the thermodynamic behavior of water through simple analytical formulae. For the purposes of this study, we will consider two idealized regimes, the gas regime and the liquid regime, which will be defined below. These two regimes were found to be adequate most of the time. Beyond and between these two regimes, there is a vast area of state space that will be dealt with only as the need arises. The criteria for the gas regime were found empirically by searching the state space as contained in the steam tables.[28] It was found that in certain regions of the state space, steam behaved very much like a perfect gas, i.e., its properties *differed little from that of a perfect gas of the same molecular weight.* The idealized liquid regime is an adaption of the state equations for high temperatures given by Cole. The criteria for the liquid regime were also found empirically by searching the steam tables. The pressure and temperature ranges of the available steam tables are somewhat limited, and beyond these ranges one can only extrapolate.

In the following, the equations for the pressure and front velocity will be rederived *without neglecting the ambient pressure terms,* and the analysis is extended to include the possibility of superheated steam or liquid water as a blast fluid.

a. Gas Regime

In the gas regime, all of the water absorbed by the blast is converted into superheated steam. The blast absorbs water at the rate given by

the velocity of the underwater front. In this regime, the specific enthalpy term in Eq. (13) may be approximated by

$$\omega = \omega_s = (R/m_s)(T_s - T_{sh})\gamma_s/(\gamma_s - 1) + \epsilon_{sh}$$

$$= (p_{so} + p_o)\gamma_s/((\gamma_s - 1)\rho_s) - p_o\gamma_s/((\gamma_s - 1)\rho_{ow}) + \epsilon_{sh} . \qquad (23)$$

All the terms that pertain to steam have been given a subscript "s" and those that pertain to water the subscript "w", p_{so} is the steam pressure behind the front in the one-dimensional stage, T_s is the temperature, ρ_{ow} is the density of the unperturbed water, and m_s is the molecular weight of steam, which is 18. The term ϵ_{sh} is the latent of vaporization at ambient density ρ_{ow} and pressure p_o, and T_{sh} is the interpolated temperature at ambient pressure and density of the undisturbed water, as predicted by the gas equation. The term ϵ_{sh} is given, in terms of the latent heat at constant volume and temperature ϵ_{sv}, by

$$\epsilon_{sh} = \epsilon_{sv} - p_o(\rho_{ow}/\rho_{sv})^{\gamma_s}\gamma_s/((\gamma_s - 1)\rho_{ow})$$

$$= \epsilon_{sv} - 3300 \text{ kJ/kg} ; \text{ at } 25°C \text{ and atmospheric pressure }, \qquad (24)$$

where ρ_{sv} is the interpolated density of steam at ambient temperature T_o and pressure p_o as determined by the gas equation.

These equations may also be applied to a perfect gas by simply setting the latent heat term ϵ_{sh} equal to zero, and T_{sh} equal to T_o. Thus it may also be applied to the air blast propagating upwards from the interface. To distinguish the two cases, the subscript "a" will replace "s" or "w" for the terms associated with air blast. For air the effective molecular weight m_a is 29.

The ratio of specific heats γ for many gases, including air, is dependent on temperature and very weakly dependent on pressures. For air,[27] the value of γ_a varies between 1.4 at room temperature to 1.23 at 2800°K. For steam, however, the variations are much larger. Using steam tables,[28] the values of γ_s were

17

computed over the available range of temperatures and pressures as shown in Fig. 3. It can be seen that for temperatures above 600°C the value of γ_s lies between 1.2 and 1.3. Therefore, a compromise value of 1.25 was chosen for γ_s. This is comparable to the γ values of other triatomic gases such as SO_2 at 1.26 and CO_2 at 1.31.

The latent heat of vaporization at a constant volume is the difference between the internal energies of water and steam. In Fig. 4, plots of the internal energies of water and as a function of temperature at various pressures, obtained from the steam tables, are compared with a straight line perfect gas law computed for the molecular weight of water and a specific heat ratio of 1.25. It is seen that at high temperatures, the curves tend towards the perfect gas line. Assuming an initial state at 25°C and atmospheric pressure, it is seen that the latent heat ε_{sv} is approximately 2300 kJ/kg. Substituting into Eq. (24), this gives ε_{sh} a value of -1000 kJ/kg.

b. Liquid Regime

In addition to the gas regime, the data in Fig. 4 also suggest a liquid regime. In the liquid regime, the specific enthalpy of water, adapted from the state equations given by Cole,[24] is defined by the relationship

$$\omega = \omega_w = ((p_{wo} + p_o)\gamma_w + c_{wo}^{2}(\rho_{ow} - \rho_w))/((\gamma_w - 1)\rho_w) - p_o\gamma_w/((\gamma_w - 1)\rho_{ow})$$

$$= c_{wv}(T_w - T_o) + (p_{wo} + p_o)/\rho_w - p_o/\rho_{ow} \, . \tag{25}$$

where all the terms that pertain to the liquid regime have been given the subscript "w", p_{wo} is the excess pressure of liquid water above the ambient pressure p_o in the one-dimensional stage, c_{wv} is the specific heat at constant volume which is approximately a constant, T_w is the absolute temperature behind the front and T_o is the ambient temperature in front of it, which is assumed to be 298°K (25°C) for calculation purposes, and c_{wo} is the speed of small amplitude sound waves in the unperturbed water which at 25°C is equal

18
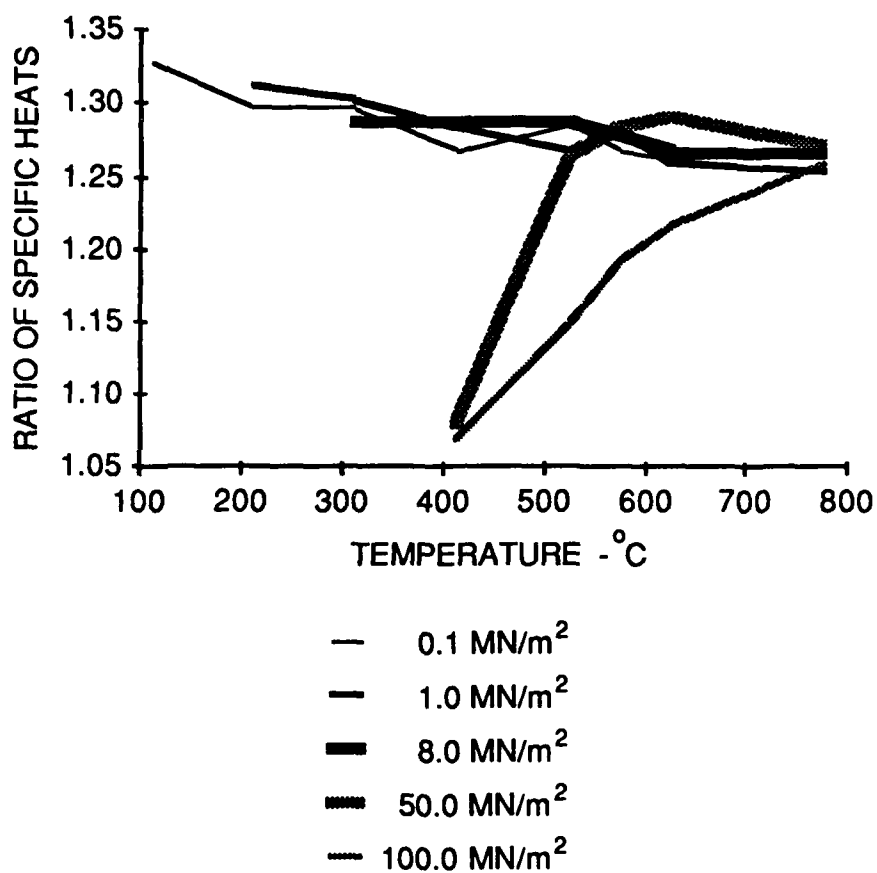
FIGURE 3
RATIO OF SPECIFIC HEATS OF STEAM COMPUTED FROM STEAM TABLES
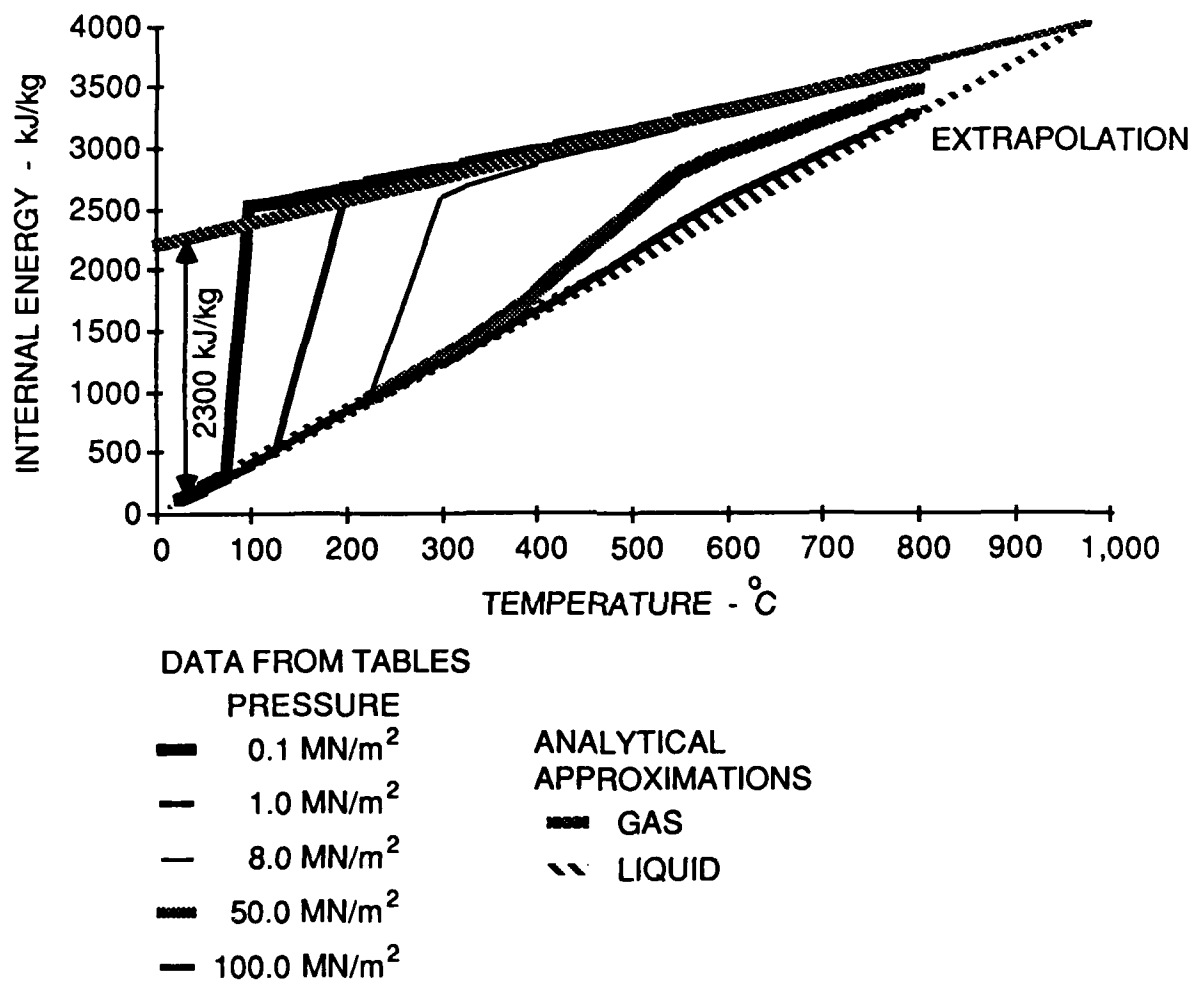
FIGURE 4
INTERNAL ENERGY OF WATER AND STEAM FROM STEAM TABLES

to 1534.6 m/s. Using values from the steam tables, it was estimated that a reasonable approximation may be obtained with $\gamma_w = 1.33$, $\rho_{ow} = 1001$ kg/m^3, and $c_{wv} \approx 4.2$ kJ/kg. The adiabatic state equation is given by[24]

$$p_{wo} = (c_{wo}^2 \rho_{ow}/\gamma_w)((\rho_w/\rho_{ow})^{\gamma_w} - 1) . \tag{26}$$

It is interesting to note that if the asymptotic functions of the internal energy of the liquid and gas regimes, as shown in Fig. 4, were extrapolated, they would intersect. There is a corresponding intersection of the enthalpy functions, which is found by equating the enthalpies as given by Eqs. (23) and (25); the temperature at the intersection is found to be 978°C. Beyond this temperature, the liquid regime, if it existed, would apparently have a higher specific enthalpy than the gas regime.

Despite appearances, Eq. (25) is not a gas equation, and γ_w is not the ratio of specific heats. The specific heat at constant volume c_{wv}, as calculated from the steam tables, was found to be approximately constant in this regime.

The regions on the pressure-temperature diagram in which the above equations for the gas and liquid regimes are valid are shown in Fig. 5; in these regions the parameter estimates of the two respective models were found to be within 10% of the tabulated values from steam tables. Beyond the range of tabulated values, the validity of the models is not known with any certainty; the boundaries shown are mere extrapolations of the boundary functions found for the tabulated region.

c.   Blast Pressure Solution

Eliminating D and u from Eqs. (11)-(13), a general relationship between enthalpy, pressure, and coefficient of expansion is obtained,

$$\omega + p(\eta^2 - 1)/(2(1-\eta)\rho_o) - I_o((1-\eta)/p\rho_o)^{1/2} = 0 . \tag{27}$$

21
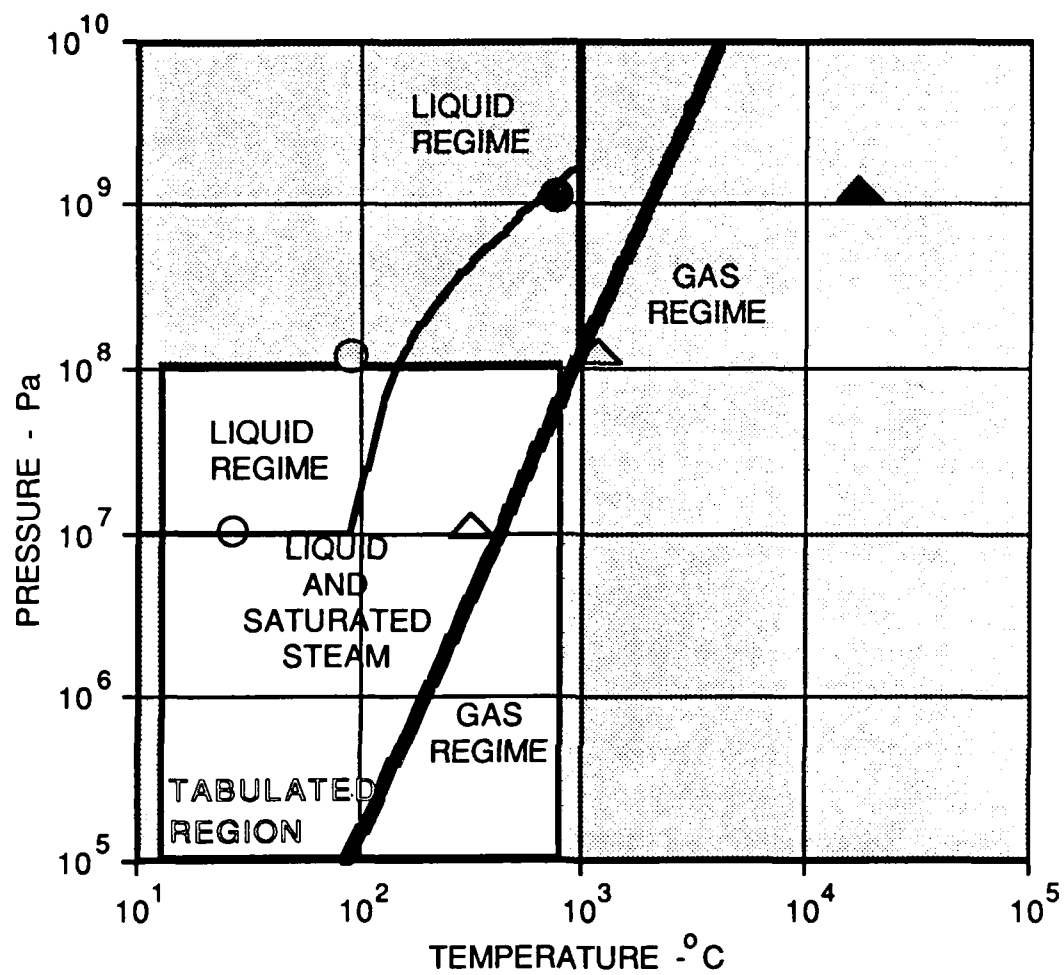
FIGURE 5
LIQUID AND GAS REGIMES OF THE STATES OF WATER

Substituting for ω from either Eq. (23) or (25), and applying subscripts "w" or "s" where appropriate, a cubic equation in $p^{1/2}$ is obtained, of the form

$$p_{xo}^{3/2} + 3a_x p_{xo}^{1/2} + 2b_x = 0 \ . \tag{28}$$

For the pressure behind the one-dimensional front in air p_{ao}, the coefficients a_a and b_a are given by

$$a_a = (2/3)(\ p_o \gamma_a (\eta_a - 1)/(\gamma_a - 1))/(\ (\eta_a(\ \gamma_a + 1)/(\gamma_a - 1)) - 1)\ ,$$

$$b_a = -I_{oa}\ (1 - \eta_a)^{1/2} p_{oa}^{1/2} \ /(\ (\eta_a(\ \gamma_a + 1)/(\gamma_a - 1)) - 1)\ ,$$

where I_{oa} is the power density absorbed by the air front.

Assuming that all the absorbed water is changed into steam, the pressure behind the underwater front p_{uo} is given by the steam pressure p_{so}. The coefficients a_s and b_s for solving for p_{so} are given by

$$a_s = (2/3)[\ \varepsilon_{sh} \rho_{ow} + \gamma_s p_o (\eta_s - 1)/(\gamma_s - 1)]/[(\eta_s(\ \gamma_s + 1)/(\gamma_s - 1)) - 1]\ ,$$

$$b_s = -I_{ou}\ (1 - \eta_s)^{1/2}\ \rho_{ow}^{1/2} \ /(\ (\eta_s(\ \gamma_s + 1)/(\gamma_s - 1)) - 1)\ ,$$

where I_{ou} is the power density at the underwater front.

Finally, assuming that all the absorbed water remains in the liquid state, the pressure behind the underwater front p_{uo} is given by the water pressure p_{wo}. The coefficients a_w and b_w for solving for p_{wo} are given by

$$a_w = (2/3)\rho_{ow}(c_{wo}^2 + \gamma_w p_o/\rho_{ow})(\ \eta_w - 1)/(\ \eta_w(\ \gamma_w + 1) - (\ \gamma_w - 1))\ ,$$

$$b_w = -I_{ou}\ (1 - \eta_w)^{1/2}\ \rho_{ow}^{1/2} \ /(\ (\eta_w(\ \gamma_w + 1)/(\gamma_w - 1)) - 1)\ .$$

The general solution where a valid one exists is given by

$$p_{xo} = [\,(-b_x + \sqrt{(b_x^2 + a_x^3)}\,)^{1/3} - (b_x + \sqrt{(b_x^2 + a_x^3)}\,)^{1/3}\,]^2 \,, \qquad (29)$$

where the condition for a valid solution is: $b_x^2 + a_x^3 > 0$. This condition implies that there are minimum levels of the power densities or intensities I_{oa} and I_{ou} that are necessary to the sustenance of the respective fronts.

In each case, the value of h_x remains to be found by the maximum entropy condition. For a gas at high pressure, including air and superheated steam, it is given by the Chapman-Jouguet condition in Eq. (22). In the general case, however, it must be found by the maximum entropy condition. Since in all three cases that are of interest here the specific heats at constant volume may be treated as constants, the procedure for obtaining an expression for the entropy in terms of η_x is straightforward. Using the state equation such as Eqs. (14), (23), or (25) as the case may be, the fluid is allowed to expand isentropically to an intermediate state that has the same density as its final density. An expression is found for the temperature at this intermediate state. Then, it is allowed to heat up at constant volume to its final state, and a second expression is found for the temperature at the final state. Since the specific heat at constant volume is approximately constant, the result is an expression similar to Eq. (20). Finally, the expression for entropy is differentiated with respect to η_x to find the maximum entropy condition.

For air and superheated steam at high pressures, the equations for the variable part of the entropy are identical to those of the air blast, and thus Eqs. (17)-(21) may be used.

For the liquid regime, the expressions for the intermediate and final absolute temperatures T_{wo}' and T_w, corresponding to T_o' and T, are not as simple as for the gas regime. They are found from the state equation of Eq. (25) and the adiabatic equation of Eq. (26) to be

24

$$c_{wv}(T_{wo}' - T_o)$$

$$= c_{wo}^2 ((h_w/g_w)(h_w^{-g_w}-1) + h_w-1)/(g_w-1) - p_o(1-h_w)/(r_{ow}(g_w-1)) \ , \qquad (30)$$

$$c_{wv}(T_w - T_o)$$

$$= (p_{wo}h_w + c_{wo}^2 r_{ow}(h_w-1))/(r_{ow}(g_w-1)) - p_o(1-h_w)/(r_{ow}(g_w-1)) \ . \qquad (31)$$

Substituting for T_o' and T in Eq. (20) with the above expressions for T_{wo}' and T_w, and differentiating with respect to h_w, the maximum entropy condition may be found. The resulting equation, however, is very messy. Thus, for this case, a numerical method for finding the maximum entropy condition may be preferable.

Numerical results for the three case studies are shown in Table II. The maximum entropy conditions for all the blast fluids were found numerically by the Newton interpolation method. The values of h for maximum entropy and for the Jouguet condition are shown for comparison. It is seen that, where applicable, they are identical, except in case 1 where the pressure, at 130 atmospheres (1.3 ¥ 10^7 Pa), is sufficiently low that atmospheric pressure is not entirely negligible. The minimum intensity required to sustain each front, calculated according to the validity condition for Eq. (29), is shown along with the actual power density absorbed; in case 1, it will be shown that the laser intensity is insufficient to support the total process, and therefore the minimum intensity is used for calculation purposes. In all cases, it was found that the water exiting the underwater front is in the liquid regime, and the air at the air front remains in the gaseous phase. It should be noted that the calculated air temperature as it exits the air front is very high, ranging from 22,000°C in case 1 to 1.9 million°C in case 3. It will be shown in the following section that the air is not expected to remain at these extremely high temperatures for any significant length of time because it will immediately mix with the gases in the interior of the blast which are considerably cooler.

TABLE II
EQUILIBRIUM BLAST MODEL CASE STUDIES: FRONT CONDITIONS

PHYSICAL CONSTANTS

Medium		Steam	Water	Air
Molecular weight	g mole	18	18	32
Ambient density	kg/m^3	N/A	1001	1.3
Adiabatic exponent		1.25	1.335	1.4
Latent heat of vaporization	J/kg	N/A	2.3E+6	N/A
Specific heat at constant volume	kJ/kg	4.2	4.2	0.72
Sound speed	m/s	N/A	1535	330

CASE		1	2	3
Spot diameter	m	0.0032	0.00066	0.00017
Spot area	m^2	8.0E-6	3.4E-7	2.3E-8
Incident intensity	W/m^2	5.6E+11	1.3E+13	2.0E+14
Energy density	MJ/m^2	0.03	1.0	14

FRONT CHARACTERISTICS

Medium		Water	Air	Water	Air	Water	Air
Minimum intensity	W/m^2	1.7E+10	2.6E+7	1.7E+10	2.6E+7	1.7E+10	2.6E+7
Actual intensity	W/m^2	*1.7E+10*	7.7E+10	1.0E+12	2.5E+12	2.2E+13	6.3E+13
η (maximum entropy)		0.9960	0.5852	0.9856	0.5833	0.9780	0.5833
η (Jouguet condition)		N/A	0.5833	N/A	0.5833	N/A	0.5833
Phase		LIQUID	GAS	LIQUID	GAS	LIQUID	GAS
Front velocity	m/s	1.8E+3	4.9E+3	3.0E+3	1.5E+4	7.1E+3	4.5E+4
Mach number		1.16	14.71	1.96	46.81	4.64	137.13
Absolute particle velocity	m/s	7.2	2.0E+3	43	6.4E+3	1.6E+2	1.9E+4
Front pressure	Pa	1.3E+7	1.3E+7	1.3E+8	1.3E+8	1.1E+9	1.1E+9
Front temperature	°C	27	2.2E+4	92	2.3E+5	7.6E+2	1.9E+6
Specific enthalpy	kJ/kg	2.2E+4	2.0E+7	4.1E+5	2.0E+8	4.2E+6	1.7E+9
Specific entropy	kJ/kg/K	32	2.9E+3	8.5E+2	4.6E+3	5.2E+3	6.1E+3

Notes :

1. Ambient temperature, laser power, and pulse duration are as stated in Table I.

2. The intensity at the underwater front in case 1 (in *italics*) is the minimum consistent with the maximum entropy condition.

3. Equilibrium Conditions

To obtain equilibrium, the pressures behind the air and the underwater fronts p_{ao} and p_{uo}, as defined by Eq. (28) and its solution Eq. (29), and the pressure p_{go} of the interior of the blast volume must all be equal. Thus,

$$p_{go} = p_{ao} = p_{uo} . \tag{32}$$

With two fronts back-to-back producing gases at the same pressure but at different temperatures and densities, there is bound to be an increase in entropy in the subsequent temperature equalization. This will result in a net loss of pressure in the interior of the blast. To maintain equilibrium, a proportion of the supplied laser power must be diverted to the gases in the interior in order to restore the gas pressure.

The initial enthalpy density rate h_g' entering the interior per unit area of the fronts is given by

$$h_g' = (\omega_a D_{ao} \rho_{oa} + \omega_u D_{uo} \rho_{ou}) , \tag{33}$$

where D_{ao}, D_{uo}, ρ_{oa}, and ρ_{ou} are the front velocities in air and underwater and the unperturbed densities of the two media, respectively. The specific enthalpies ω_a and ω_u may be computed from Eqs. (23) and (25), respectively. The final enthalpy density rate, after temperature equalization, may be expressed in a similar form,

$$h_g = (\omega_{ag} D_{ao} \rho_{oa} + \omega_{ug} D_{uo} \rho_{ou}) , \tag{34}$$

where ω_{ag} and ω_{ug} are the final specific enthalpies after temperature equalization of the fluids in the interior. The subscript "g" is added to distinguish the physical properties at equilibrium from the corresponding properties of the fluids in their initial conditions. The energy absorption rate I_{og} of the blast interior per unit frontal area is then given by

27

$$I_{og} = h_g - h_g' . \tag{35}$$

The terms ω_a and ω_u may be evaluated through Eq. (23). To find ω_{ag} and ω_{ug}, we start by finding the corresponding final component densities ρ_{ug} and ρ_{ag} of the interior fluids. One equation relating them is obtained by invoking conservation of mass and total volume, giving

$$(D_{ao} + D_{uo}) = (D_{ao}\rho_{oa}/\rho_{ag}) + (D_{uo}\rho_{ou}/\rho_{ug}) . \tag{36}$$

A second independent expression relating ρ_{ag} and ρ_{ug} may be found by equating the temperatures of the two fluids and setting their pressures equal to the blast pressure p_g, through the state equations of Eqs. (23) and (25). Thus, it is possible to solve for ρ_{ag} and ρ_{ug}.

For the case where all the absorbed water is converted into superheated steam, it is found that the density ratios at equilibrium are simply given by the *molecular weight* ratios, giving

$$\rho_{ag}/\rho_{ug} = m_a/m_s . \tag{37}$$

Using Eqs. (36) and (37), the component densities ρ_{ag} and ρ_{ug} may be simply solved giving, for ρ_{ug},

$$\rho_{ug} = ((D_{ao}\rho_{oa} m_s/m_a) + D_{uo}\rho_{ou})/(D_{ao} + D_{uo}) \tag{38}$$

and a symmetrical expression for ρ_{ag}. Setting the pressures equal to p_{go} and using the above expression for ρ_{ag} and ρ_{ug}, expressions for the final specific enthalpies ω_{ag} and ω_{ug} of the two gaseous components may be obtained through the state equation of Eq. (23). Finally, substituting the resulting expressions for ω_{ag} and ω_{ug} into Eq. (34), a solution for the final enthalpy density rate may be found for the air-steam mixture.

In the case where the absorbed water remains a liquid, the problem is more complicated. There are three distinct possibilities here. One is that the liquid water within the blast may coalesce into large droplets resulting in very little heat exchange with the surrounding hot air, in which case there will be no temperature equalization. This possibility is considered unlikely since the gases from the air front will be at a high temperature and highly agitated and therefore it would tend to break up the water droplets. The second possibility is that the liquid water evaporates into steam on contact with the hot air; in this case Eqs. (33)-(38) would be applicable. The third is that the liquid water exists as a fine spray and exchanges heat with the hot air but remains in liquid form. This last possibility is addressed by equating the temperatures of the air and the liquid water and setting the pressures equal to equilibrium pressure p_g. Through the state equations of Eq. (23) and (25), the second independent equation relating ρ_{ag} and ρ_{ug} is given as

$$((p_g + p_o)\gamma_w + c_{wo}^2 (\rho_{ow} - \rho_{ug}))/((\gamma_w - 1)\rho_{ug}) - p_o\gamma_w/((\gamma_w - 1)\rho_{ow})$$

$$= c_{wv}((p_g m_a/(R\rho_{ag})) - T_o) + (p_g + p_o)/\rho_{ug} - p_o/\rho_{ow} . \qquad (39)$$

Eliminating ρ_{ag} from Eqs. (36) and (39), ρ_{ug} is given by

$$\rho_{ug}/\rho_{ow} = ((\gamma_w - 1)c_{wv}p_g(m_a/R)(D_{uo}r_{ou}/D_{ao}\rho_{oa}) + p_g + c_{wo}^2\rho_{ow} + p_o)$$

$$+ ((\gamma_w - 1)(c_{wv}p_g(m_a/R)(D_{uo} + D_{ao})/(D_{ao}\rho_{oa}) - T_o) + c_{wo}^2\rho_{ow} + p_o) . \qquad (40)$$

Substituting for r_{ug} from Eq. (40) into (36) a similar expression for ρ_{ag} may be found. Applying the expressions for the final densities of the air and water components, ρ_{ag} and ρ_{ug}, to their respective state equations, Eqs. (23) and (25) respectively, expressions for the final specific enthalpies of the two components may be obtained. Again, substituting the resulting expressions for ω_{ag} and ω_{ug} into Eq. (34), a solution for the final enthalpy density rate may be found for the air-water mixture.

29

From the above analysis, it is seen that the laser intensity I_{tot} must be divided into three parts,

$$I_{tot} = I_{oa} + I_{ou} + I_{og} . \tag{41}$$

where I_{oa} is the part supplied to the air front, I_{ou} to the underwater front, and I_{og} to the interior of the blast. The pressure equilibrium conditions as stated in Eq. (32) determine the exact division of intensities.

Numerical case studies of the equilibrium conditions are shown in Table III. The values of I_{oa}, I_{ou}, and I_{og} were found iteratively, using the pressure and temperature equilibrium conditions as defined in the above equations. The percentage breakdown of the power distribution shows that a very large proportion is absorbed by the interior of the blast. In case 1, we have a situation where the laser intensity is sufficient to drive the two fronts, but insufficient to maintain the internal pressure of the blast; therefore, the blast is effectively quenched as soon as the fluids from the two fronts meet. It is also apparent that only a proportion of the laser intensity, 6.39% in case 2 and 11.10% in case 3, is directly employed in driving the underwater blast front. These percentages are expected to have a direct influence on the sound generation efficiency of the process. In cases 2 and 3, it was found that the water, which was still in a liquid form as it emerged from the underwater front, would be converted into superheated steam (gas regime) after mixing with the hot air from the air front; the temperature of the mixture, while still high, at 1,747°C in case 2 and 17,940°C in case 3, is still significantly lower than that of the air front. Therefore the air probably does not remain at the extremely high temperatures shown in Table II for any significant length of time, probably no more than the duration of a few mean free paths. In case 1, had there been enough laser intensity to maintain equilibrium, the water would have turned into saturated steam. Since this result is outside the two regimes of water that were analytically modeled, it had to be found iteratively by hand using temperature, pressure, density, and enthalpy data from the steam tables. The states of the water in the three case studies, both at the front and in the interior, are shown in the Fig. 5 for comparison.

TABLE III

EQUILIBRIUM BLAST MODEL CASE STUDIES: EQUILIBRIUM CONDITIONS

CASE		1	2	3
Spot diameter	m	0.0032	0.00066	0.00017
Spot area	m^2	8.0E-6	3.4E-7	2.3E-8
Incident intensity	W/m^2	5.6E+11	1.3E+13	2.0E+14
Energy density	MJ/m^2	0.03	1.0	14
INTERIOR CHARACTERISTICS				
Initial enthalpy density rate	W/m^2	1.7E+11	5.3E+12	1.3E+14
Final enthalpy density rate	W/m^2	7.7E+12	1.5E+13	2.5E+14
Equilibrium temperature	^oC	602	1,747	17,940
Laser intensity absorbed	W/m^2	7.5E+12	9.8E+12	1.1E+14
Phase of water/air components		Sat.Steam*/GAS	GAS/GAS	GAS/GAS
* Dryness fraction	%	18.9		
FEASIBILITY				
Input power distribution				
Air front	%	13.80	19.08	31.86
Water front	%	3.05	6.39	11.10
Interior equilibrium	%	1341.97	74.53	57.04
TOTAL %		(1358.82)	100.00	100.00
Is the laser power adequate?		NO	YES	YES
CONDUCTION LIMITED CONDITIONS				
Critical thickness (1-dimensional stage)	m	3.6E-7	2.6E-5	1.5E-4
τ_k (1-dimensional stage)	s	5.5E-11	1.4E-9	2.9E-9
CHARACTERISTICS OF THE 2-DIMENSIONAL STAGE				
τ_{2D}	s	1.3E-7	8.4E-9	7.4E-10
τ_u	s	1.3E-7	8.4E-9	2.3E-9
LASER PULSE UTILIZATION	%	100	22.39	6.02

It appears that the laser energy must enter the blast volume through the air front. From the air blast front, it is transported through the interior towards the underwater front. There are a number of possible transport mechanisms. The two main candidates are conduction and reradiation. Conduction in this case is taken to include convection. Under the reradiation category, there are several candidates, including simple scattering, Raman scattering, and stimulated emissions. We will only consider the conduction mechanism in this study.

Let us now consider the conduction mechanism in greater detail. Conduction will take place naturally since the temperature at the underwater front, as the numerical results show, is always significantly less than that at the air front. Furthermore, any drop in pressure at the underwater front will be accompanied by a further temperature reduction, which will increase the temperature gradient. Therefore, as long as the distance between the two fronts is small such that the thermal resistance is negligible, the process will be a dynamic and stable one in which the input laser energy tends to be distributed in a way that will maintain the equilibrium. The thermal conductivity k of steam and air may be approximated by a linear temperature dependence,

$$k = k_1 T + k_0 , \tag{42}$$

where k_1 and k_0 are constants.

For air, it was found that using the values (0.000062, 0.0054) for (k_0, k_1) in SI units, the above conductivity function gives values that are very close to the tabulated values[27] over a wide range of conditions. The tabulated values of the thermal conductivity of water do not increase monotonically with temperature, but within ±20% they can be represented by a single constant value of 0.6 W/m/°K. The conductivity of steam at low temperatures has a very complicated dependence on pressure and temperature, but curves constructed from the tabulated values suggest that at higher temperatures it also converges to a linear temperature dependence of the form shown in Eq. (42); it was found that values for (k_0, k_1) of (0.000062, 0.012) could be expected to give a good fit.

The comparisons between tabulated values and the analytical approximations are shown in Fig. 6.

The necessary heat flow rate per unit area is given by the power density required to drive the underwater front and to maintain equilibrium in the blast fluids ($I_{ou} + I_{og}$). This is related to the temperature gradient dT/dx by

$$dT/dx = (I_{ou} + I_{og})/k \ , \tag{43}$$

where x is vertical distance. Substituting for k from the above equation and integrating, a relationship is found between the temperatures T_{ao} and T_{uo} at the air and underwater fronts, the power density ($I_{ou} + I_{og}$), and a critical thickness x_c, given by
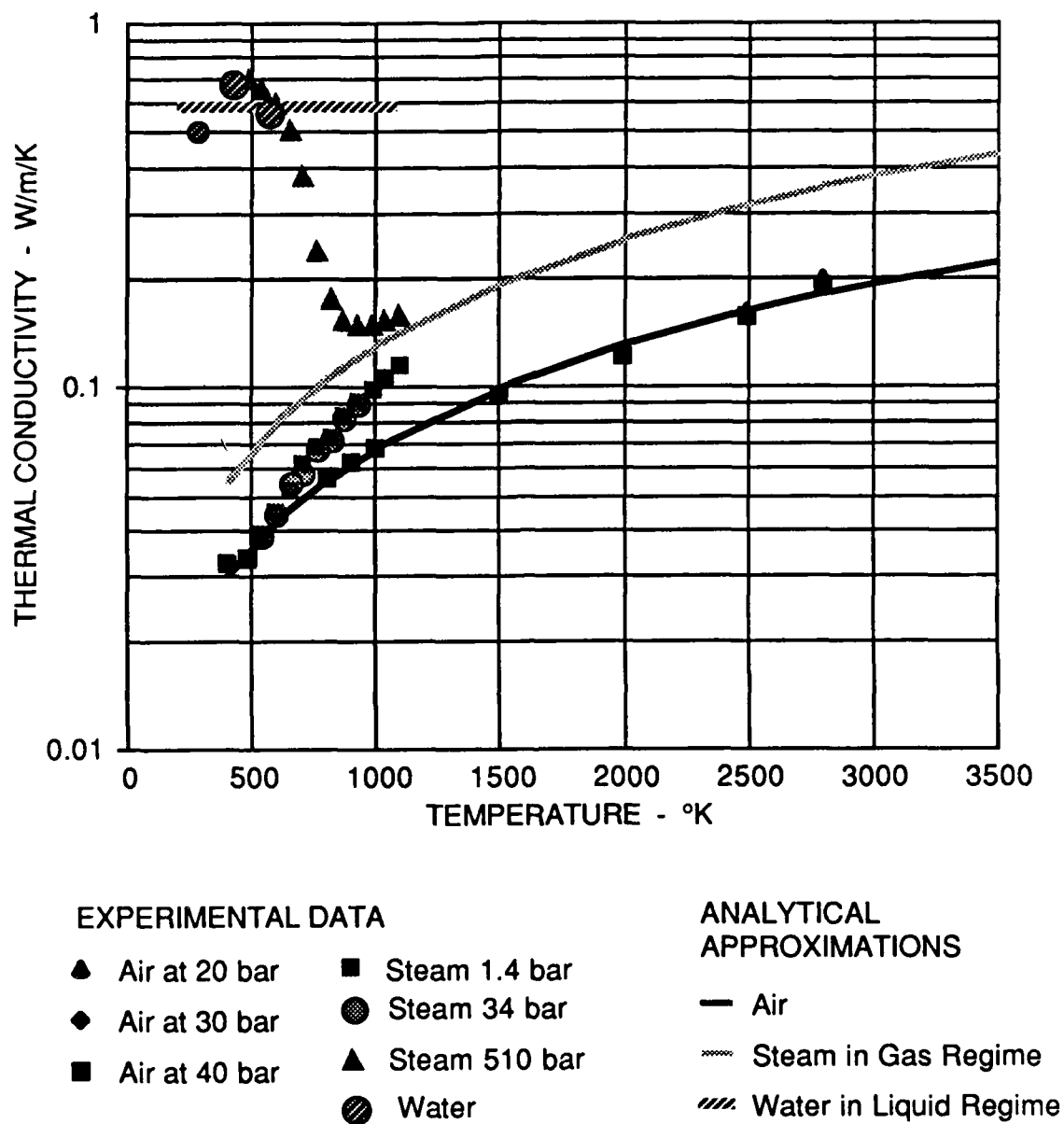
$$(I_{ou} + I_{og}) x_c = k_0(T_{ao} - T_{uo}) + k_1(T_{ao}^2 - T_{uo}^2)/2 \ . \tag{44}$$

For a layer of a thickness less than x_c, the energy distribution within the layer will remain in dynamic equilibrium. When the layer thickness exceeds x_c, the free flow of energy from the air front to the underwater front will be impeded and the pressure at the underwater front will decline. With the air and underwater fronts moving apart at a velocity of ($D_{ao} + D_{uo}$), the critical thickness x_c will be reached at an estimated time of τ_k after the start of the process, where τ_k is simply given by

$$\tau_k = x_c/(D_{ao} + D_{uo}) \ . \tag{45}$$

Computed values of τ_k for the one-dimensional stage are shown in Table III for the three case studies.

After the critical thickness is reached, the energy distribution within the blast volume will be distorted. An increasingly smaller proportion of the energy will reach the underwater front. The pressure at the underwater front will drop giving rise to a pressure gradient within the blast volume which will tend to drive

33

EXPERIMENTAL DATA

▲ Air at 20 bar   ■ Steam 1.4 bar

◆ Air at 30 bar   ● Steam 34 bar

■ Air at 40 bar   ▲ Steam 510 bar

               ◉ Water

ANALYTICAL APPROXIMATIONS

— Air

····· Steam in Gas Regime

///. Water in Liquid Regime

FIGURE 6
THERMAL CONDUCTIVITIES

the blast gases into the water. This is a likely mechanism for the subsequent formation of an underwater gas bubble. The air front may be expected to continue to travel at more or less its original speed. The underwater front will slow down. Since, as the numerical results in Table II show, the underwater front velocity and temperature are small compared to those of the air front, it can be deduced that the layer thickness will be mainly determined by the air front velocity D_{ao}. Consequently, the power density I_u at the underwater front will decline as the reciprocal of time. Thus, the power density I_u may be expressed in terms of the initial power density I_{ou} divided by a correction factor β_k,

$$I_u = I_{ou}/\beta_k \quad ; \quad \text{for } t > \tau_k \, , \tag{46}$$

where

$$\beta_k = t/\tau_k \, . \tag{47}$$

4. The Two-Dimensional Stage

As the two blast fronts move away from each other, the thickness of the interior volume will increase. In addition to its vertical expansion, the blast volume also expands laterally outward. It is reasonable to ignore the lateral expansion and treat the process as one-dimensional until the front displacements become comparable to their diameters. As the vertical and lateral displacements increase, the frontal area will also increase. This will cause the rate of mass absorption to be significantly increased and thus the input laser power will have to be diluted over an increasingly larger mass input rate. The idealized geometry is shown in Fig. 7, which shows the air and underwater fronts expanding both vertically and laterally. The result is a reduction in the intensity available to drive the underwater front. The effects on the pressure at the underwater front are of particular interest since it will have a direct impact on the acoustic output of the process.
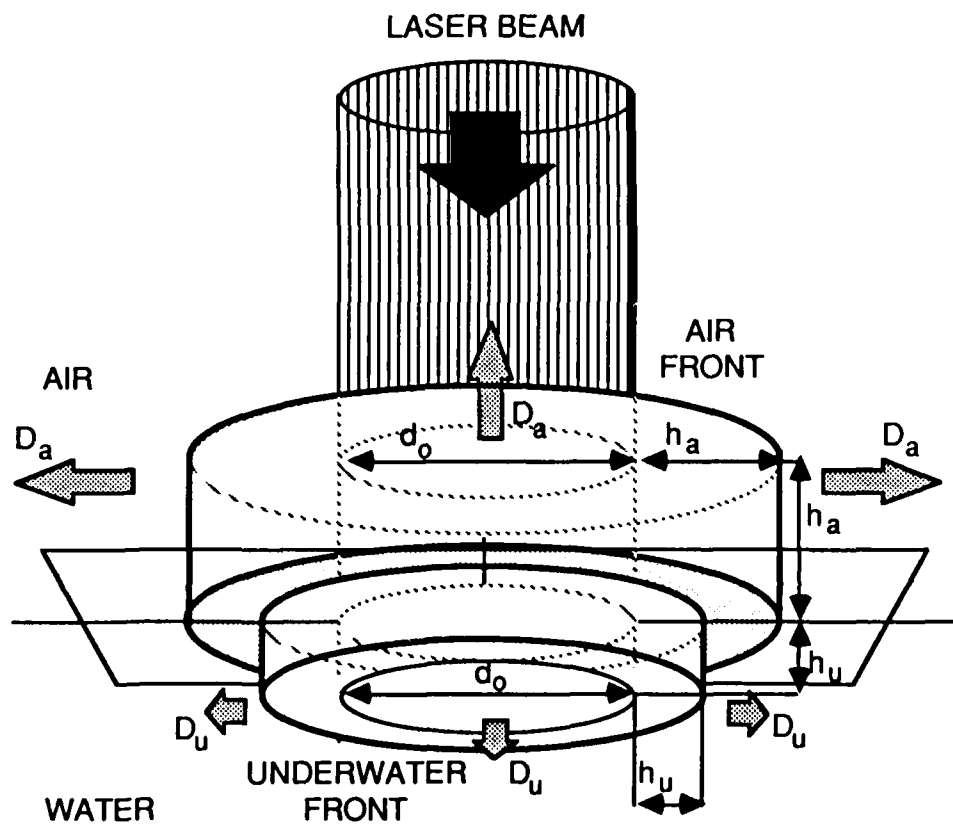
FIGURE 7
IDEAL GEOMETRY OF THE TWO-DIMENSIONAL STAGE:
NEGLIGIBLE THERMAL RESISTIVITY CASE

To account for the reduction in pressure at the underwater front, the energy equation of Eq. (13) as it applies to the underwater front is now modified by replacing the power input per unit area term I_o with a time dependent term I_u for the underwater blast. Let I_u be expressed in terms of its initial value I_{ou} and a correction term b_u, giving

$$I_u/(r_o D) = I_{ou}/(r_o D b_u) = w + 0.5u^2 - 0.5D^2 . \qquad (48)$$

If it can be assumed that the thermal resistivity is negligible, then the input energy will be distributed in a way that will maintain pressure and thermal equilibrium within the volume. Then, the parameter b_u is given by the ratio between the mass absorption rates between the one-dimensional stage at time $t=0_+$ and at a general time t. With reference to the geometry shown in Fig. 7, it can be seen to be given by

$$b_u(D_{uo}W_{uo} + W_{ao}D_{ao})\pi d_o^2 /4$$

$$= W_u (D_u\pi(d_o + 2h_u)^2/4 + \pi D_u(d_o + 2h_u)h_u)$$

$$+ W_a (D_a\pi(d_o + 2h_a)^2/4 + \pi D_a(d_o + 2h_a)h_a) . \qquad (49)$$

The terms W_a and W_u are weights related to the relative energy consumption rates of the fronts and the interior given by

$$W_a = ((I_a/I_u)+(I_g/I_u)(D_a/(D_a + D_u))$$

and

$$W_u = (1 + (I_g/I_u)(D_u/(D_a + D_u)) . \qquad (50)$$

The terms W_a, W_u, I_a, I_u, I_g, D_a, and D_u are functions of time t while W_{ao}, W_{uo}, I_{ao}, I_{uo}, I_{go}, D_{ao}, and D_{uo} are their initial values in the one-dimensional stage at $t=0_+$; d_o is the initial diameter of the frontal area, which is also equal to the diameter of

the laser beam, and h_a and h_u are the vertical distances traveled by the fronts, given by

$$h_a = \int_0^t D_a \, d\tau$$

and

$$h_u = \int_0^t D_u \, d\tau \quad . \tag{51}$$

Let us model D_a and D_u as functions that are approximately constant in the one-dimensional stage, defined as the interval $0 < t \leq \tau_{2D}$ where τ_{2D} is taken to be a time constant characteristic of the duration of the one-dimensional stage. For $t > \tau_{2D}$ let D_a and D_u asymptotically decay as $(t/\tau_{2D})^s$, where s is a negative power. Using this model, the time integral of D_a may be approximated by

$$\int_0^t D_a \, d\tau \approx t D_{ao} \left(\tau_{2D}/t + \int_{\tau_{2D}}^t (\tau/\tau_{2D})^s/t \, d\tau \right)$$

$$\approx t D_{ao} \left(\tau_{2D}/t - (\tau_{2D}/t)/(1+s) + (t/\tau_{2D})^s/(1+s) \right) \quad , \tag{52}$$

and similarly for that of D_u. This model will also conveniently make the weights W_a and W_u time independent. Assuming that $0 > s > -1$ and large t, the time integral of D_a may be approximated by the asymptote

$$\int_0^t D_a \, d\tau \rightarrow t D_{ao} (t/\tau_{2D})^s/(1+s) \quad . \tag{53}$$

A similar result is also obtained for the time average of D_u. Substituting the asymptotic forms of D_a and D_u and their integrals into Eq. (49), the asymptotic form of β_u is given by

$$\beta_u \;\to\; 12\,(W_{ao}D_{ao}{}^3 + W_{uo}D_{uo}{}^3)(t/\tau_{2D})^{3s+2}\,\tau_{2D}{}^2(1+s)^{-2}$$

$$\times \quad (\,D_{uo}W_{uo} + W_{ao}D_{ao}\,)^{-1}d_o{}^{-2} \;. \tag{54}$$

Using I_{ou}/β_u instead of I_o in the expression for front velocity of Eq. (1), it is deduced that D_u varies as $\beta_u{}^{-1/3}$. Since the above equation shows that β_u is asymptotically proportional to t^{3s+2}, equating the powers of t, it is deduced that

$$s = (-1/3)(3s+2) \;. \tag{55}$$

Solving, it is found that the value of s is -1/3, which justifies our initial assumption of its range of values. Substituting for s in Eq. (54), it is found that β_u must vary linearly with t. Then, using I_{ou}/β_u instead of I_o in Eq. (15), it is deduced that the pressure p_u at the underwater front must vary as

$$p_u \;\to\; p_{uo}\,(\tau_{2D}/t)^{2/3} \qquad ;\ \text{for}\ t > \tau_{2D} \;, \tag{56}$$

where p_{uo} is the initial pressure in the one-dimensional stage.

To obtain an approximate estimate of τ_{2D} let us equate the asymptotic form of β_u to the initial value of β_u which is one, replace t with τ_{2D}, and solve, giving

$$\tau_{2D} = d_o\,(1+s)\,[(D_{uo}W_{uo} + W_{ao}D_{ao})/(12(W_{ao}D_{ao}{}^3 + W_{uo}D_{uo}{}^3))]^{-1/2} \;. \tag{57}$$

Calculated values of τ_{2D} for the three case studies are shown in Table III.

5. Pressure Decay

Let us now consider the case where the blast enters the two-dimensional stage and then enters the conduction limited condition, i.e., the case where $\tau_{2D} < \tau_k$ for time $t > \tau_k$. This is applicable when the laser beam is narrow; thus the blast is apt to enter the two-dimensional stage before its dimensions approach the critical thickness of the conduction limited condition.

The correction term β_k' for the conduction limited condition will differ by a constant factor from β_k as given by Eq. (47) because the decline in pressure due to the two-dimensional expansion will alter the time constant of the conduction limited condition. Otherwise, the intensity reductions due to expansion and thermal conduction limitation are expected to be independent, and hence multiplicative. Using the asymptotic forms of β_u and β_k', the power density at the underwater front I_u will be given by

$$I_u = I_{ou}/(\beta_u \beta_k')$$

$$\rightarrow I_{ou}(\tau_u/t)^2 \quad ; \quad \text{for } t \gg \tau_u \ , \tag{58}$$

where τ_u is the new time constant for the combined conduction and expansion effects. Replacing I_o in Eq. (15) with I_u from the above equation, it is seen that the pressure will decline as $t^{-4/3}$. Thus, the underwater front pressure p_u is asymptotically given as

$$p_u \rightarrow p_{uo} \quad\quad\quad ; \quad \text{for } t \ll \tau_u$$

$$\rightarrow p_{uo}(\tau_u/t)^{4/3} \quad ; \quad \text{for } t \gg \tau_u \ . \tag{59}$$

To obtain an estimate of τ_u it is necessary to return to Eq. (44) and replace the constant terms $(I_{ou} + I_{og})$, T_{ao}, and T_{uo} with their time dependent counterparts $(I_u + I_g)$, T_a, and T_u. From the above analysis of $(I_{ou} + I_{og})$, T_{ao}, and T_{uo}, it is deduced that their asymptotic forms are

$$(I_u + I_g) \rightarrow (I_{ou} + I_{og})(\tau_{2D}/t) \quad\quad\quad ; \quad \text{for } t > \tau_{2D} \tag{60}$$

$$T_a \rightarrow T_{ao}(\tau_{2D}/t)^{2/3} \quad\quad\quad\quad ; \quad \text{for } t > \tau_{2D} \tag{61}$$

$$T_u \rightarrow T_{uo}(\tau_{2D}/t)^{2/3} \quad\quad\quad\quad ; \quad \text{for } t > \tau_{2D} \ . \tag{62}$$

Substituting τ_u for t and replacing $(I_{ou} + I_{og})$, T_{ao}, and T_{uo} with $(I_u + I_g)$, T_a, and T_u, in Eq. (44), a relationship between x_c and τ_u is found.

$$(I_{ou} + I_{og})(t_{2D}/\tau_u) \, x_c$$

$$= k_o(T_{ao} - T_{uo})(\tau_{2D}/\tau_u)^{2/3} + k_1(T_{ao}{}^2 - T_{uo}{}^2)(\tau_{2D}/\tau_u)^{4/3}/2 \quad . \tag{63}$$

A second relationship between x_c and τ_u is given by

$$x_c = \int_0^{\tau_u} D_a + D_u \, d\tau$$

$$\rightarrow (D_{ao} + D_{uo})\tau_{2D}(1 + 3(\,(\tau_u/t_{2D})^{2/3} - 1)/2) \; ; \; \text{for } \tau_u > \tau_{2D} \quad . \tag{64}$$

Eliminating x_c from these two equations, a cubic equation in $(\tau_{2D}/\tau_u)^{1/3}$ is found,

$$(I_{ou} + I_{og})\tau_{2D}(D_{ao} + D_{uo})(\, 3 - (\tau_{2D}/\tau_u)^{2/3}\,)/2$$

$$= k_o(T_{ao} - T_{uo})(\tau_{2D}/\tau_u)^{1/3} + k_1(T_{ao}{}^2 - T_{uo}{}^2)(\tau_{2D}/\tau_u)^{3/3}/2 \, , \tag{65}$$

which may be solved using standard solutions.

In the case where the blast enters the conduction limited condition while still in its one-dimensional stage, i.e., $\tau_{2D} \geq \tau_k$, the underwater front pressure will decline according as $t^{-2/3}$ until the two-dimensional stage is reached. It will reach the two-dimensional stage at a time not significantly different from τ_{2D} as defined in Eq. (57). This is because the arrival time of the two-dimensional stage is mainly controlled by the velocity of the air blast front since it is very much faster than the underwater front; and, since the air front velocity is largely unaffected by the conduction limited condition, it is expected that τ_{2D} is also largely unaffected. Therefore, in this case, the time constant τ_u for the combined conduction and expansion effects is simply equal to τ_{2D}.

41

The values of τ_u for the three case studies are shown in Table III. It is seen that the values of τ_u can be very small, ranging from 0.13 μs in case 1 to 2.3 ns in case 3.

The above results suggest that there is a definite time window in which the laser energy will have the maximum effect. This time window is expected to be closely related to τ_u. By integrating the pressure p_u as defined in Eq. (59), over all time, a simple expression for the total impulse delivered to the water by the blast is obtained.

$$\text{Impulse} = \int_0^\infty p_u \, dt$$

$$= 4\tau_u \, p_{uo} \, . \tag{66}$$

It can be shown that more than half of the impulse is delivered between t=0 and t=$4\tau_u$. Therefore, the usefulness of any laser energy that arrives after $4\tau_u$ will be much reduced. Thus, dividing the laser pulse length by $4\tau_u$, an estimate of the percentage of the laser energy that is most useful may be estimated. The results for the case studies as shown in Table III indicate that, while in case 1 all the laser energy is useful, in case 3 the useful proportion is only 6.02%.
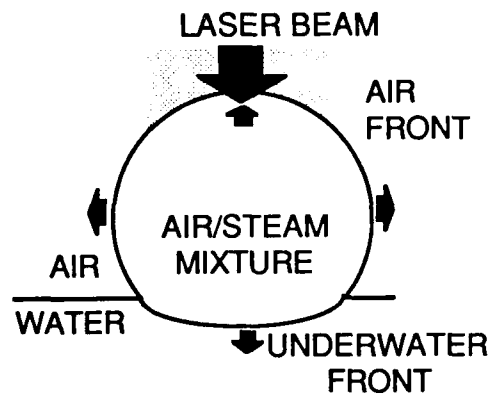
6. Blast Evolution

From the above analysis and numerical case studies, it is possible to piece together a qualitative picture of the evolution of the blast process.

In the one-dimensional stage, two fronts will form at the interface and begin to move apart. With its much higher equilibrium velocity, the air blast front will move away from the interface at a faster rate than the underwater front. Thus, the blast volume will be mainly above the water surface, as illustrated in Fig. 8(a). The blast will send a shock front into the water. At τ_{2D} the blast enters the two-dimensional stage, in which dilution of the input power from the laser over an increasingly larger frontal area and interior volume becomes

42
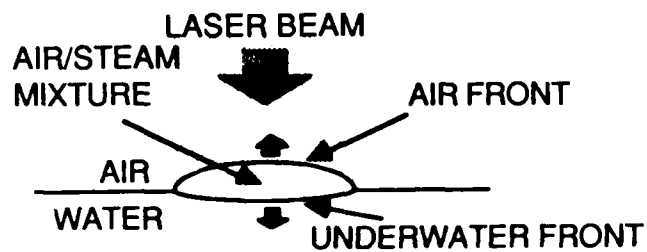
(a) ONE-DIMENSIONAL STAGE

(b) TWO-DIMENSIONAL STAGE
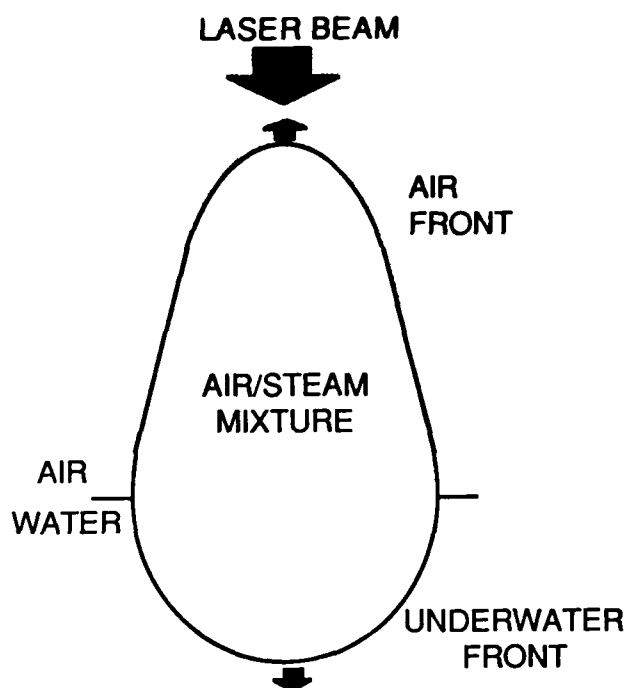
(c) THERMAL CONDUCTION LIMITED CONDITION

FIGURE 8
BLAST EVOLUTION

significant. Therefore, the fronts will continue to expand but at increasingly slower rates as the pressure declines. The volume evolves from an initial pancake shape into a more rounded shape, as illustrated in Fig. 8(b). The increase in the thermal resistance due to the widening gap will become significant after time τ_u and result in an increasingly smaller proportion of the laser energy delivered to the underwater front. The part of the air front in direct contact with the laser beam will continue to travel at a high speed while the remaining fronts lose pressure and slow down, as illustrated in Fig. 8(c). The pressure gradient which subsequently develops will tend to drive gas into the water. The gas driven into the water by the pressure gradient will collect into a bubble which may oscillate, causing one or more subsequent bubble pulses.

High speed photography of the interaction of a high power laser with a water surface by Emmony, Geerken, and Straaijer[6] clearly shows the development of the later stages of the blast. Their photographs show the development of a spherical blast whose center is well above the interface. Later, when the effects of thermal resistivity become significant, they show the part of the air front that is in direct contact with the laser beam continuing to rise to great heights, while the expansion rate of the main volume declines. Finally, a gas bubble is driven below the water surface. Their photographs also show subsequent bubble activity which is beyond the scope of this blast model.

7.   Underwater Acoustic Output

In the case where the blast is weak, the velocity of the underwater front will be approximately equal to that of small amplitude acoustic waves. The effective intensity I_u will drop below the minimum requirement early in the one-dimensional stage. At this point, the front will have moved a negligible distance, and therefore all the significant pressure changes may be considered as taking place at the interface. As an acoustic source, it may be modeled as a planar pressure transducer. Since the pressure is weak, linear superposition may be applied, and thus the acoustic signal at a distant point may be simply

constructed through a Green's function integral. Thus the acoustic pressure $p(r)$ at a point r is given by the surface integral

$$p(r) = \int_{-\infty}^{\infty} \int_{-\infty}^{\infty} (dp_u(t - |r\text{-}s|/c_o)/dt)/(|r\text{-}s|\rho_o)\ ds\ , \tag{67}$$

where $p_u(t - |r\text{-}s|/c_o)$ is the time retarded underwater pressure and s is a general point on the interface. This approach was taken in the previous study.[22] This allowed the optoacoustic process to be studied without the complication of nonlinear acoustic propagation effects.

In the case of a strong blast, the underwater front will continue to be driven well after τ_u, that is, well into the conduction limited condition. To obtain a better understanding of the acoustic generation process, let us look more closely at the development of the underwater front, particularly at the heat flow to the front and the shock front itself.

Let us consider the blast gases behind the underwater front. In the conduction limited condition, the energy deposited by the laser beam cannot be instantaneously distributed. Therefore a significant concentration of heat energy will build up in the collection volume. Since energy collection takes place at the air front, the collection volume is the volume occupied by the laser beam that has been swept by the air front. For a circular laser beam directed vertically downward, the collection volume is a vertical cylinder starting at the interface and terminating at the air front, as shown in Fig. 9. Therefore the governing process controlling the development of the underwater front is the heat diffusion from the cylindrical reservoir, particularly through its bottom end. The problem of heat diffusion is one that satisfies Laplace's equation, and may be solved by standard methods in the static case. From the geometry of the problem, it can be seen that, for a point on the underwater front directly below the reservoir, the downward diffusion from the curved sides of the reservoir will be small compared to that from the flat bottom end. Neglecting the diffusion from the curved sides, the problem becomes one of diffusion from a circular plate. In this case, the solution of the static problem is very simple: Using a

45
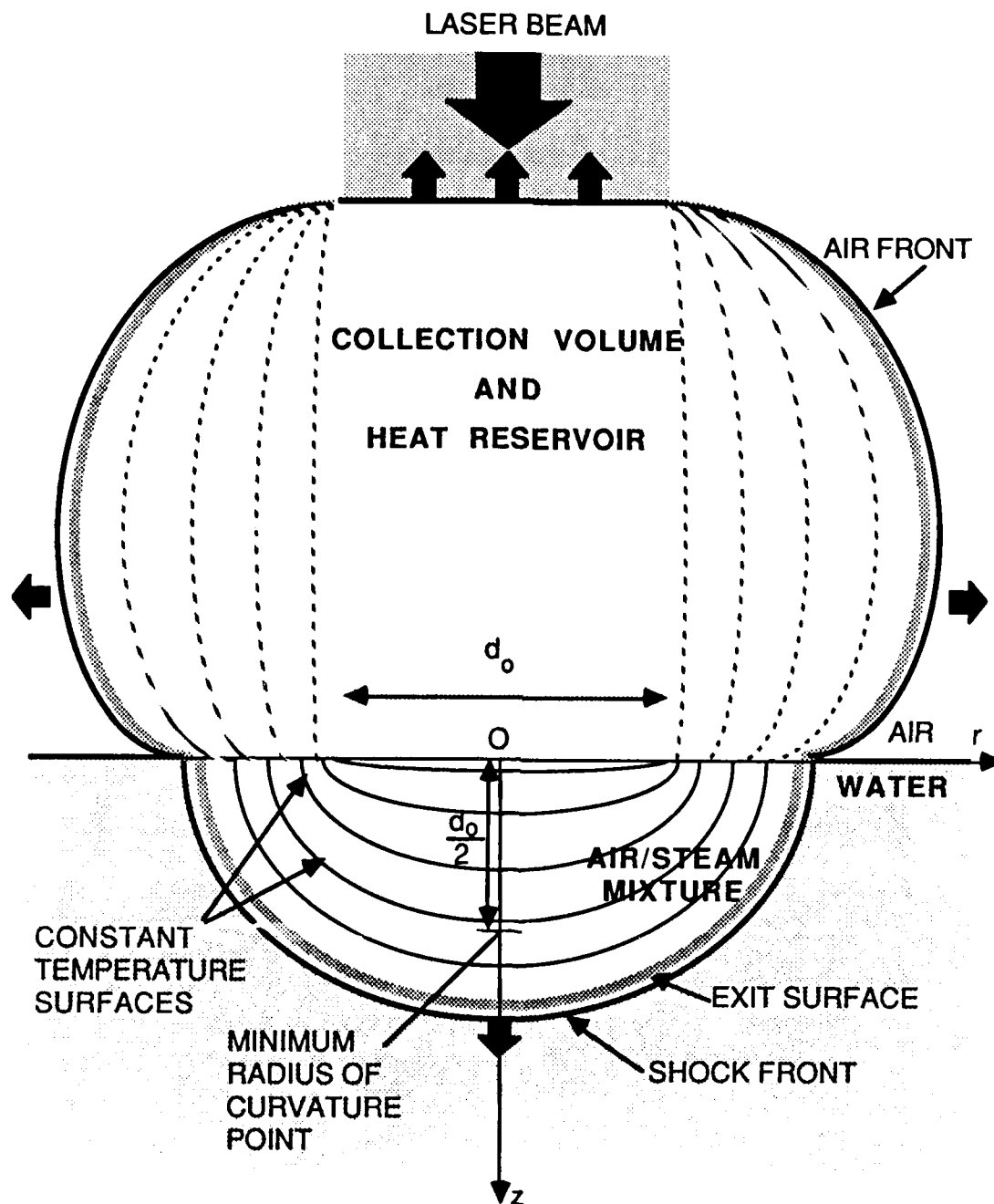
FIGURE 9
ELLIPSOIDAL SURFACES IN THE UNDERWATER FRONT
IN THE CONDUCTION LIMITED CONDITION

conformal transformation technique,[29,30] it may be shown that the lines of flux are confocal hyperbolae that are orthogonal to confocal ellipsoid constant temperature surfaces, as illustrated in Fig. 9. Thus the underwater constant temperature surfaces will tend to conform to the confocal ellipsoid surfaces, since any deviation from this basic shape would be accompanied by a corrective change in the heat input rate. The foci are located on the rim of the circular heat reservoir. Assuming that the diameters of the heat reservoir and the laser beam are approximately equal, the general equation of the constant temperature surface, for a laser beam of diameter d_o, is given by

$$z^2 = (q/2)^2 - (d_o/2)^2 - r^2(1 - (d_o/q)^2) , \qquad (68)$$

where z is the depth of a point on the constant temperature surface and r its radial distance from the vertical axis of symmetry; q is the independent parameter.

On the vertical axis of symmetry, i.e., at r=0, the radius of curvature R_c of the ellipsoid is given by

$$R_c = -1/(d^2z/dr^2)$$

$$= (q/2) (1 - (d_o/q)^2)^{-1/2} . \qquad (69)$$

Differentiating R_c with respect to q and setting the result equal to zero, it is found that the value of R_c has a minimum of d_o, which occurs at $q = d_o\sqrt{2}$. Substituting for q in Eq. (68) and setting r to zero, it is found that the minimum radius of curvature occurs at $z=d_o/2$.

Initially, the underwater front is modeled as a perfect surface of discontinuity, where the fluids enter and exit an infinitely thin transformation zone. In the one-dimensional stage, the underwater front is a shock front, driven through the water by hot gases from behind, traveling at a constant speed and in a state of dynamic equilibrium. As the front enters the conduction

limited condition, its input intensity I_u declines and therefore it is no longer able to process the incoming fluids at the same rate. As a consequence two things will happen: (1) the front will slow down and (2) it will "thicken", i.e., the exit surface, or gas boundary, will begin to lag behind the shock front, eventually giving way to the complete separation of a self-contained shock pulse from the gas bubble. There will be strong pressure and particle velocity gradients in this zone. Since the particle velocities in a strong shock front are quite substantial, there is a case for treating the dynamics in this zone in terms of a flow field rather than a wave field. Numerical results of η from the case studies shown in Table II indicate that the change in the density of water caused by the underwater shock front is extremely small. Therefore the velocity field of the particle motion may be regarded as nearly incompressible. Since the flow field of an inviscid and incompressible fluid also obeys Laplace's equation, it is expected that the evolution of the shock front will also have a tendency to conform to the confocal ellipsoid model, as illustrated in Fig. 9. In the limit as the parameter q in Eq. (68) tends to infinity, the ellipsoid will become a sphere. Thus, the ellipsoid model will allow the shock front to smoothly develop into a spherical front in the farfield.

Therefore, it is argued that the ellipsoid model is the asymptotic model that the underwater front will tend towards, in the limiting case of extremely high heat flow rates in the blast volume and high particle velocities behind the shock front. In practice, it serves as a useful but approximate model.

From studies of underwater explosions,[24] there are only a few main characteristic quantities that define the final spherically spreading shock front, the initial peak pressure, the radius of curvature, and the rate of decay (or time constant). The theoretical results developed in the foregoing section may be used to estimate these characteristic quantities. The propagation of the shock wave may then be modeled as that of a simple spherical shock for which the pressure and time constant variations have been theoretically analysed by several researchers. For the purposes of this analysis, the results of Rogers[31] will be used. The expressions for shock peak pressure p_m and time constant τ,

48

in terms of the initial values of range R_o, pressure p_o, and time constant τ_o, are given by

$$p_m = p_o \{[1 + 2(R_o/\lambda_o)\ln(R/R_o)]^{1/2} - 1\}/[(R/\lambda_o)\ln(R/R_o)] \quad , \tag{70}$$

$$\tau = \tau_o [1 + 2(R_o/\lambda_o)\ln(R/R_o)]^{1/2} \quad , \tag{71}$$

where the characteristic length λ_o is given in terms of the coefficient of nonlinearity β (value 3.5 for water) and the initial values by

$$\lambda_o = p_o c_o^3 \tau_o / \beta p_o \quad . \tag{72}$$

The initial peak pressure p_o will be taken as equal to the initial blast pressure as formulated in Eq. (29). The initial range R_o will be taken as equal to the radius of curvature R_c of the ellipsoid model at its minimum point. In the vertically downwards direction, it was found through Eq. (69) to be equal to the diameter of the laser beam d_o, giving

$$R_o = d_o \quad . \tag{73}$$

The initial time constant τ_o will be obtained from the asymptotic decay rates as given by Eqs. (59) and (66) by equating the impulses of the exponential pulse of the Kirkwood-Bethe model[24] and that of the above model. The impulse I_{KB} in the Kirkwood-Bethe model is given by

$$I_{KB} = \int_0^\infty p_u \, d\tau = \int_0^\infty p_{uo} \, e^{-t/\tau_o} \, d\tau = p_{uo}\tau_o \quad . \tag{74}$$

The impulse I_g in the above model is given by

$$I_g = \int_0^\infty p_u \, d\tau \rightarrow p_{uo}\tau_u + \int_{\tau_u}^\infty p_{uo}(t/\tau_u)^{-4/3} \, d\tau = 4p_{uo}\tau_u \quad . \tag{75}$$

Equating I_{KB} and I_g, the result is simply

49

$$\tau_0 = 4\tau_u \ . \tag{76}$$

Applying the commonly used approximation that the final shock pulse is also similar to an exponential function, the values of the peak pressure p_m and time constant τ may be used to obtain approximate but simple estimates of the magnitude and the roll-off of the shock pulse energy density spectrum $|P(\omega)|^2$, giving

$$|P(\omega)|^2 \approx (p_m\tau)^2/(1 + (\omega\tau)^2) \ ; \qquad \text{for } 0 << \omega \ . \tag{77}$$

Numerical results for the three case studies of the initial and final values of the key parameters are shown in Table IV; in the example shown, the final values refer to a point of observation 1 m directly below the blast. The figures for case 1 are in brackets since they would only apply if the laser intensity in case 1 were adequate, i.e., about 14 times (1359%) higher than the stated value in Table III. It is interesting to note that, while the initial peak pressure is highest in case 3, the final pressure is not. This is due to its smaller initial radius of curvature. Of the three cases, the case that is predicted to deliver the highest peak pressure and spectrum density level is case 2. Case 1 proved to be a non-starter; the case 1 values in brackets are not applicable because they are computed for a laser power that is 14 times higher than the stated value.
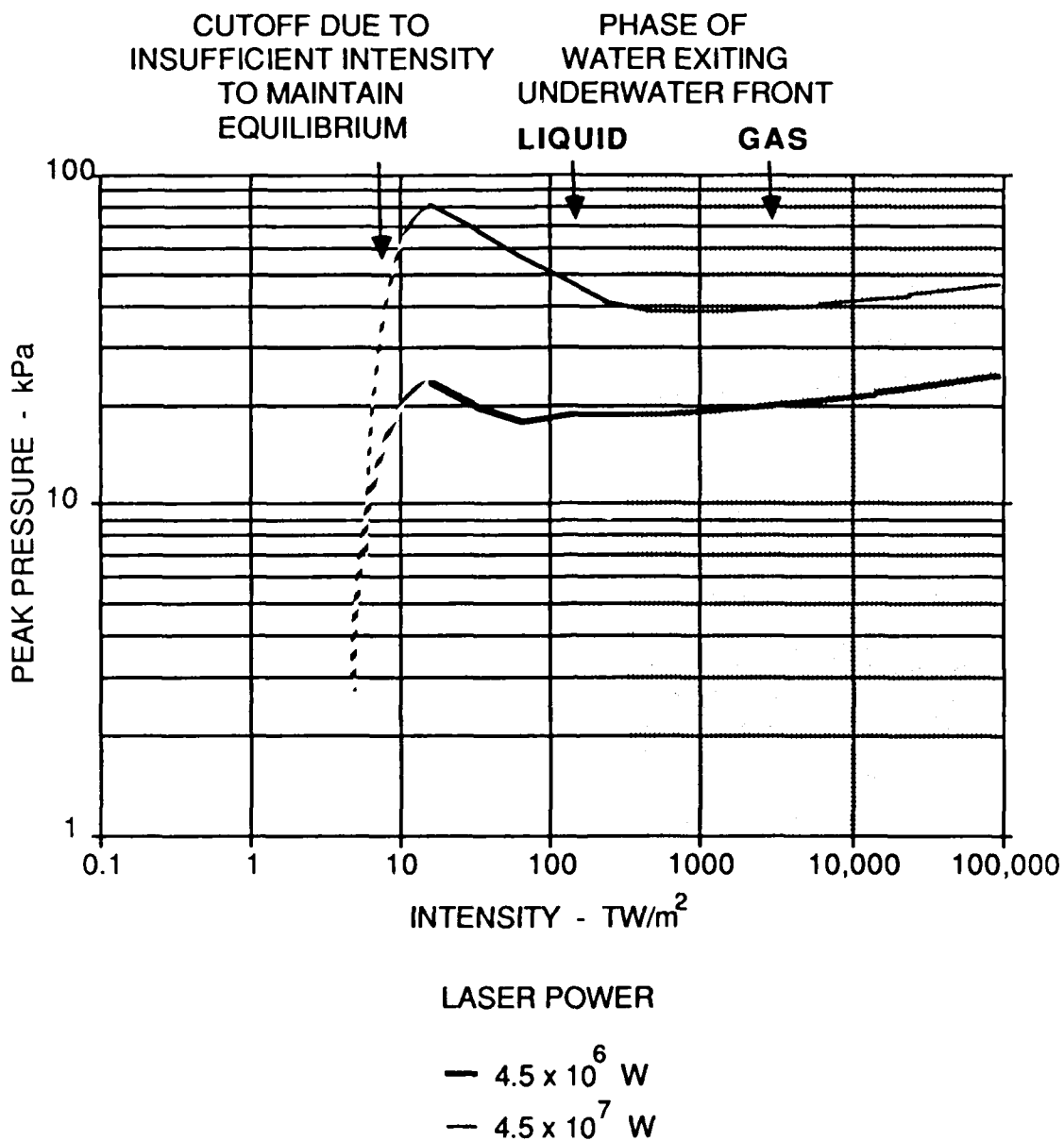
In Fig. 10 a plot of the predicted acoustic peak pressure, for the point 1 m directly below the blast, as a function of intensity is shown. The laser power is assumed to be constant and the intensity is varied by changing the spot size. Two curves are shown, one for a laser power of 4.5 MW which is the power delivered by our Nd:glass laser, and a second curve for a laser power that is ten times higher. It was found that above an intensity of 300 TW/m^2 the fluid exiting the underwater front is predicted to be steam. Below this intensity, it is liquid water which is subsequently turned into steam on contact with the hot air from the air front. It is seen that below intensities of about 10 TW/m^2, there is insufficient intensity to maintain the equilibrium within the blast, that is, to drive

TABLE IV

EQUILIBRIUM BLAST MODEL CASE STUDIES: ACOUSTIC OUTPUT

CASE STUDIES		1	2	3
Spot diameter	m	0.0032	0.00066	0.00017
Spot area	m^2	8.0E-6	3.4E-7	2.3E-8
Incident intensity	W/m^2	5.6E+11	1.3E+13	2.0E+14
Energy density	MJ/m^2	0.03	1.0	14
ACOUSTIC OUTPUT :				
t_o	s	(5.4E-07)	3.4E-08	9.0E-09
Initial peak pressure	Pa	(1.3E+7)	1.3E+8	1.1E+9
l_o	m	(4.3E-02)	2.7E-04	8.3E-06
R_o (vertical case)	m	(3.2E-3)	6.6E-4	1.7E-4
R	m	(1)	1	1
Time constant at R: t	s	(7.3E-7)	2.1E-7	1.7E-7
Peak pressure at R: p_m	Pa	(3.5E+4)	2.4E+4	1.9E+4
Spectrum level dB re 1 W/m^2/Hz re 1 m		(-94)	-108	-112
Upper cutoff frequency	MHz	(0.21)	0.78	0.94

The figures for case 1 are in brackets because they represent the values that would have been obtained had there been enough laser power to drive the process.

CUTOFF DUE TO
INSUFFICIENT INTENSITY
TO MAINTAIN
EQUILIBRIUM

PHASE OF
WATER EXITING
UNDERWATER FRONT

LIQUID   GAS

LASER POWER

— 4.5×10^6 W
— 4.5×10^7 W

FIGURE 10
THEORETICAL PREDICTION OF PEAK ACOUSTIC PRESSURE
AS A FUNCTION OF INTENSITY AT 1 m BELOW BLAST CENTER

the fronts at the maximum entropy condition and sustain the pressure equilibrium within the blast interior. It is possible that a pressure wave may still be generated outside blast equilibrium conditions; therefore, in practice, the pressure is not expected to decay quite so abruptly with intensity. It is seen in Fig. 10 that acoustic pressure maxima occur at the minimum intensity (maximum spot size) required to sustain an equilibrium blast.

In Fig.11, a similar plot of the low frequency spectrum levels is shown. The low frequency spectrum estimate is based on the assumption of an exponential shock function. Under this assumption, the low frequency end of the acoustic pressure Fourier transform is approximately constant, given by the product of the peak pressure and the time constant.

Assuming that the radiated acoustic energy approximately follows a dipole directivity pattern, the total acoustic energy radiated, at a range of 1 m, was estimated. The acoustic energy was divided by the useful laser energy, giving a measure of the energy conversion efficiency for a range of 1 m; the useful laser energy is defined as the stated laser power times the useful pulse length which is estimated to be $8\tau_u$, where τ_u is the pressure decay time constant as defined by Eqs. (65) and (66). The plots of efficiency as a function of spot size and intensity are shown in Fig. 12(a) and (b). Also shown are plots of efficiency for the acoustic energy in the band 0-50 kHz; this band was chosen because it covers a broad range of sonar applications. It is seen in Fig. 12(a) that, below the minimum spot size required to generate steam within the blast interior, the fullband efficiencies are practically independent of the laser power, with a minimum value of approximately 0.04%. It is also seen that the 0-50 kHz band efficiencies are about 10 times lower and increase only slowly with laser power. It is also seen in Fig. 12(b) that the efficiency in the 0-50 kHz band is independent of laser power above intensities of about 100 TW/m^2.
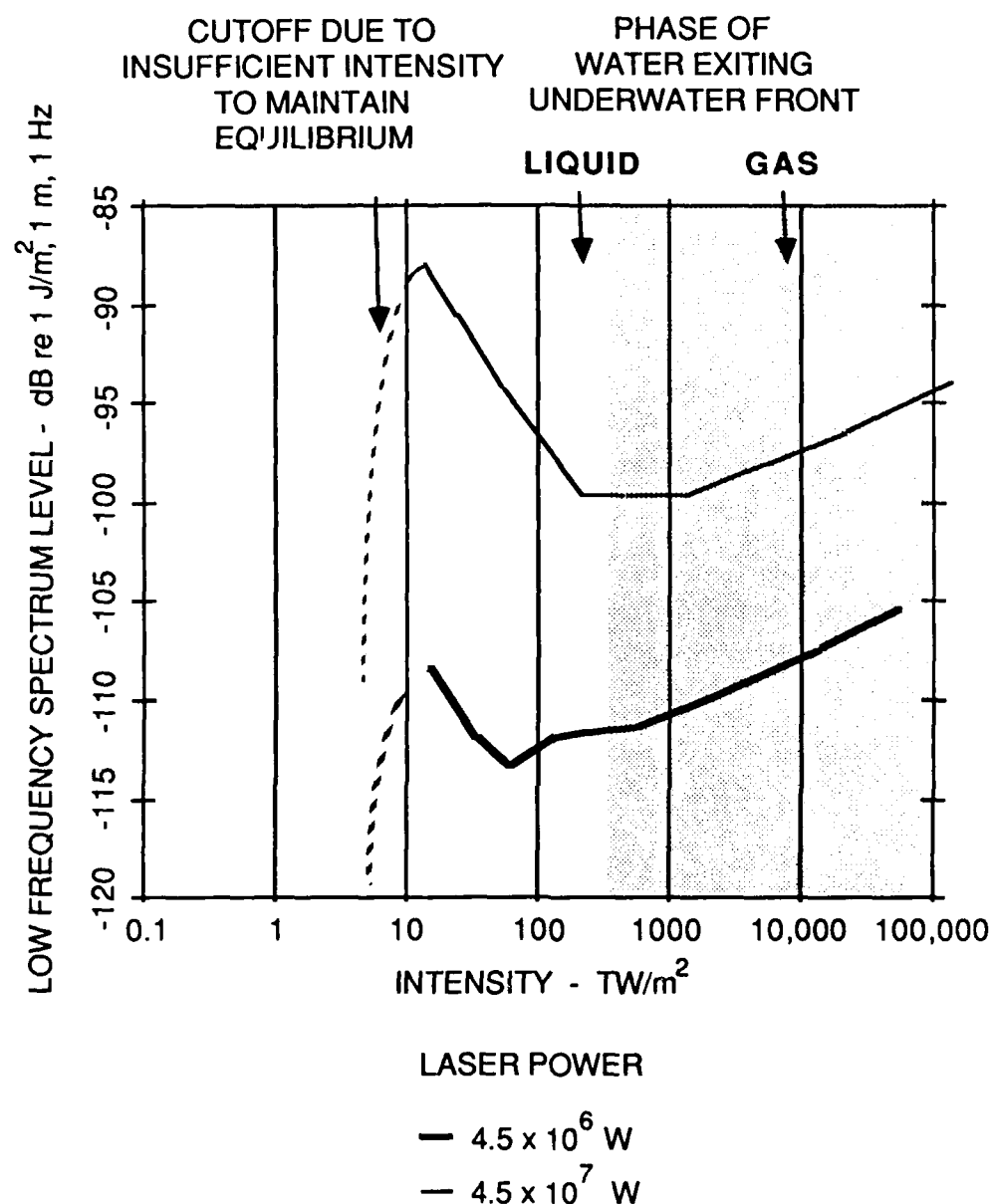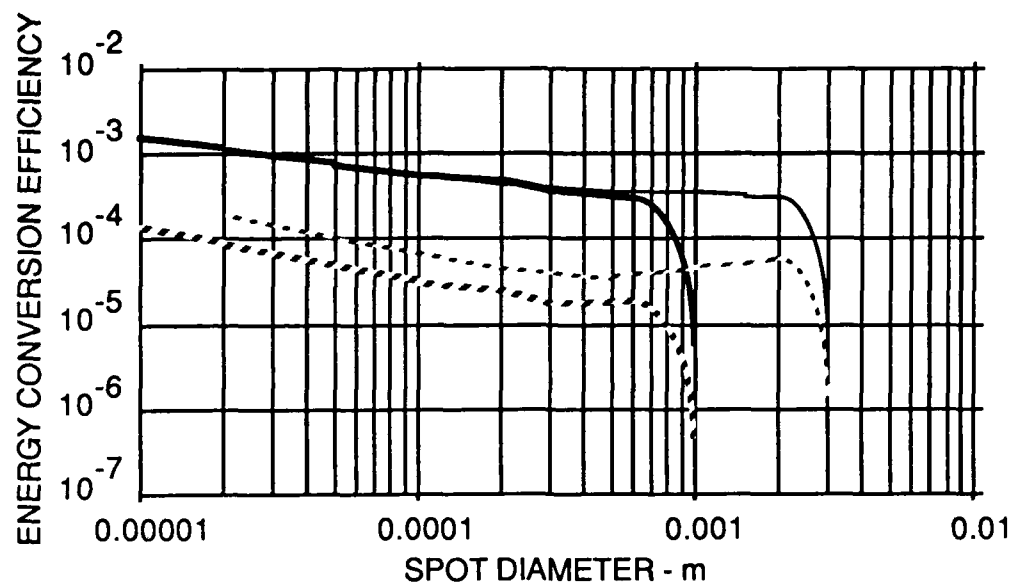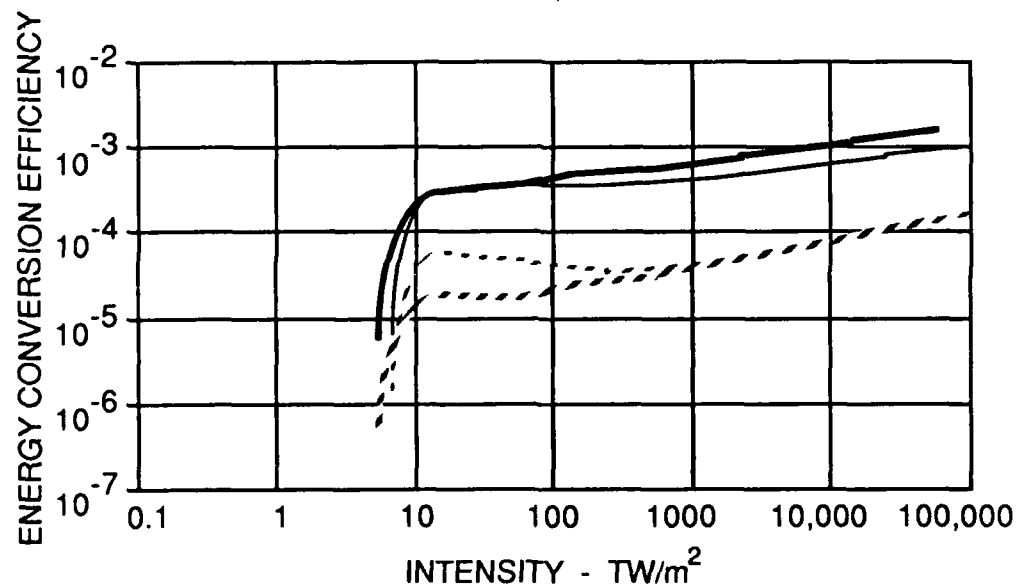
FIGURE 11
THEORETICAL PREDICTION OF LOW FREQUENCY SPECTRUM
OF ACOUSTIC OUTPUT AS A FUNCTION
OF INTENSITY AT 1 m BELOW BLAST CENTER

54

FIGURE 12
THEORETICAL PREDICTION OF ENERGY CONVERSION EFFICIENCIES
AS A FUNCTION OF (a) LASER SPOT SIZE AND (b) INTENSITY,
AT A RANGE OF 1 m

III. EXPERIMENT

A. Apparatus

The apparatus is shown in Fig. 13. The laser used is an Apollo Nd:glass laser model 22/A with a maximum pulse energy of 22 J. The laser beam was directed vertically down by a prism and focused on the water surface. With appropriate topside lenses, it is capable of producing a spot size of approximately 8 mm^2 (diameter 3.2 mm) at the water surface. With converging lenses nearer the water surface, spot sizes of 0.023 and 0.342 mm^2 (diameters 0.17 and 0.66 mm) were also obtained. A short laser pulse was achieved by using a Inrad model 2-016 Q-switch driver to modulate the Pockels cell in the laser cavity. The laser pulse was approximately 0.15 μs long and a train of up to five pulses at a maximum repetition rate of 10,000 pps could be delivered. The maximum laser pulse energy delivered at the water surface per pulse was 0.7 J. Silicon PIN photodiodes were used to monitor the laser pulse through fiber-optic probes. The acoustic detectors used included a E8-59 hydrophone and a PCB138A01 tourmaline shock probe. The acoustic signal was recorded at a number of different observation angles q. The control circuit determined the number of pulses and the timing between pulses. The data, both optical and acoustic, were recorded on a Nicolet 4094A digital oscilloscope.

Direct viewing of the reaction at the water surface was not possible due to the speed of the process and the strong optical emission. Therefore, snapshots of the activity on the water surface were made photographically. The apparatus is shown in Fig. 14. The real image of a grid pattern is projected on the water surface and captured on film using a polaroid camera. Any disturbance on the water surface is manifested as a distortion in the grid image. By strobing the grid with a flash lamp, the disturbances on the water surface at a particular instant may be captured. Since the camera shutter was opened before the start of the optoacoustic process, any optical emissions in the visible range from the surface produced at the time of the laser pulse arrival were also captured on the film.
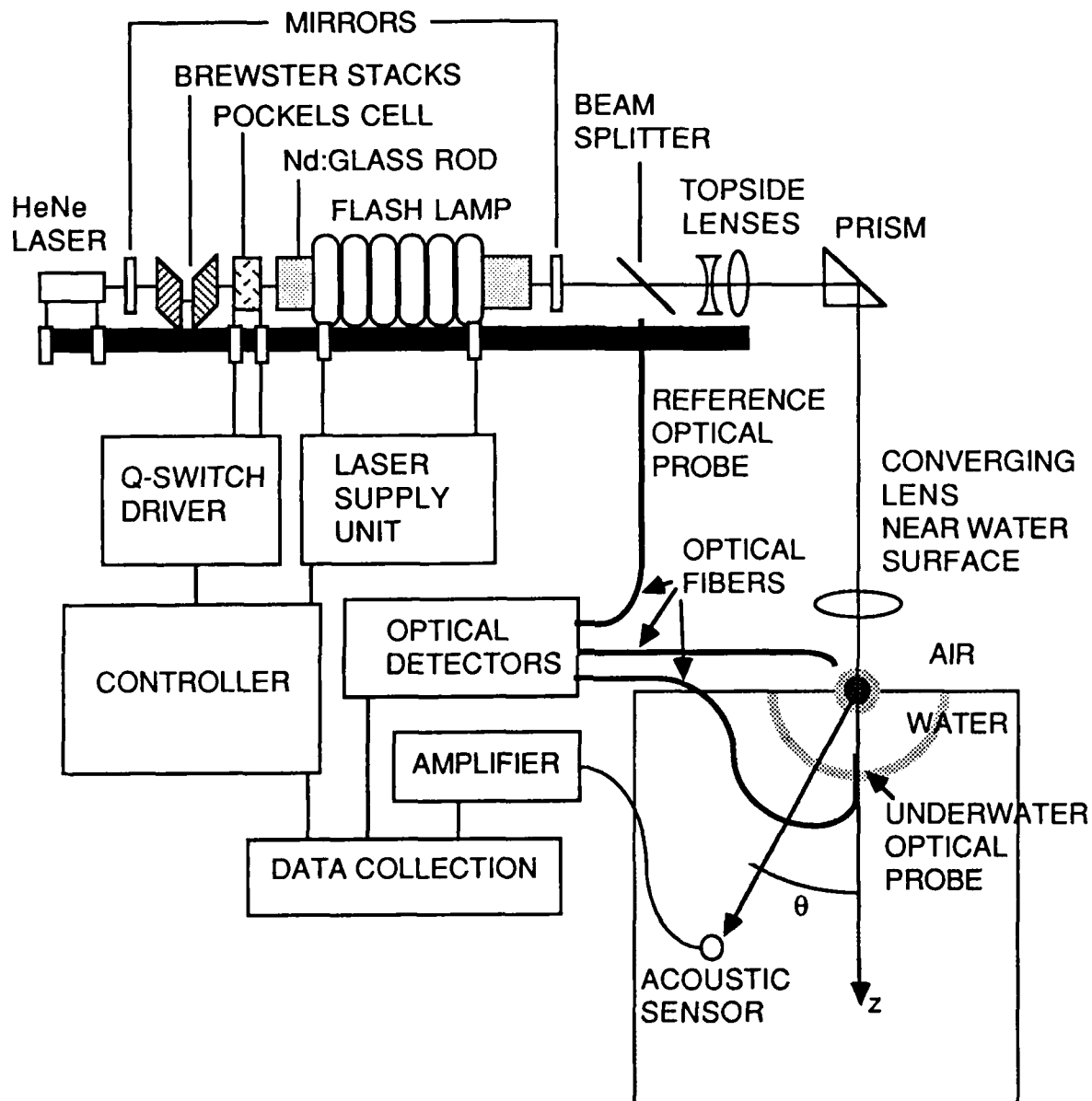
FIGURE 13
EXPERIMENTAL APPARATUS
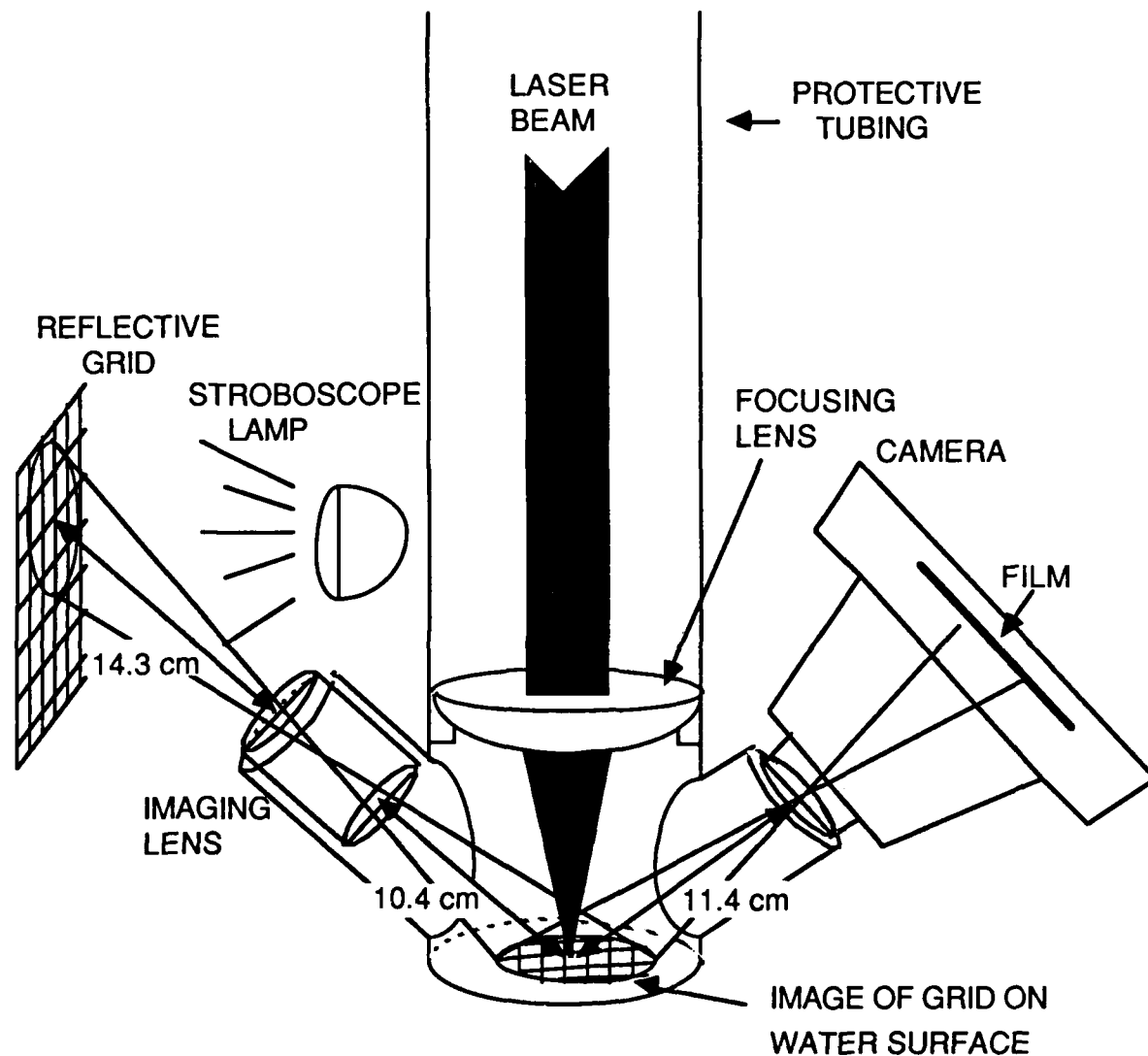
FIGURE 14
PHOTOGRAPHIC APPARATUS TO RECORD SURFACE ACTIVITY

B. Acoustic and Photographic Data

Let us begin by comparing the experimental results with the linear thermoacoustic theory, which assumes that the acoustic signal is produced by simple thermal expansion of the medium, since this is the best understood mechanism of optoacoustic sound generation. From linear thermoacoustic theory,[1,3] the acoustic signal spectral density $|P(\omega)|^2$ is given by

$$|P(\omega)|^2 = |W(\omega)|^2 (kC_a D_a /r_o)^2 \exp(-2\alpha r_o) , \tag{78}$$

where

$W(\omega)$ = the Fourier transform of the laser power function,

k = acoustic wave number,

α = acoustic absorption coefficient,

r_o = range from optoacoustic source,

C_a = thermoacoustic conversion constant, determined by physical constants, including specific heat, thermal expansion coefficient, etc., and

D_a = diffraction loss, determined by the geometry and orientation of laser beam, the laser beamwidth, and absorption length.

Dividing both sides of Eq. (78) by the square of the laser energy, which is identically $W(0)$, we get

$$|P(\omega)/W(0)|^2 = |W(\omega)/W(0)|^2 (kC_a D_a /r_o)^2 \exp(-2\alpha r_o) . \tag{79}$$

The right hand side of Eq. (79) is now independent of the laser energy $W(0)$. It is dependent on the width of the laser beam through the term D_a and on the shape of the laser pulse through the normalized spectrum function $|W(\omega)/W(0)|$. In the farfield and on the vertical axis directly below the optoacoustic source, it can be shown that the term D_a is independent of the laser beamwidth. The shape of the laser pulse was kept constant throughout the experiment. Under these conditions, $|P(\omega)/W(0)|^2$ is only dependent on

60

physical constants; therefore it makes a good metric for studying the optoacoustic conversion characteristics.

In Fig. 15, representative experimental measurements of $|P(\omega)/W(0)|^2$ are shown along with the theoretical thermoacoustic characteristic curve. The acoustic sensor was at a depth of 1 m directly below the source point. Results are shown from four very different laser surface energy density levels, i.e., laser energy delivered to the water surface divided by beam cross-sectional area at the water surface. The results show that at 0.013 MJ/m^2 there is good agreement with the thermoacoustic theory for the most part. The discrepancies, wherever they occur, tended to exceed the theoretical estimate; therefore it is deduced that the linear thermoacoustic theory must be close to the limits of its validity. At 0.03 MJ/m^2 and higher energy densities, it is seen that the acoustic outputs were significantly higher than that predicted by the thermoacoustic theory. At 14 MJ/m^2, the acoustic output exceeded that predicted by the thermoacoustic theory by more than 50 dB.

At the lowest energy densities, the acoustic pulse (not shown) was found to have the characteristic N-shape of the bandlimited time derivative of a delta function, which is as predicted by the linear thermoacoustic theory. The corresponding acoustic pulses for the remaining energy density levels are shown in Figs. 16, 17, and 18. At 0.03 MJ/m^2 and using the E8-59 hydrophone, the pulse is a corrupted figure of N, as shown in Fig. 16, indicative of nonlinearities. At the higher laser energy densities, the signal was considerably stronger; thus it was possible to use the tourmaline gauge shock probe and take advantage of its greater bandwidth. At 1 MJ/m^2 and 14 MJ/m^2, as shown in Figs. 17 and 18, the positive shock peaks are estimated to have time constants of about 2 μs. This is probably due to the limited response time of the shock probe, which is claimed by the manufacturer to be 1.5 μs. Therefore, the true acoustic peak pressure is likely to be higher than that shown. With hindsight, a faster probe, such as a PVDF film, would have been a better choice. At 14 MJ/m^2, as shown in Fig. 18, there is significant clipping and stretching of the rarefaction phase due to cavitation limitation.
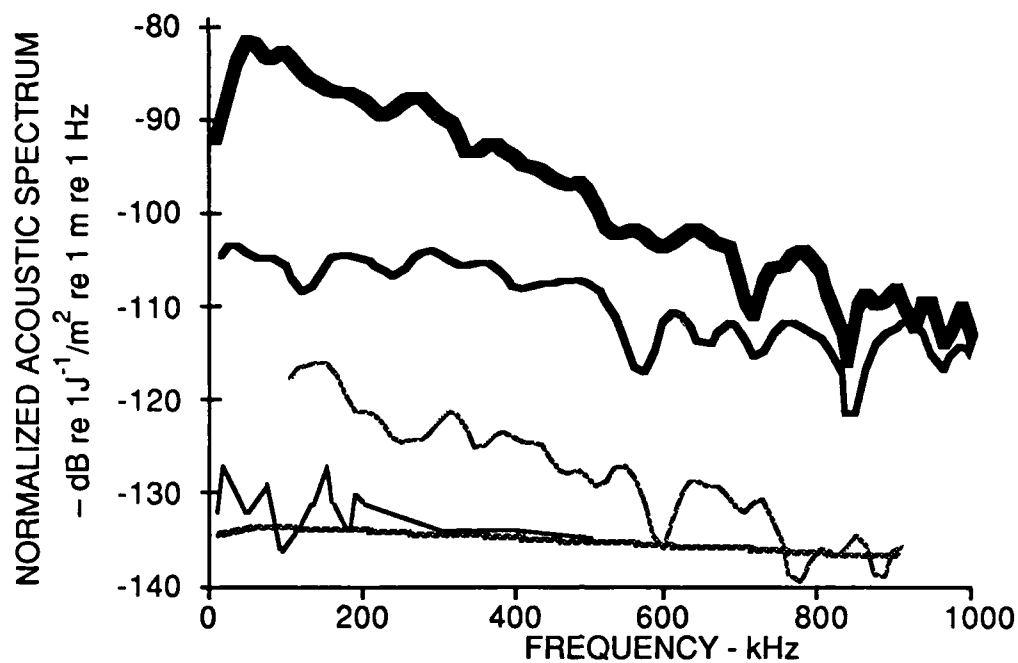
FIGURE 15
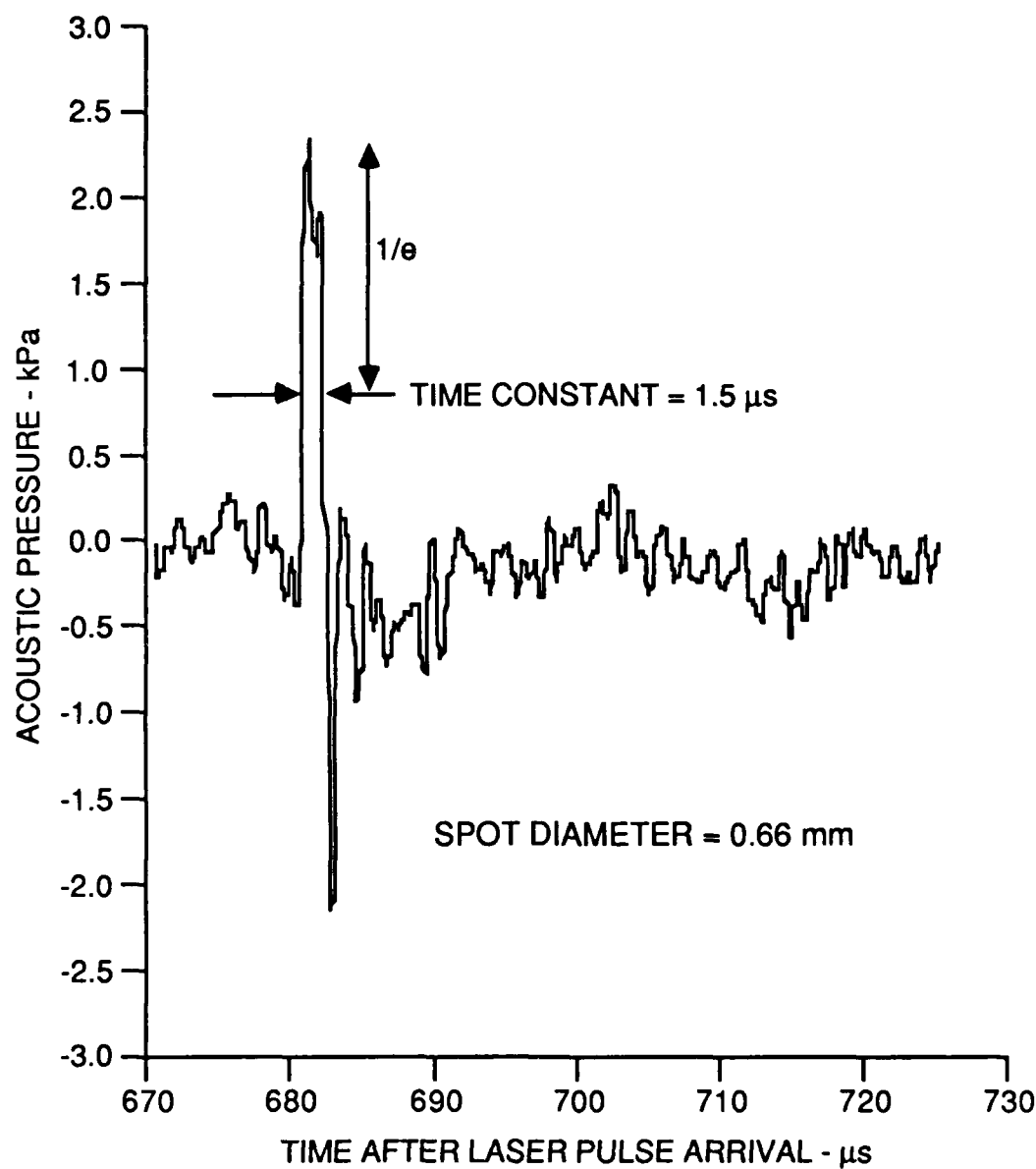**COMPARISON OF THE EXPERIMENTALLY MEASURED NORMALIZED**
ACOUSTIC SPECTRA AT 1 m BELOW THE SOURCE
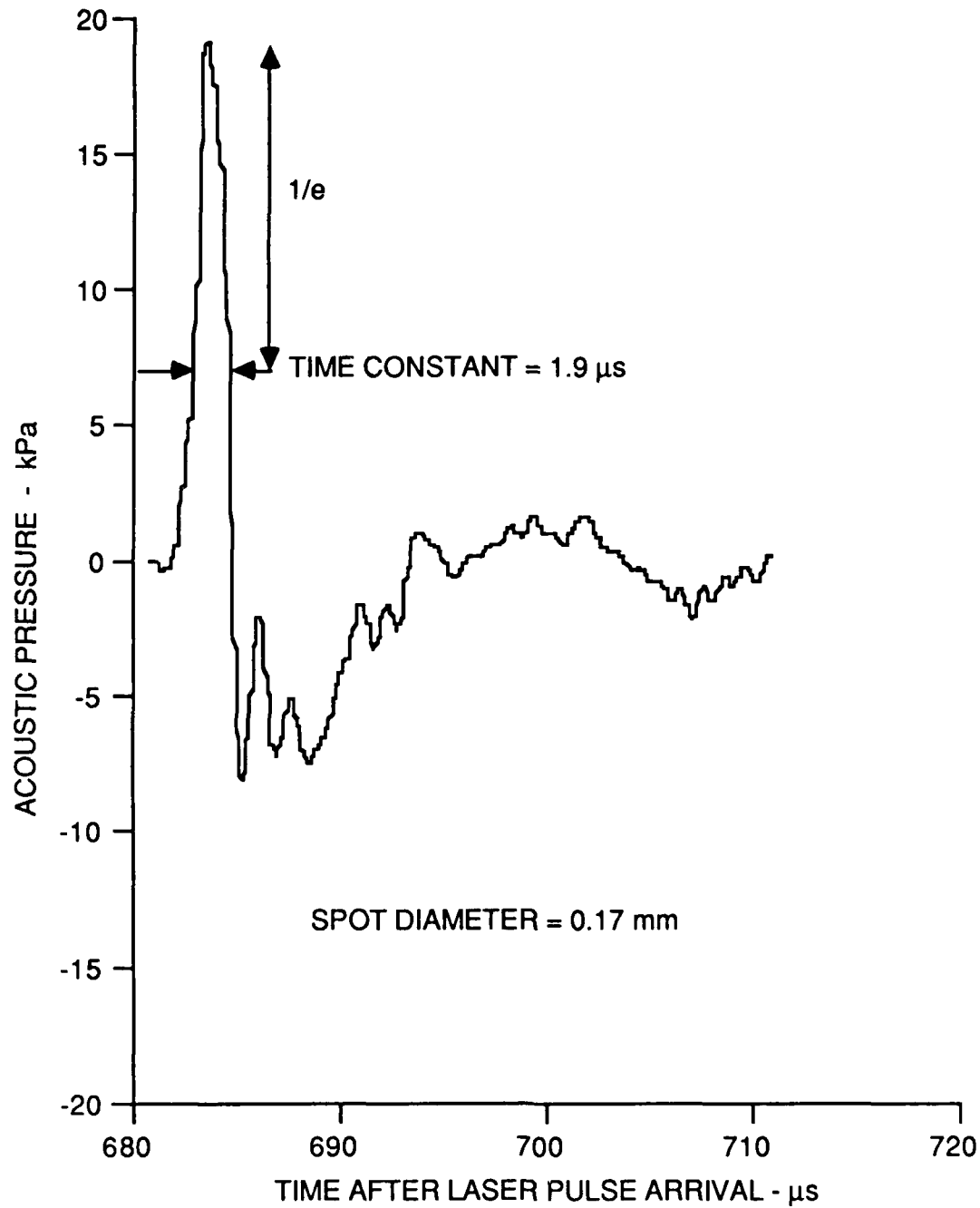**AT VARIOUS LASER ENERGY DENSITIES AND INTENSITIES**
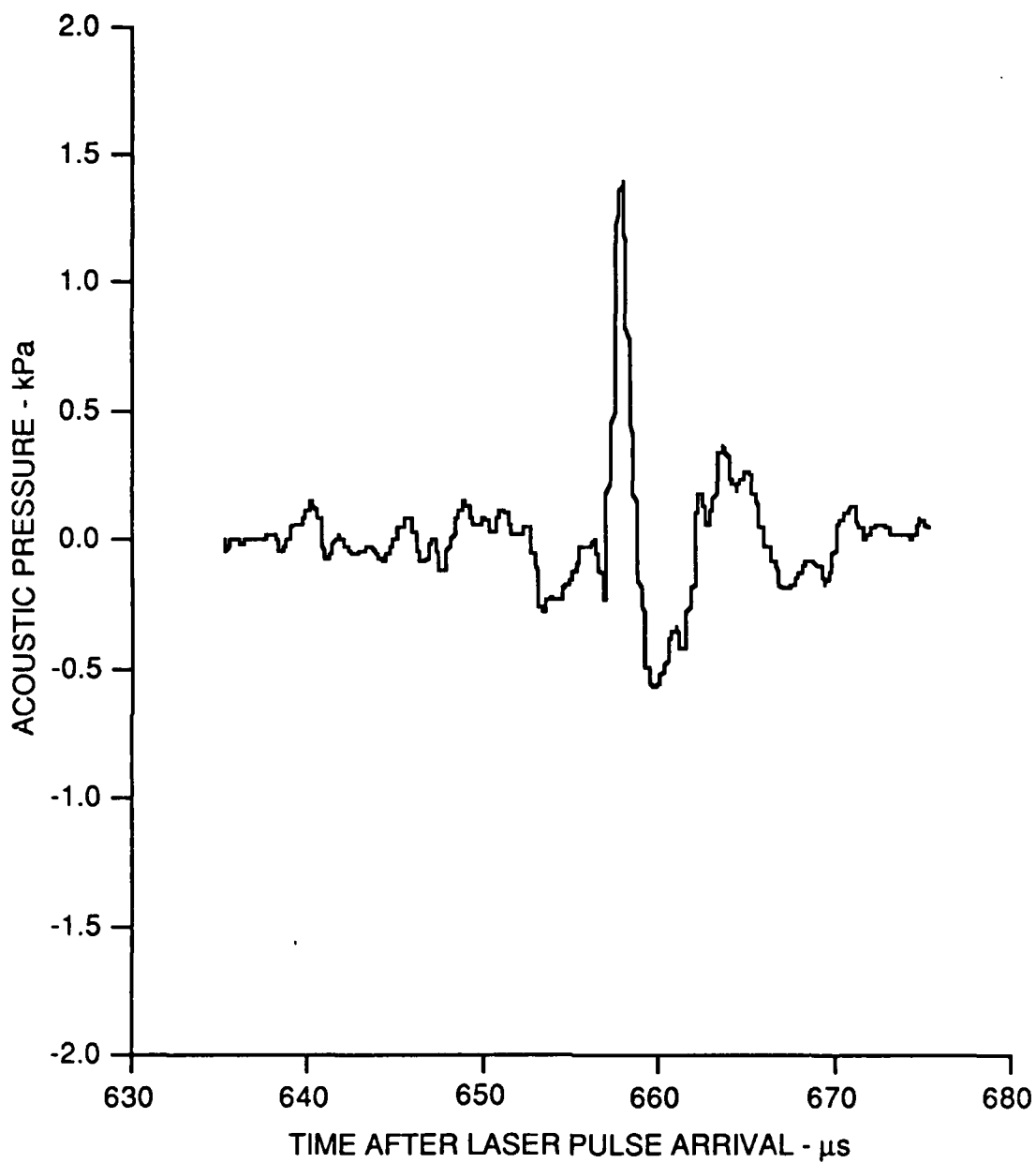
FIGURE 16
ACOUSTIC PULSE AT A LASER ENERGY DENSITY OF 0.03 MJ/m^2
AND INTENSITY 0.56 TW/m^2

63

FIGURE 17
**ACOUSTIC PULSE AT A LASER ENERGY DENSITY OF 1 MJ/m^2**
AND INTENSITY 13 TW/m^2

FIGURE 18
ACOUSTIC PULSE AT A LASER ENERGY DENSITY OF 14 MJ/m^2
AND INTENSITY 200 TW/m^2

C. Comparison with the Equilibrium Blast Model

From photographic observations of the water surface, obtained using the apparatus described in Fig. 14, it was found that at energy densities 0.013 and 0.03 MJ/m^2 there were no detectable surface deformations. An example of the photograph of the grid image on the water surface under these conditions is shown in the Fig. 19. As the energy density levels approached 1 MJ/m^2, some disturbances were observed. Occasionally, as shown in Fig. 20, the photograph would show secondary emission from the laser spot; the laser itself is invisible to the film. Other times, as shown in Fig. 21, there would be a bright spot and weak ripples. At 1 MJ/m^2, for most of the time, the observed surface image is as shown in Fig. 22. This photograph shows a bright and explosive optical emission from the water surface where the laser beam made contact. It is also seen that there are several concentric ripples. The photograph clearly shows that an explosive reaction has taken place. At 14 MJ/m^2 the ripple structure is quite different, having only one large ripple and a plume rising vertically out of the water, as shown in Fig. 23. The plume is not easily seen, but its shadow is clearly visible in the foreground. In all the photographs, the grid was strobed at 10 ms after laser contact; therefore the surface ripples appear as they were at that instant. The optical emissions, however, could have occurred at any time up to 30 ms after the laser arrival since the camera shutter was left open during that interval.

The many concentric ripples seen in Fig. 22 are of particular interest. A mathematical analysis of the water waves produced by explosions was made by Kranzer and Keller.[32] Their analysis was done in terms of the impulse distribution on the water surface. For the case where the impulse is a nonzero constant within a circular area and zero outside, they showed that there will be a large number of concentric ripples of approximately equal amplitude. It has been shown in Eq. (66) of the blast model that most of the impulse is delivered within a time of $4\tau_u$. In many cases, the lateral boundaries of the air and underwater fronts will not have significantly expanded in that time; from the figures under case 2 in Table II and III, it can be seen that this is particularly

66
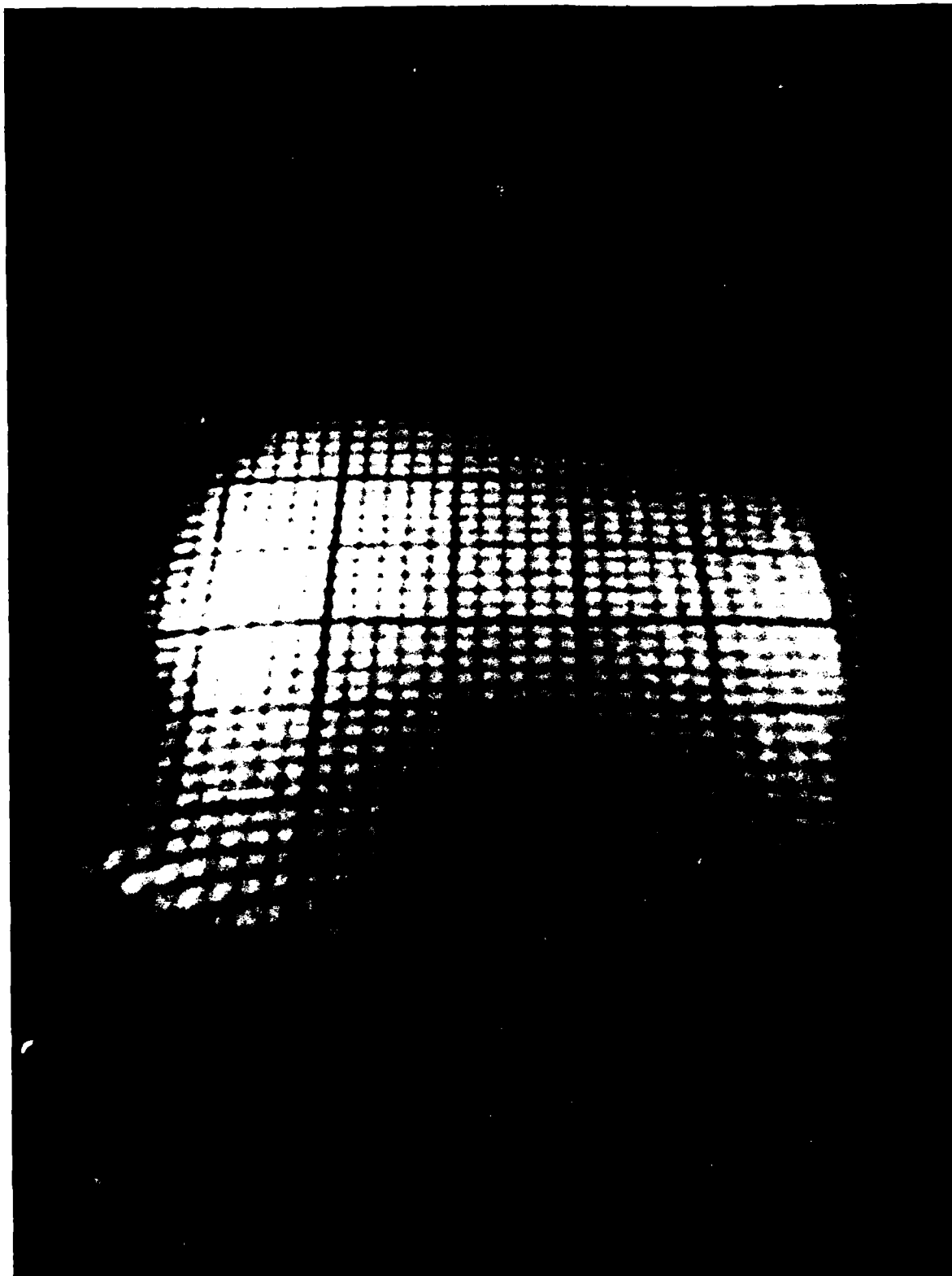
FIGURE 19
UNDISTURBED WATER SURFACE
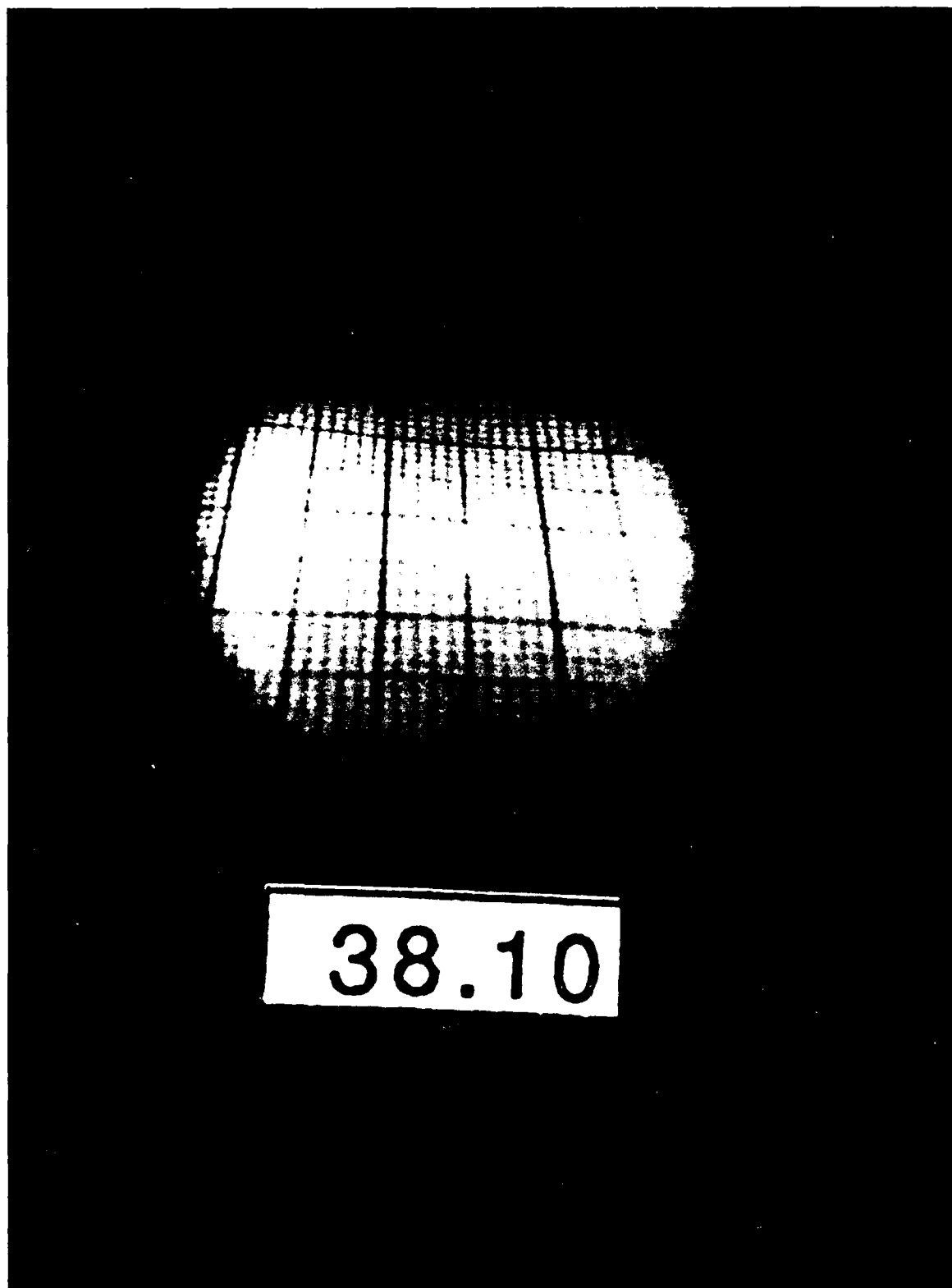**AT A LASER ENERGY DENSITY OF 0.03 MJ/m^2**

67

4999-24A

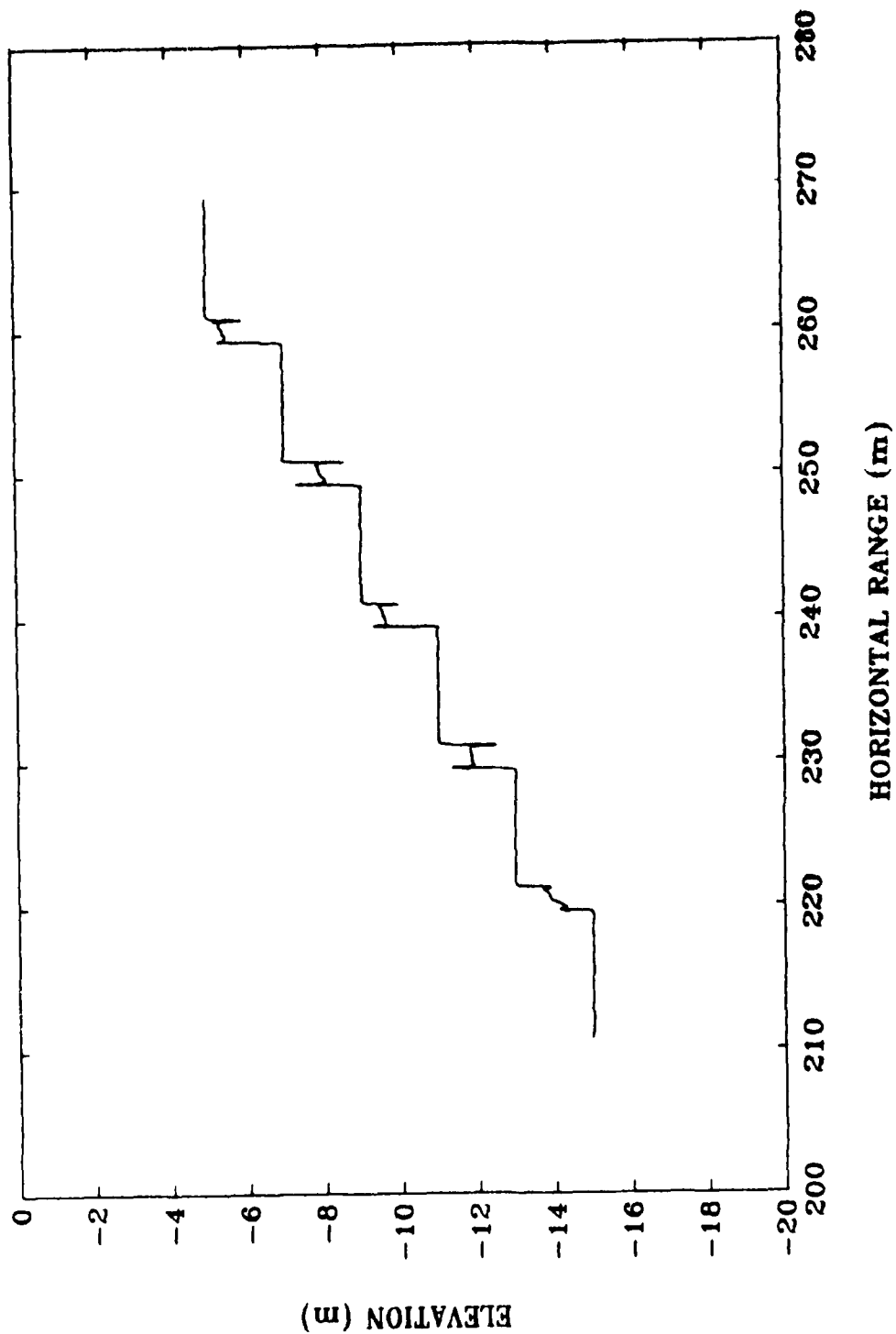**FIGURE 20**
A BRIGHT SPOT OBSERVED ON THE WATER SURFACE
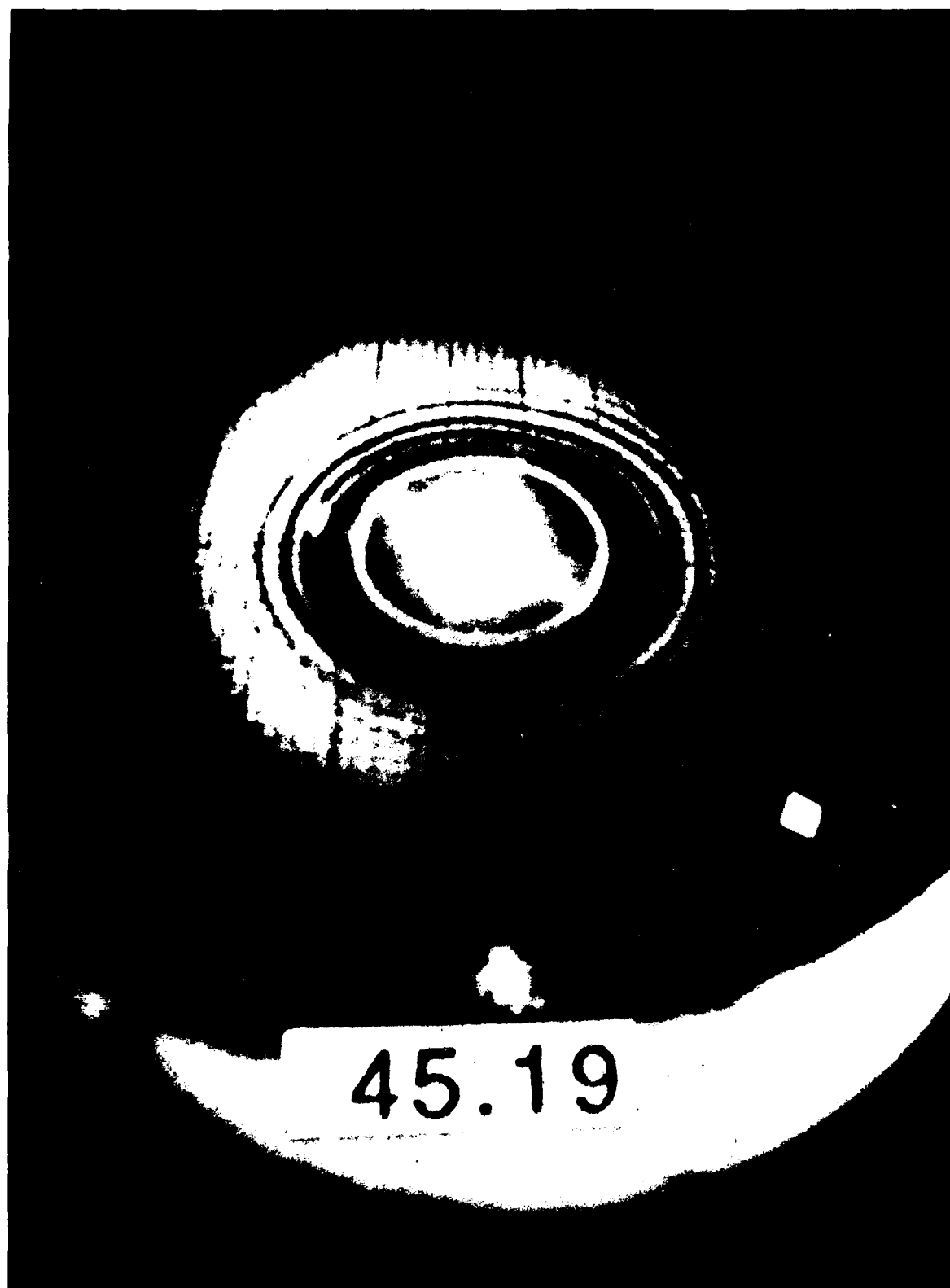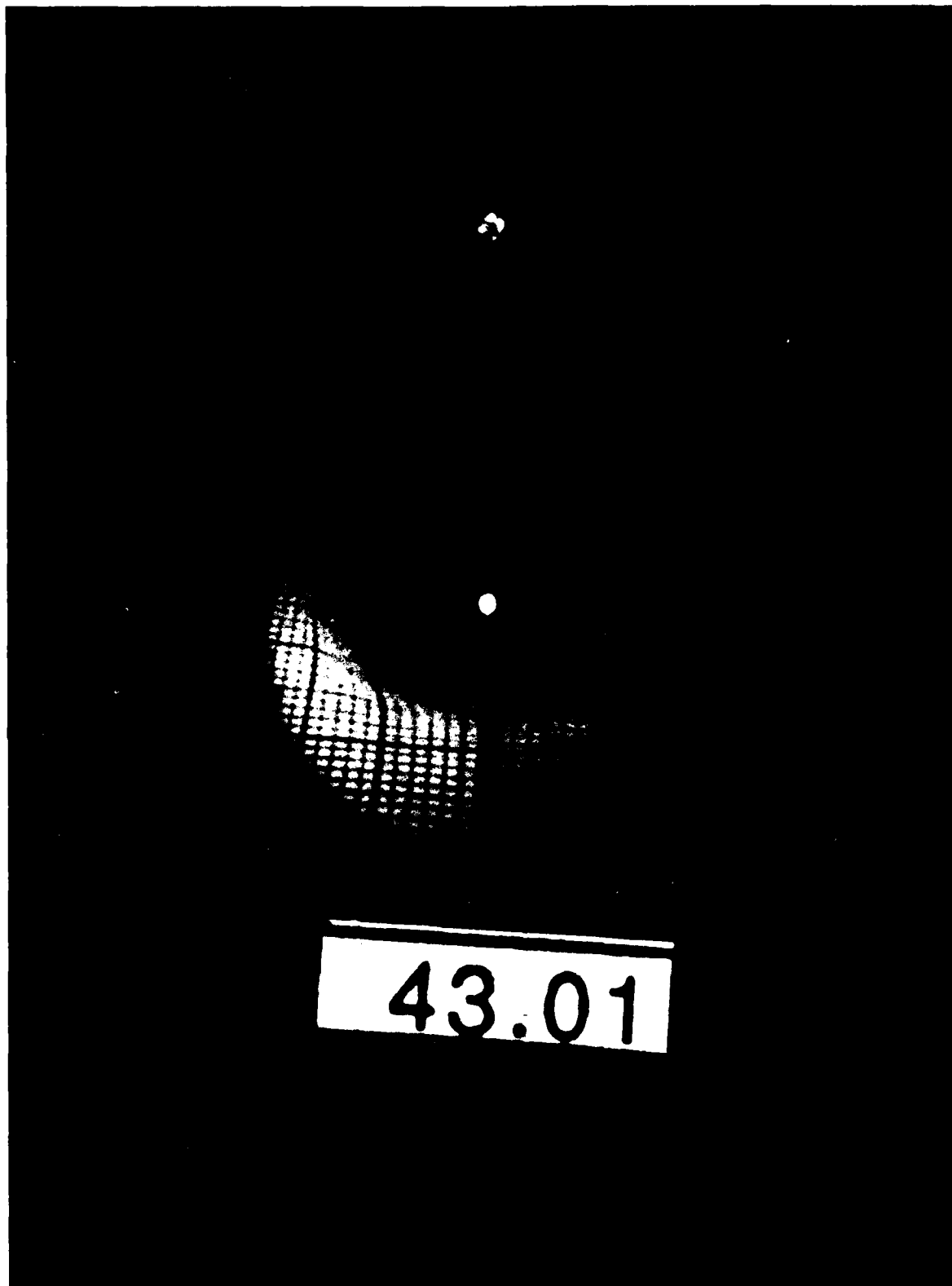
Fig. 11. Underlying effect of postdetection smoothing. Conditions are the same as in Fig. 8 except that noise is removed from both s_0 and s_1.

FIGURE 22
STRONG EMISSION AND CONCENTRIC RIPPLES AT LASER
ENERGY DENSITY 1 MJ/m^2, STROBED AT 10 ms AFTER LASER PULSE

70

5012-11A

FIGURE 23
SURFACE EMISSION, ONE RIPPLE AND ONE PLUME OBSERVED AT
ENERGY DENSITY 14 MJ/m^2, STROBED AT 10 ms AFTER LASER PULSE

4999-22A

applicable to the data at 1 MJ/m². Thus, the impulse function may be approximated by a nonzero constant within a circular area and zero outside it. The photograph of Fig. 22 shows several concentric ripples of roughly equal amplitude which seems to be in agreement with the mathematical results of Kranzer and Keller.

Apparently, this is not the case for the data at 14 MJ/m². In this case, the blast diameter is estimated, from the figures under case 3 in Tables II and III, to have expanded by approximately an order of magnitude by the time $4\tau_u$. Therefore, in this case, the impulse distribution may be expected to be a fairly smooth function of radial distance from the blast center. For functions of this type with continuous first derivatives, Kranzer and Keller showed that only one large ripple will be produced. This appears to be in agreement with the photograph shown in Fig. 23.

The experimentally measured shock peak pressures could not be directly compared with the theoretical blast model predictions. This was because the rise time of the shock probe, at 1.5 µs according to the manufacturer's specifications, was not quick enough for the predicted time constants of the shock pulses, as shown in Table IV. For this reason, the shock pulses shown in Figs. 16-18 are probably not a faithful reproduction of the actual shock pulse; Their time constants, found to be between 1.5 and 2 µs, are determined mostly by the limitations of the probe. To compare these results with the model predictions, it is necessary to allow for the sluggishness of the probe. Assuming that the probe behavior may be modeled as a linear low pass filter, the expected peak pressure would be scaled down by a factor approximately equal to the ratio of the time constants. The experimentally measured peak pressures are compared with the scaled theoretical predictions in Fig. 24. It is seen that at 0.03 MJ/m², the intensity of the laser spot is less than the minimum required for a stable blast; this is supported by the photographic observations which show no visible surface activity. Nevertheless, a significant level of acoustic pressure was produced. The mechanism responsible must be a weak blast, i.e., one that does not satisfy the maximum entropy condition. The results at 1 MJ/m² show good agreement with the equilibrium blast model; photographic observations
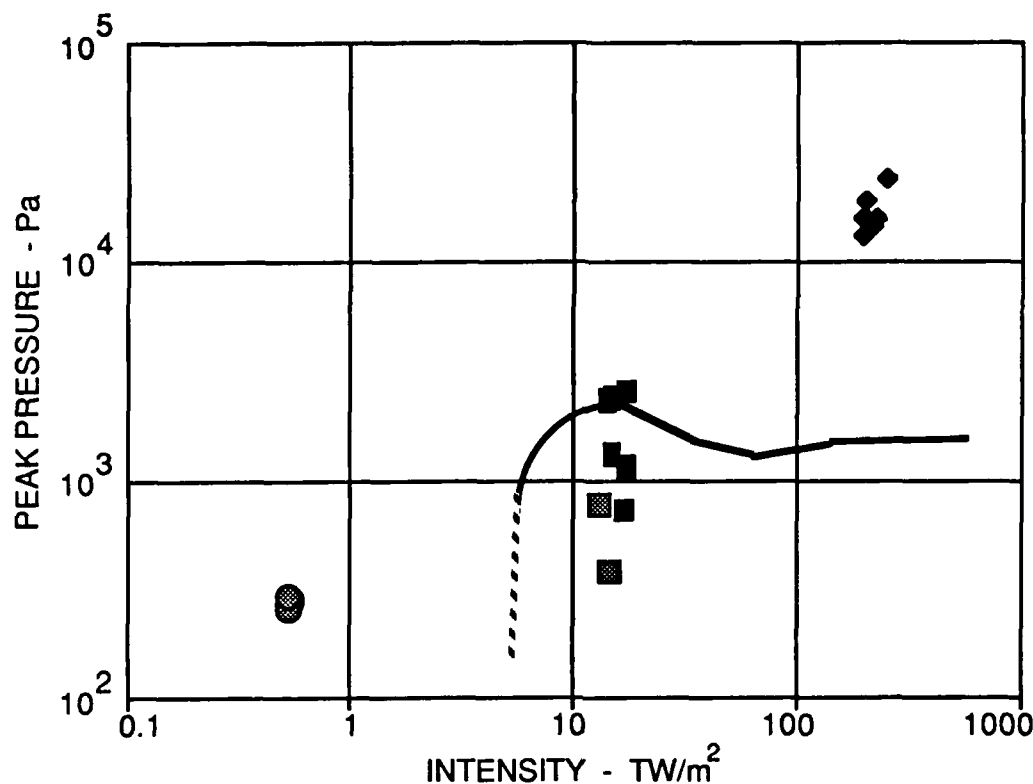
ENERGY DENSITIES, SPOT DIAMETERS, AND
PHOTOGRAPHIC OBSERVATIONS

◆ 14 MJ/m^2, 0.17 mm,
PLASMA COLUMN, SINGLE RIPPLE, PLUME

■ 1 MJ/m^2, 0.66 mm,
PLASMA BALL, CONCENTRIC RIPPLE, NO PLUME

▦ 1 MJ/m^2, 0.66 mm,
SMALL BRIGHT SPOT, NO RIPPLES, NO PLUME

● 0.03 MJ/m^2, 3.2 mm,
NO VISIBLE SURFACE ACTIVITY

── BLAST MODEL AT LASER POWER OF 4.5 MW
ADJUSTED FOR OBSERVED TIME CONSTANT

FIGURE 24
COMPARISON OF OBSERVED PEAK ACOUSTIC PRESSURES
WITH BLAST MODEL PREDICTIONS

clearly show that an explosive reaction has taken place. The acoustic pressures at 14 MJ/m^2, however, are considerably greater than that predicted by the equilibrium blast model. Speculations as to the reason for this excess pressure will be given in a later section.

Comparable experimental data from other sources have not been found. There have been a large number of published reports of optoacoustic generation experiments in the interior of a liquid medium, but very few at the surface. The most extensive data set is that of Maccabee and Bell.[10,11] They used a CO_2 laser, which is considerably different from the Nd:glass laser in terms of laser wavelength. Two subsets of their data are compared with the blast model predictions, one at a laser spot area of 1 cm^2 and the other at a spot area of 6 cm^2, as shown in Figs. 25 and 26. In both cases, it is seen that the laser intensities used in the experiment were too low for an equilibrium blast. The predicted time constants in the equilibrium blast region are approximately 2.5 μs and 4 μs, respectively. The measured time constants were in the region of 1 μs for both cases. It is deduced that the mechanism that produced the acoustic pulses must have been a weak blast, probably due to a number of small equilibrium blasts at a few hot spots within the larger laser spot. This would account for the reduced time constant. This is also consistent with the bright flashes observed at the higher intensity levels.

Comparison of the predicted and measured acoustic energy density spectra were made. For this comparison, there was no need for any compensatory adjustments within the passband of the acoustic receiving system. In Fig. 27, the predicted and measured spectra at 1 MJ/m^2 are shown. It is seen that there is good agreement. Above 100 kHz, the experimental energy density spectrum was mostly contained within the leading positive compression pulse, as assumed by the blast model. Below 100 kHz, the experimental spectrum from the rarefaction phase of the shock pulse was found to be higher by a few decibels. In Fig. 28, a similar comparison is made for the 14 MJ/m^2 case. Again, it is seen that above 100 kHz, the experimental energy density spectrum was mostly contained within the leading positive compression
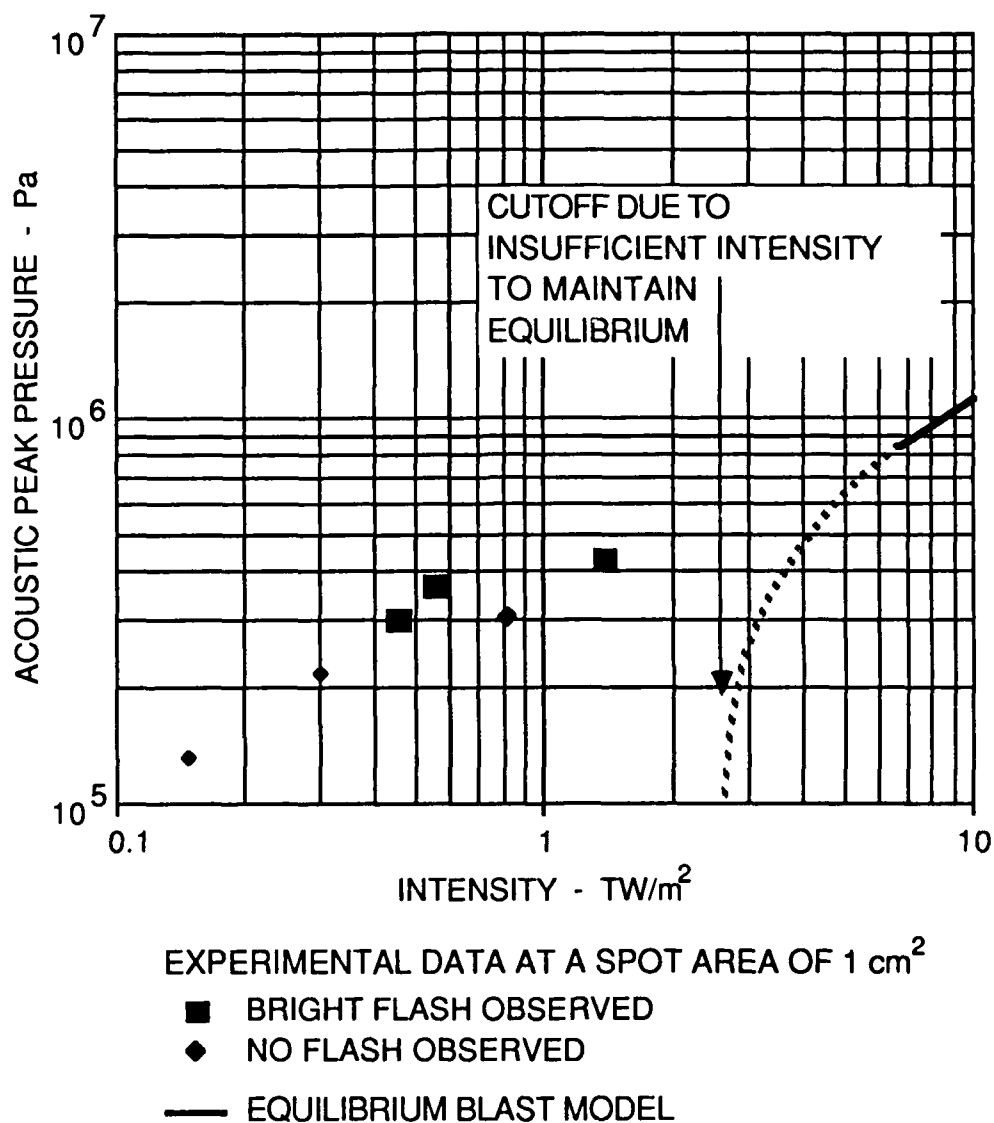
FIGURE 25
EXPERIMENTAL RESULTS OF MACCABEE AND BELL WITH
BLAST MODEL PREDICTIONS AT A SPOT AREA OF 1 cm^2
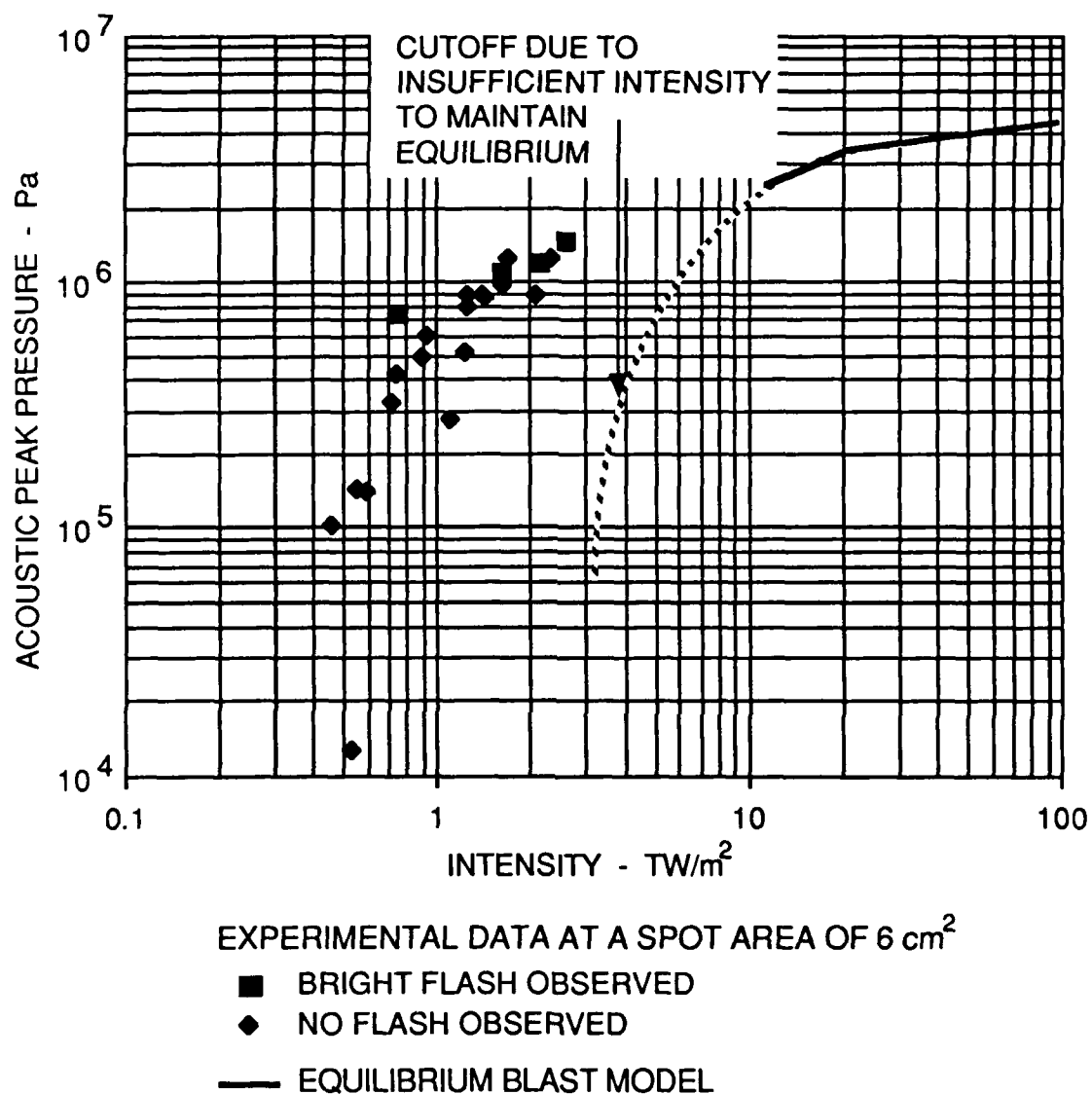
FIGURE 26
EXPERIMENTAL RESULTS OF MACCABEE AND BELL WITH
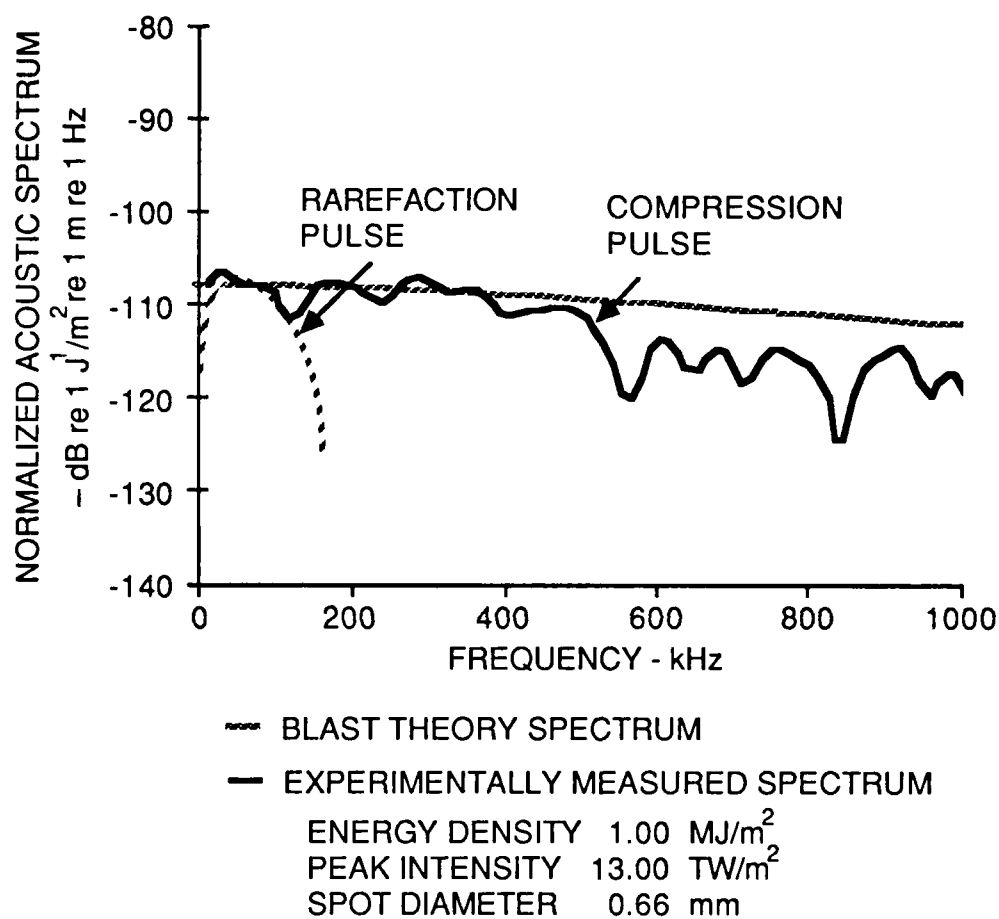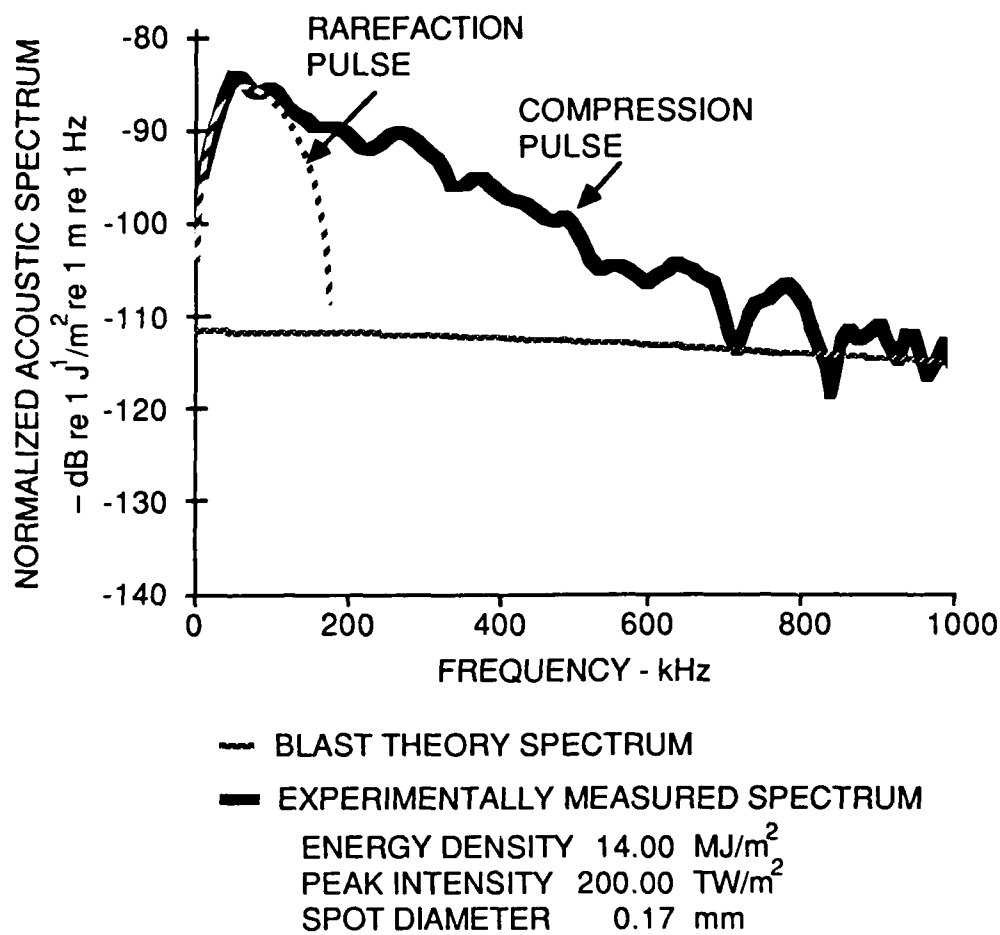BLAST MODEL PREDICTIONS AT A SPOT AREA OF 6 cm²

FIGURE 27
COMPARISON OF THE EXPERIMENTALLY MEASURED ACOUSTIC
SPECTRUM AND THE BLAST MODEL PREDICTION AT 1 MJ/m^2

FIGURE 28
COMPARISON OF THE EXPERIMENTALLY MEASURED ACOUSTIC
SPECTRUM AND BLAST MODEL PREDICTION AT 14 MJ/m^2

pulse. It is also seen that the experimental spectrum level is far higher than the equilibrium blast model prediction.

The experimental acoustic spectra from various observation angles q, where the angle θ is as shown in Fig. 13, are compared in Figs. 29-31. The results for the 0.03 MJ/m^2 case are shown in Fig. 29. The spectra appear to decline at a rate of about 20 dB per decade. This suggests a distributed source function rather like the linear thermoacoustic source. The spectrum in the 0° direction appears to be the strongest except below 150 kHz where the broadside thermoacoustic array generates a significant peak at near-horizontal angles such as at 80°.

In the 1 MJ/m^2 case, as shown in Fig. 30, the spectra are much flatter, falling off at a rate of less than 10 dB per decade, suggesting a more compact source. Within 30° of the downward vertical the spectra appear to be independent of angle. At 85°, there is a peak in the spectrum at around 200 kHz, indicative of a weak broadside thermoacoustic array.

The results for the 14 MJ/m^2 case, as shown in Fig. 31, are most puzzling. The spectra, at 0° and 30°, have returned to a slope of 20 dB per decade, while the spectra at the two highest angles are almost flat. This is indicative of a distributed array once again, but probably an end-fire array rather than a broadside array. Further speculation will be given in a later section.

It was also found that at 1 and 14 MJ/m^2, there was often not just one acoustic pulse but a train of several pulses. As many as four pulses were detected, as shown in Fig. 32. These pulses are thought to be bubble pulses.

D. Optical Results

The mechanism for initiating the blast is, however, not known. For CO_2 lasers, with which many studies of optoacoustic generation have been made, the laser wavelength is 10.6μ. At this wavelength, the absorption coefficient is
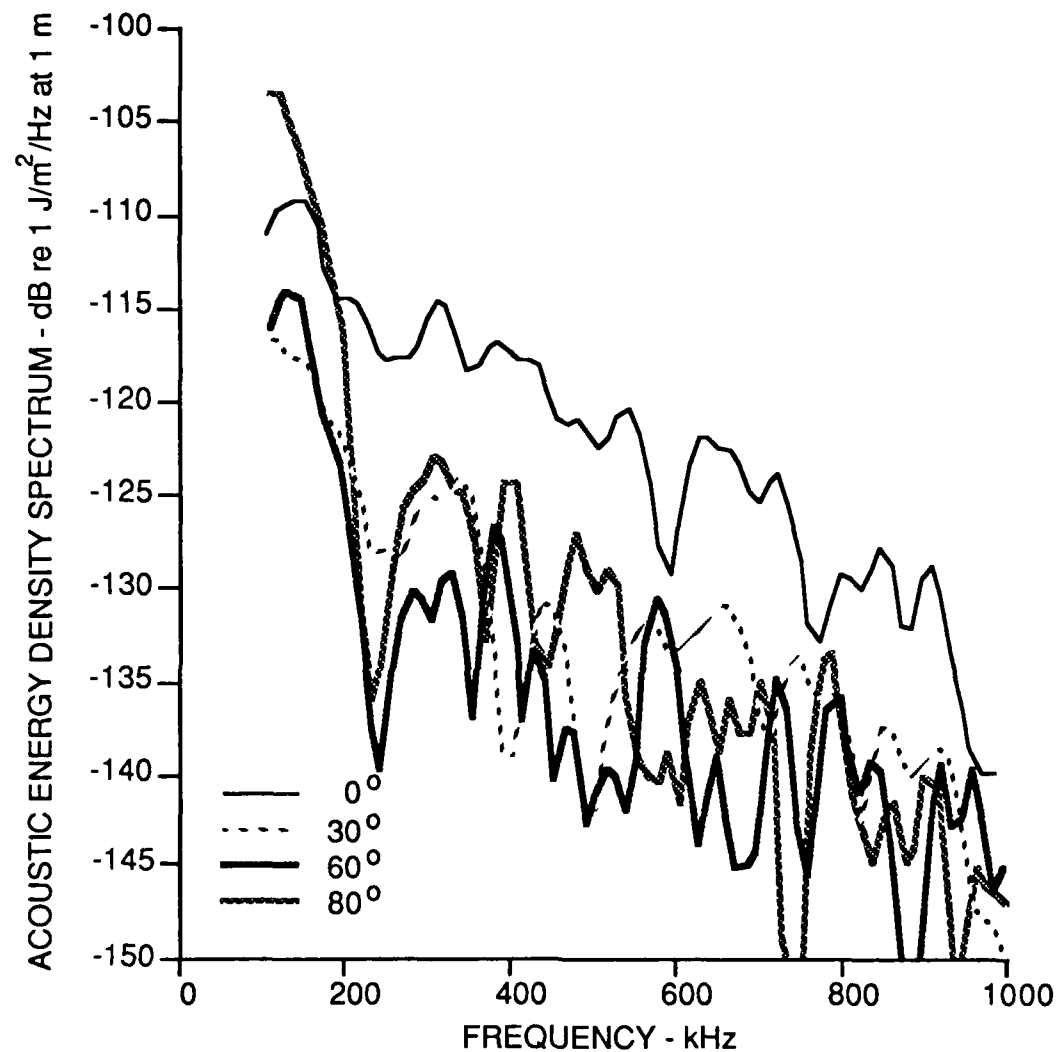
FIGURE 29
MEASURED ACOUSTIC ENERGY SPECTRA AT DIFFERENT
OBSERVATION ANGLES AT 0.03 MJ/m^2
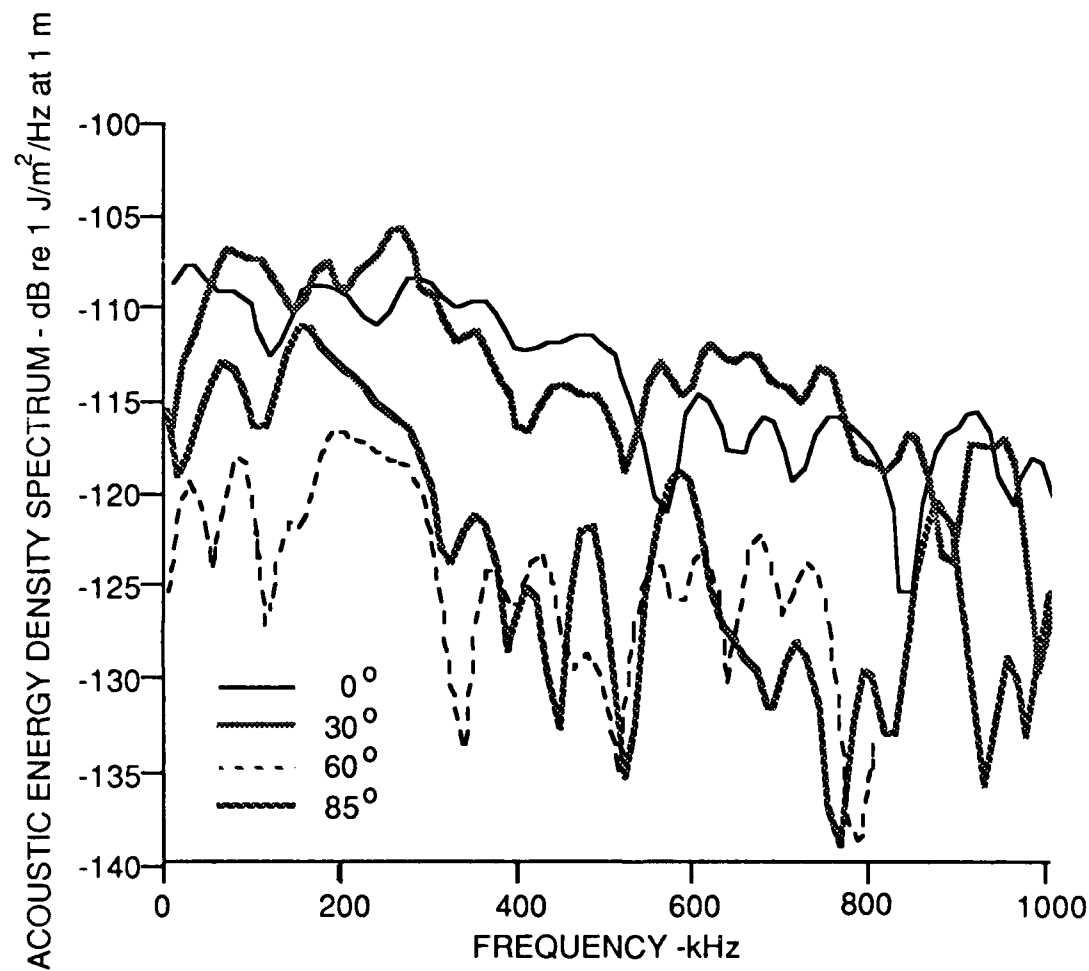
FIGURE 30
MEASURED ACOUSTIC ENERGY SPECTRA AT DIFFERENT OBSERVATION ANGLES AT 1 MJ/m^2

81
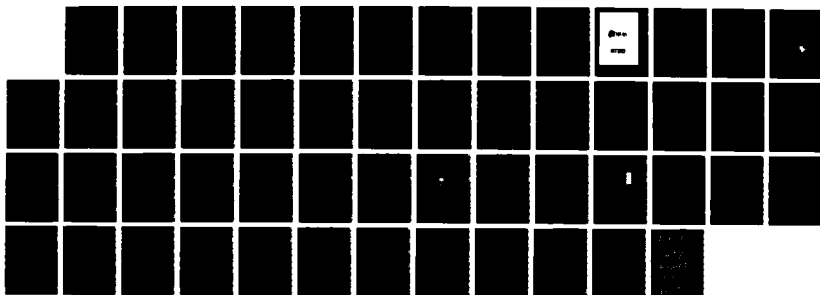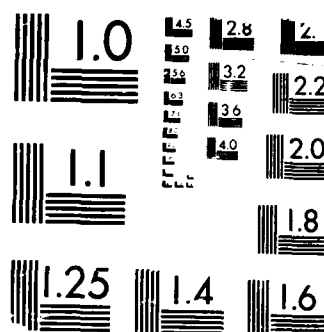
MICROCOPY RESOLUTION TEST CHART
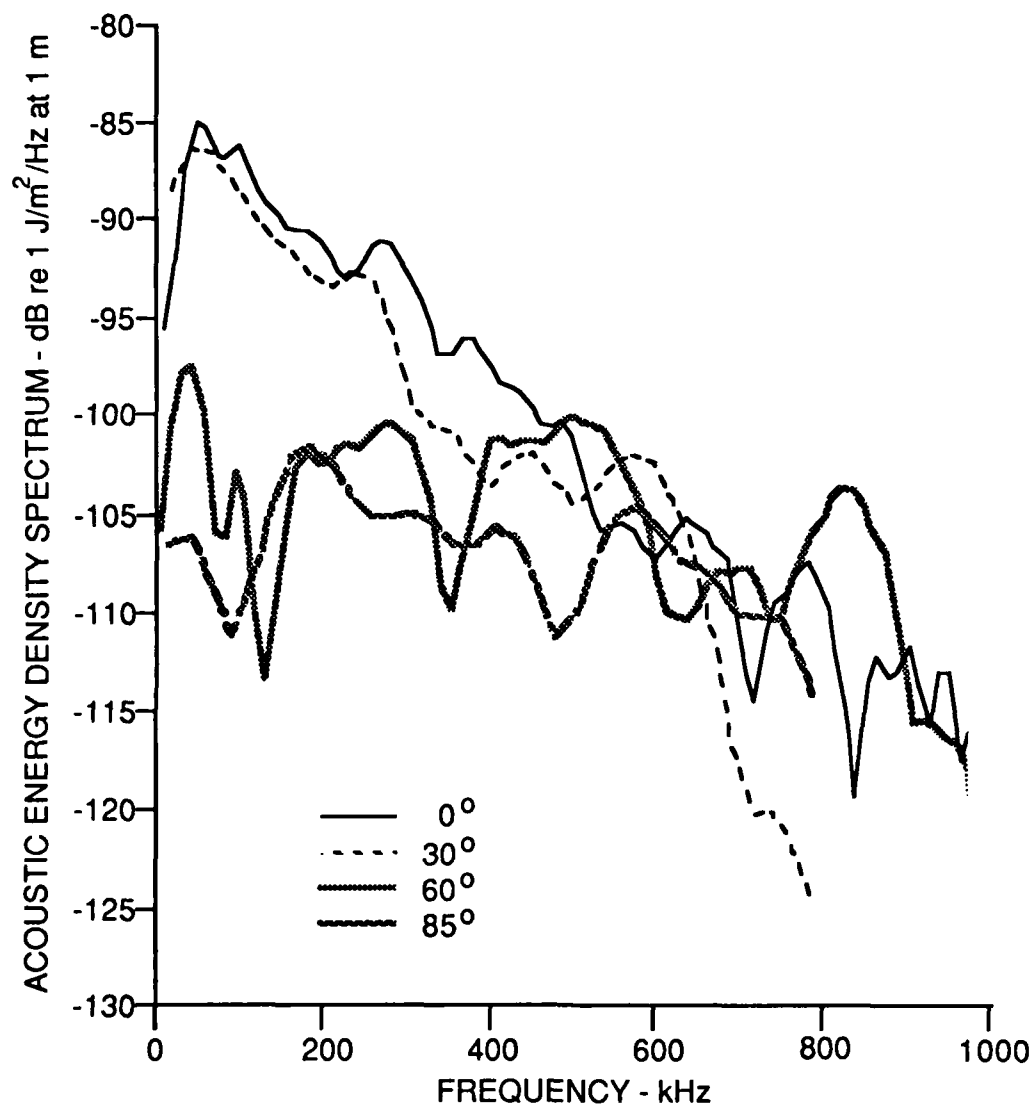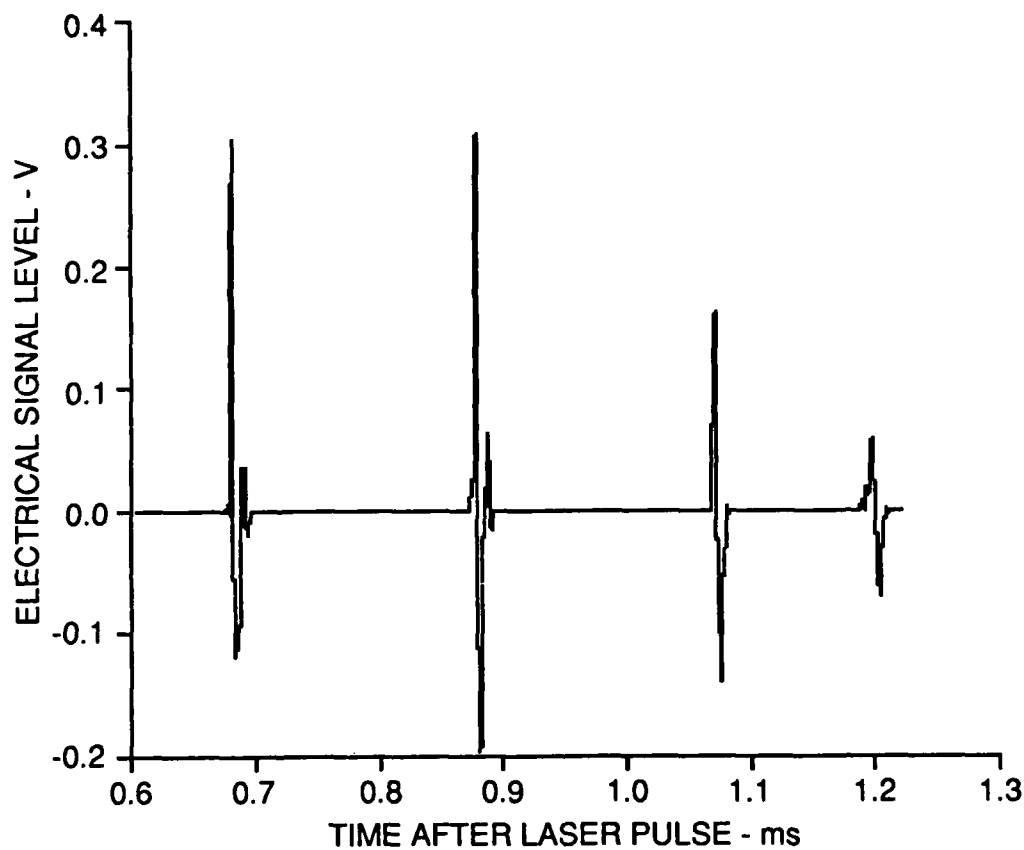
NBUREAU OF STANDARDS 1963-A

FIGURE 31
**MEASURED ACOUSTIC ENERGY SPECTRA AT DIFFERENT**
OBSERVATION ANGLES AT 14 MJ/m²

FIGURE 32
EXAMPLE OF OBSERVED MULTIPLE ACOUSTIC PULSES
**GENERATED BY A SINGLE LASER PULSE AT 14 MJ/m^2**

high enough that simple absorption and the subsequent increase in enthalpy will adequately account for the blast formation. However, for a Nd:glass laser with a wavelength of 1.06μ, at the known absorption coefficient in water of 15 m^{-1}, the laser surface energy density required to cause the water to boil is in excess of 20 MJ/m^2; therefore simple absorption cannot account for the initiation of the blast. It has been postulated[5] that the high intensity of the laser radiation causes the water to undergo a dielectric breakdown which results in a sharp increase in the absorption coefficient. The increase in absorption coefficient then causes the energy density threshold for boiling to be sharply reduced and the remaining laser energy is then absorbed into a thin surface layer which evaporates and starts the blast process.

In an attempt to observe the increase in absorption coefficient, an optical probe was placed in the water at a depth of 0.34 m directly under the blast, as shown in Fig. 13. The laser pulse as monitored by the reference probe through the beam splitter was compared with the observed optical pulse at the underwater probe. In Fig. 33, the observed optical pulses are compared for the case of a peak intensity of 0.1 TW/m^2. The underwater probe was at a depth of 33 cm. Its output was adjusted to compensate for the absorption loss at that depth. It is seen that the two curves are very similar, and so it is deduced that there was little extra attenuation over and above that of the small amplitude absorption. At a higher peak intensity of 0.4 TW/m^2, as shown in Fig. 34, there appears to be significant extra attenuation, and the underwater pulse appears to have lengthened, possibly due to secondary emissions at other wavelengths; the PIN silicon photodiodes are sensitive to a range of wavelengths from about 1μ to 0.4μ, with a peak at 0.8μ. At these levels of intensity, no disturbance was photographically observable at the surface.

Higher intensities were obtained by decreasing the laser spot size. At intensity levels that are associated with the equilibrium blast model and that produced surface disturbances of the type shown in Fig. 22, the secondary emissions were found to be very strong, as shown in Fig. 35. At similar intensity levels, but where the surface disturbance corresponds to that shown in
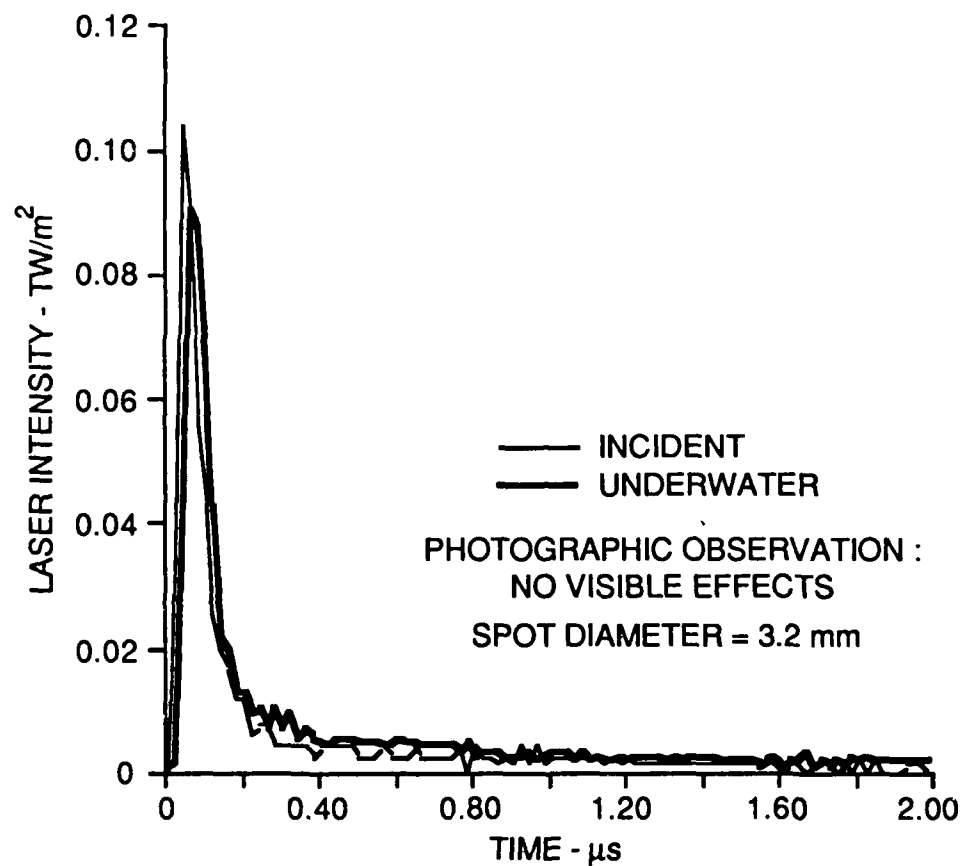
FIGURE 33
COMPARISON OF THE INCIDENT LASER INTENSITY WITH
THE OBSERVED INTENSITY BELOW THE SURFACE AT LOW POWER
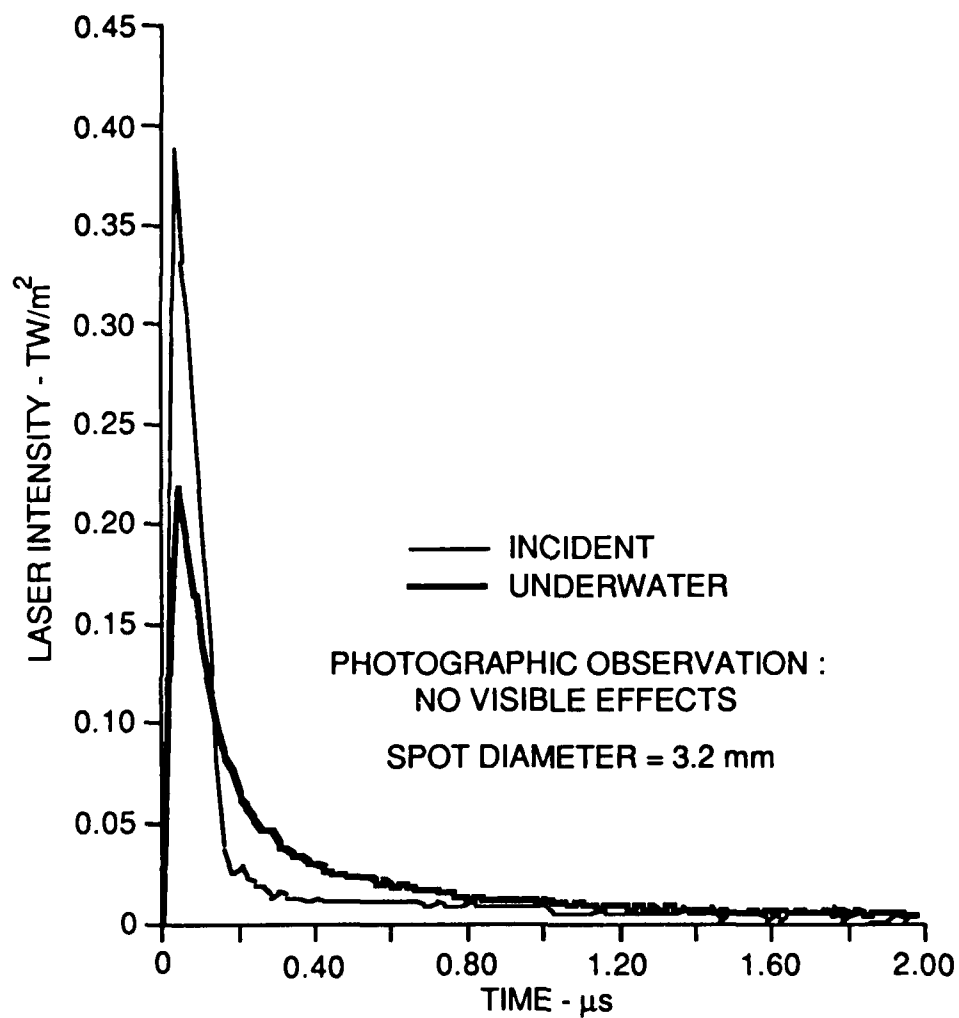
FIGURE 34
**COMPARISON OF THE INCIDENT LASER INTENSITY WITH
THE OBSERVED INTENSITY BELOW THE SURFACE SHOWING
INCREASED ABSORPTION AND SECONDARY EMISSIONS**
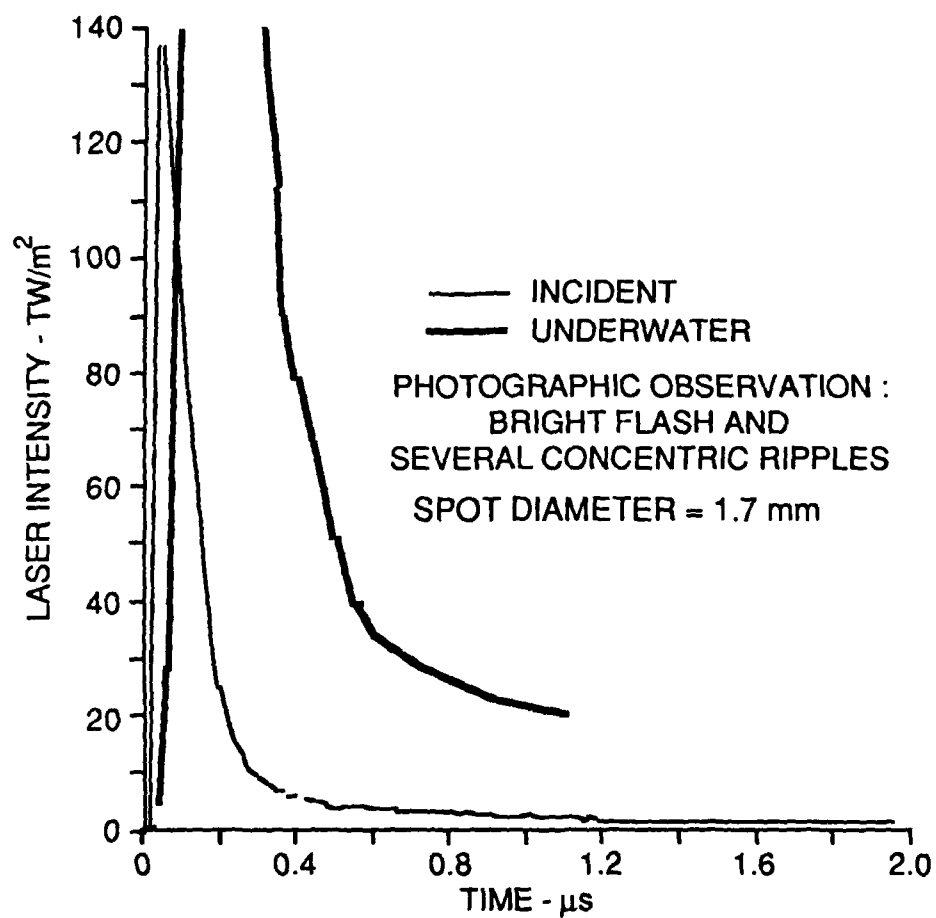
FIGURE 35
COMPARISON OF THE INCIDENT LASER INTENSITY WITH
THE OBSERVED INTENSITY BELOW THE SURFACE SHOWING
**STRONG SECONDARY EMISSIONS**

Fig. 23, there appears to be a significant reduction in the secondary emission, as shown in Fig. 36.

From the above optical results, it is seen that there is a noticeable increase in absorption as the laser intensity is increased. It is also accompanied by secondary emissions. However, it is unlikely that the cause is dielectric breakdown because the absorption appears to increase gradually with increasing laser intensity, starting at 0.4×10^{12} W/m^2. At the highest intensity used, which is 2×10^{14} W/m^2, the electric field is no greater than 2.7×10^8 V/m. From the length[33] of the O-H bond (10^{-10}m) and its energy[33] (2.6 eV), the strength of the H-O bond is estimated to be 2.6×10^{10} V/m. Therefore, dielectric breakdown seems to be an unlikely explanation.

E.   Speculations

The foregoing theoretical analysis has produced a blast model for the laser reaction at the air-water interface which gives plausible results that seem to fit some of the data. Experimental observations of the optical signal have shown that there is some extra absorption of the laser at high intensities, but the breakdown mechanism that must be present to initiate the blast process is still unknown.

It has been observed here and previously by others that sound generation is often accompanied by a strong optical emission from the water. Therefore, it is suspected that a plasma must have formed. A plasma is a collection of charge carriers, and therefore the laser radiation must be causing the water to release charge carriers. It is known that the ionization constant and the conductivity of water increase with temperature, but simple absorption of laser energy and the subsequent increase in temperature cannot account for the charge densities required for plasma formation. With CO_2 lasers at a wavelength of 10.6μ, the plasma appears to form in the ejected vapor. With Nd:glass lasers at 1.06μ, the photographic evidence suggests plasma formation in the liquid. Occasionally, a visible plasma trail descending into the liquid is observed photographically, as shown in Fig. 37.
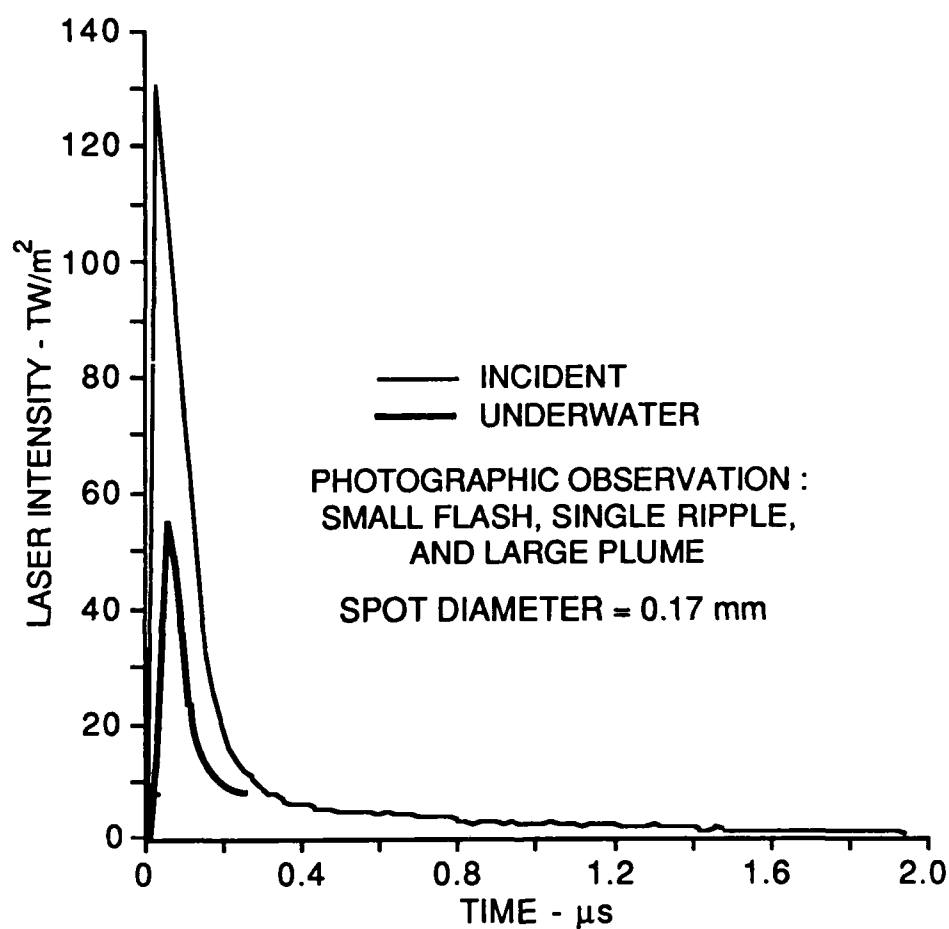
FIGURE 36
COMPARISON OF THE INCIDENT LASER INTENSITY
WITH THE OBSERVED INTENSITY BELOW THE
SURFACE SHOWING HIGH ABSORPTION
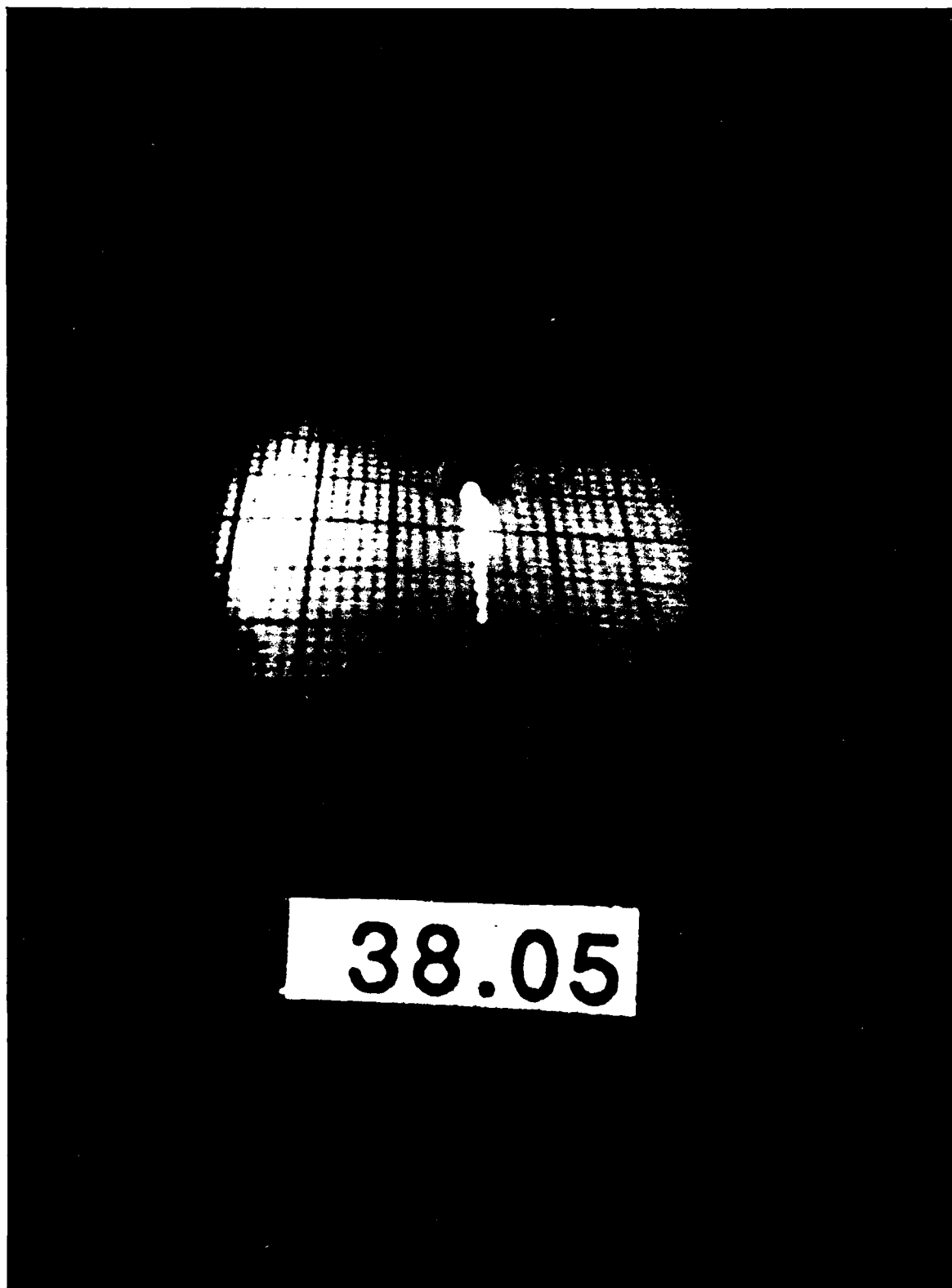
FIGURE 37
A PLASMA TRAIL AND IMPACT CRATER OBSERVED AT ENERGY
DENSITY 14 MJ/m^2, STROBED AT 0.8 ms AFTER LASER PULSE

4999-14A

The energy density of 14 MJ/m^2 was achieved by focusing the laser beam into an area of only 0.023 mm^2. The acoustic output obtained was found to be significantly higher than that predicted by the equilibrium blast model. Although the blast will grow rapidly due to the high intensity, the blast model calculations indicate that it should not be as effective as a blast of equal energy that starts from a larger initial area, as seen in the comparison between cases 2 and 3 in Table IV. This suggests that there is a mechanism that is quite different from the hydrodynamic relationships on which the equilibrium blast model is based. Another significant observation is that this unknown mechanism does not produce as much secondary emission as the equilibrium blast. This suggests that the plasma energy has been diverted away from the emission process. One possible explanation is that the plasma may be coupled to a sound wave in a way that transforms electronic energy into acoustic energy.[34]

The above observations suggests two interconnected speculations. The first is that the high intensity laser beam, perhaps through multiple photon reactions, is capable of generating a plasma in water. The second is that, at sufficiently high plasma densities, the plasma itself may act as an acoustic amplifier, channeling electronic energy into acoustic energy. The shock pulse driving mechanism would be electronic rather than thermodynamic.

IV. LASER-WATER INTERACTION

A. Electron Charge Carrier Generation

To study the mechanism for plasma formation, a simple experiment was conducted to measure the quantity and mobility of the charge carriers that the laser radiation produced, if any. It is speculated that the ionization process is a gradual buildup process, with a growth rate that is dependent on, among other factors, the laser intensity. In order to capture the process in its earliest stages of development, relatively low laser intensities were used. With low intensities, the complication of thermodynamic effects may also be avoided.

The apparatus is shown in Fig. 38. Distilled water was held in a cylindrical test cell. The cell has transparent perspex windows to allow the laser beam to enter and exit. A pair of cylindrical electrodes were inserted into the water to measure its conductivity. A potential of approximately 6 V was applied between the electrodes and the electric current time history was recorded on a Nicolet digital oscilloscope. The laser pulse was also simultaneously recorded. Due to the large electrical capacitance of the electrodes, it was necessary to use a fairly long laser pulse. The laser pulse was produced by spontaneous emission from the Nd:glass rod, without Q-switching. This produced a pulse lasting around 500 μs. The laser intensity, at 40 MW/m^2, was well below the known breakdown thresholds, and no visible reactions were observed. The experiment was repeated over a range of temperatures from 20°C to 80°C. From the time histories of the signals, a number of characteristics may be deduced, including the yield, the mobility, and time constant of the carriers generated by the laser pulse. The results are summarized as follows.

The simplest measurement that could be made was that of conductivity. The conductivity of the water was estimated from the measured dark current, the applied voltage, and the calculated electrostatic field of the electrodes. The conductivity of the water was found to increase with temperature within the range of temperatures considered. The increase in conductivity per unit increase in internal energy is plotted in Fig. 39. It is seen that the thermal
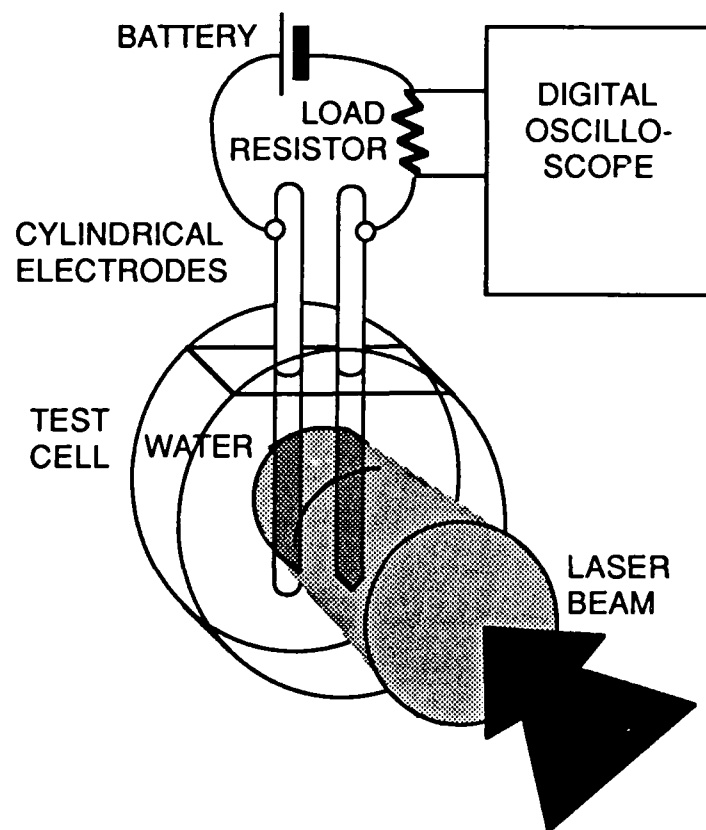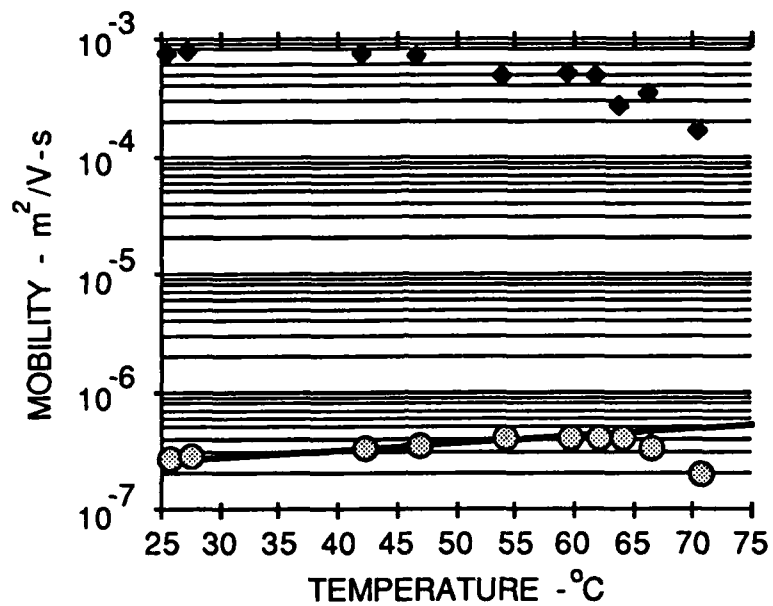
FIGURE 38
APPARATUS TO MEASURE PHOTOCONDUCTIVITY
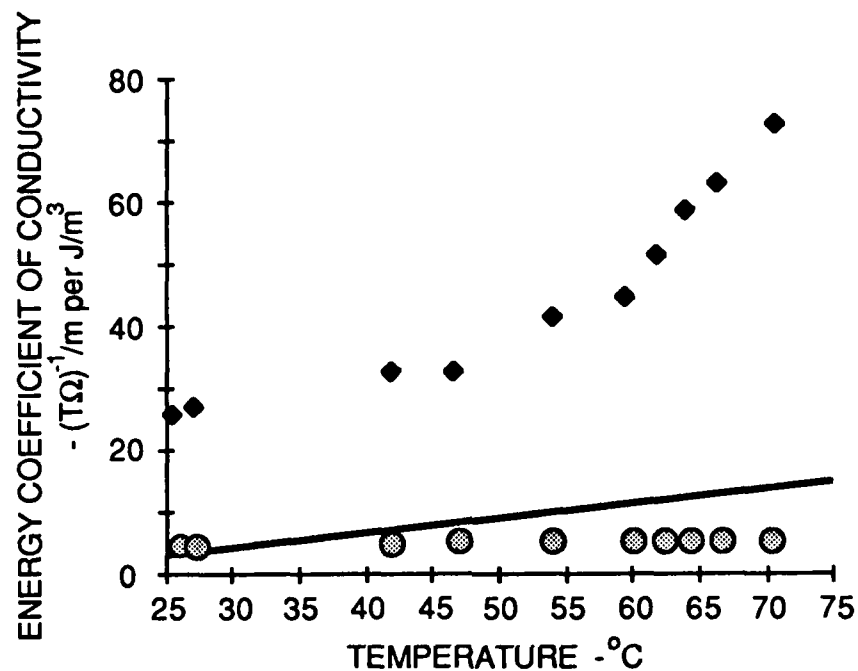
♦ LASER PHOTOCONDUCTIVITY COEFFICIENT
  MEASURED 60 µs AFTER START OF LASER PULSE

◉ MEASURED THERMOCONDUCTIVITY COEFFICIENT

— THERMOCONDUCTIVITY COEFFICIENT FROM
  TABULATED VALUES OF IONIZATION AND MOBILITY

FIGURE 39
MEASURED ENERGY COEFFICIENTS OF CONDUCTIVITY
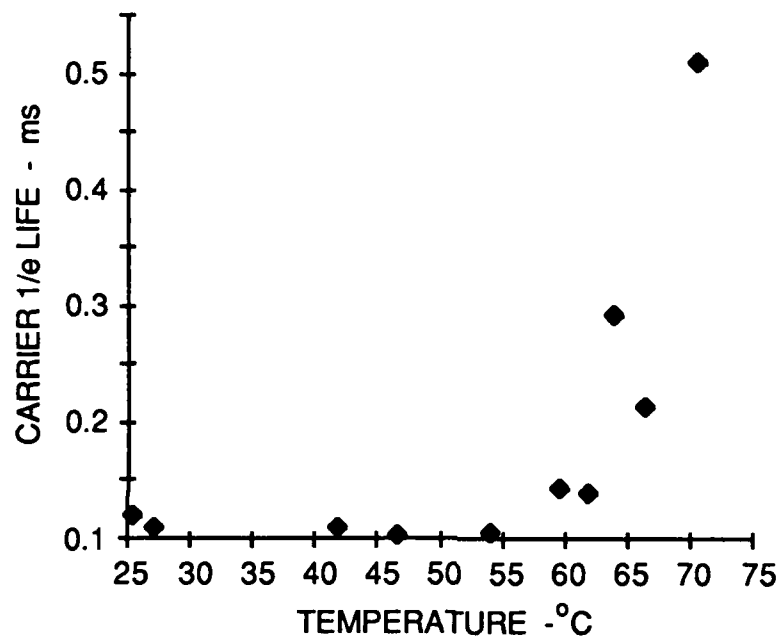AS A FUNCTION OF TEMPERATURE

coefficient of conductivity is approximately constant over the range of temperatures used. The values are comparable to estimates based on the tabulated values of ion densities and mobilities for distilled water.[27] These results were then compared with the increase in conductivity due to absorption of laser energy, measured a short time (60 μs) after the start of the laser pulse. The timing of the measurement was important, because it must be longer than the time constant (<1 μs) of the electrical circuit as determined by the capacitance of the electrodes and the parallel resistance, but shorter than the decay time of the charge carriers produced. The laser energy absorbed per unit mass was estimated from the measured absorption coefficient of the laser in water at the intensities and temperatures used. As shown in Fig. 39, the laser energy produced significantly greater increases in conductivity than simple heating with an equal amount of energy, particularly at the higher temperatures.

Having found that the laser energy produced significantly greater conductivity increases than that expected from simple heating, the data were analyzed further for the properties of the active charge carriers. It is known that the carrier in distilled water is the proton,[35] and the mobility of the proton is well tabulated. From the value and risetime of the dark current, the mobility of the proton carriers was estimated and found to be comparable to the tabulated values, as shown in Fig. 40. The mobility of the charge carriers generated by the laser energy was also estimated and compared with that of the proton in Fig. 40. It is seen that the mobilities of the laser generated carriers are higher, by a factor of about 2000. Since electrons are about 2000 times lighter than a proton, it is guessed that the laser must be exciting valence electrons to a state that allows them to act as charge carriers. They are probably not free electrons as in the case of a metallic conductor but more akin to carriers in a semiconductor that, while loosely bound, are able to hop from one molecule to the next. Their estimated 1/e lifetimes are shown in Fig. 41. It is seen that they only exist for a short time about 100 μs. Finally, the yield in terms of electrons per photon is shown in Fig. 42. It is seen that the yield is fairly constant at low temperatures, but it increases dramatically with temperature above 55°C. The mobility, yield, and lifetimes of the laser generated carriers were calculated from the measured time history of the laser generated conduction current, particularly
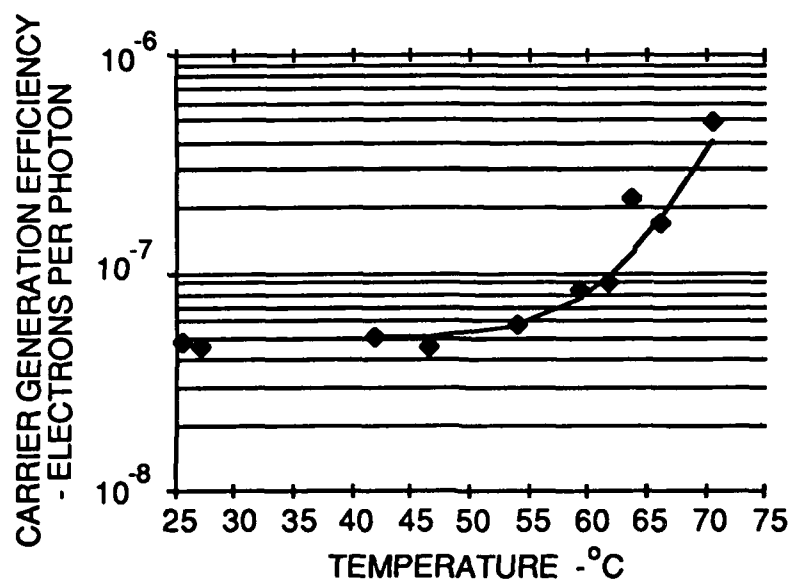
96

FIGURE 40
COMPARISON OF CARRIER MOBILITIES

FIGURE 41
LASER GENERATED CARRIER LIFE
AS A FUNCTION OF TEMPERATURE

FIGURE 42
LASER CARRIER YIELD AS A FUNCTION OF TEMPERATURE

the initial rate of current increase, and the conduction currents at 60 and 300 μs. They are related through a set of nonlinear simultaneous equations. The solutions were obtained iteratively.

B.   Plasma Generation

From the experimental results, it appears that the laser photon, at a wavelength of 1.06μ, is able to liberate electrons. At this wavelength, it cannot directly dislodge an electron, and therefore it must be energizing the electrons through a vibration mode of the water molecule. The excitation must be such that electrons are energized to a degree that they can significantly behave as charge carriers. Therefore, it is speculated that a plasma can be formed. The yields within the measured range of values, however, are not sufficient to produce a plasma of a sufficiently high density. The level of plasma density that is considered to be sufficient will be defined in the next section.

Given that the photon energy is efficiently channeled into the production of electron charge carriers, the law of conservation of energy dictates that the upperbound of the electron yield must be governed by the electron energy increase divided by the available photon energy. If it is assumed that the electrons are not entirely free, but sufficiently energized that they can hop from one molecule to the next, then it is speculated that the band gap energy E_b is the difference between the electron affinities of the H and OH ions. From the electron affinity tables,[27] the values are 0.80 and 1.83 eV. Therefore, the value of E_b is estimated to be 1.03 eV, as shown in Table V. At 1.06μ, the photon energy is 1.17 eV. Therefore, the upperbound of the electron yield is estimated by dividing E_b into the photon energy, giving 1.14 electrons per photon. If it is assumed that the observed yield trend shown in Fig. 42 may be extrapolated to higher temperatures until the upperbound is reached, as shown in Fig. 43, then a sufficiently high yield would be achievable.

Even at a laser energy density of 14 MJ/m^2, calculations based on the small amplitude absorption coefficient indicate that the heat energy absorbed would only raise the temperature of the water by approximately 10°C from room

100

TABLE V

EQUILIBRIUM BLAST MODEL CASE STUDIES: DETONATION

PLASMA SOUND SOURCE PARAMETERS

Laser frequency	Hz	2.83E14
Electron affinity of the OH -ion	eV	1.83
Electron affinity of the H -ion	eV	0.80
Difference	eV	1.03
Photon energy at 1.06μ	eV	1.170
Upperbound electron yield per photon		1.136
Critical density	m-3	9.9E26
Energy density threshold	MJ/m^2	11

CASE STUDIES		1	2	3
Spot diameter	m	0.0032	0.00066	0.00017
Spot area	m^2	8.0E-6	3.4E-7	2.3E-8
Incident intensity	W/m^2	5.6E+11	1.3E+13	2.0E+14
Energy density	MJ/m^2	0.03	1.0	14

PLASMA SOUND SOURCE CALCULATIONS

UNIFORM INTENSITY MODEL

		1	2	3
Time to produce plasma cutoff (t_{oa})	μs	19.1	0.812	0.054
Time for complete ionization (t_{ob})	ps	197	8.4	0.55

RANDOM INTENSITY MODEL

		1	2	3
Probability of avalanche ionization	%	0	100	100
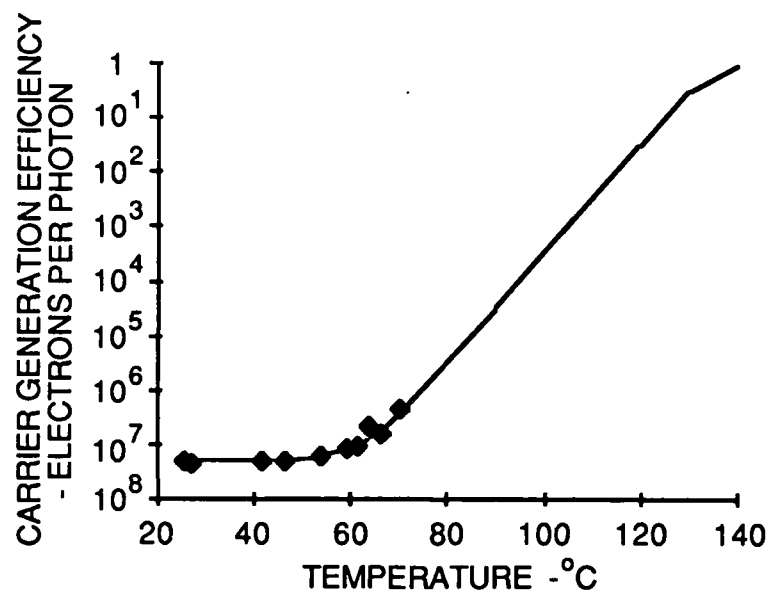
FIGURE 43
EXTRAPOLATION OF CARRIER YIELD TREND

temperature, which is negligible compared to the temperatures necessary to produce a sufficiently high yield. From the above experimental results, it may be deduced that the laser photons, at a wavelength of 1.06µ, can selectively excite certain modes of molecular vibration that produce conduction electrons. Let us refer to these modes as "conduction modes". If a temperature can be ascribed to the degree of excitation of these conduction modes, then it follows that the laser photons can selectively raise their temperature. The ratio between the temperature rise in the conduction modes and the overall temperature rise may be considered as a "temperature gain factor". Thus, it is postulated that, while the laser energy density can only raise the overall temperature of the water by a few degrees, it may raise the temperature of the conduction modes by the equivalent of several tens or hundreds of degrees. This temperature gain is expected to be only momentary; its duration is expected to be roughly equal to the lifetime of the carriers generated.

C. Avalanche Ionization

In order to obtain an explosive reaction, we also need a process by which a plasma can concentrate the laser energy into a small volume to generate an intense blast. From plasma theory, it is known that plasmas have an e-m wave cutoff frequency ω_p, called the plasma frequency,[29,36] given by

$$\omega_p = (Ne^2/\varepsilon_o m_e)^{1/2} \ , \tag{80}$$

where

> N is the volumetric carrier density,
> e is the carrier charge,
> ε_o is the permittivity of the medium, and
> m_e is the carrier mass, assumed to be an electron.

All e-m waves of frequencies lower than the plasma frequency cannot propagate through the plasma, and are rapidly absorbed. The critical density N_o of an electron plasma at a wavelength of 1.06µ is estimated to be

9.9×10^{26} electrons/m^3. When this critical plasma density is achieved, it will cause the laser absorption to abruptly increase. Subsequent laser energy arrivals will be concentrated in a thin surface layer causing local superheating, and hence producing the gas to drive a blast. The plasma will also radiate over a broad spectrum which is consistent with the experimental observations. The time t_{oa} required to achieve the plasma cutoff is given by

$$t_{oa} = \omega_\lambda^2 \varepsilon_o m_e\, e^{-2} E_p / (Y \alpha_{oa} I_o) \quad , \tag{81}$$

where

ω_λ is the laser frequency,

Y is the electron yield per photon,

I_o is the laser intensity,

E_p is the laser photon energy, and

α_{oa} is the laser absorption coefficient before plasma cutoff, assumed to be equal to the low intensity absorption coefficient. At a wavelength of 1.06μ, α_{oa} is equal to 15m^{-1}.

Using the upperbound electron yield of 1.14 electrons per photon, the time required to achieve the plasma cutoff for the three numerical case studies is given in Table V. After plasma cutoff is achieved, further laser energy arrivals will be concentrated in an increasingly thin layer of the medium. The absorption coefficient α_{ob} is now given in terms of the laser frequency ω_λ by[29]

$$\alpha_{ob} = \omega_\lambda \left[\mu_o \varepsilon_o \left((\omega_p / \omega_\lambda)^2 - 1 \right) \right]^{1/2} \quad . \tag{82}$$

The rate of increase of carrier density dN/dt is related to the absorption coefficient by

$$dN/dt = Y \alpha_{ob} I_o / E_p \quad . \tag{83}$$

Substituting for ω_p from Eq. (80) into (82) and for α_{ob} from (82) into (83), and then integrating, an expression for the plasma density N and elapsed time t is obtained,

$$t = E_p (2Y\omega_\lambda I_o)^{-1} (N_o(N - N_o)/\mu_o\varepsilon_o)^{1/2} . \tag{84}$$

Setting N equal to the number of available conduction electrons N_{ce}, the additional time t_{ob} required to achieve total ionization may be estimated. Assuming two electrons per H_2O molecule, the available density is calculated to be 3.35×10^{28}. As shown in Table V, once plasma cutoff has been achieved, it is only a matter of picoseconds before complete ionization is achieved. This process is called avalanche ionization.

In the ionization avalanche, a point is reached where the energized electrons outnumber the ground state electrons. The population inversion will cause the plasma to emit e-m energy. Assuming a simple two-level energy state system, the volumetric source density Q of the e-m radiation is given by[37]

$$Q = (2N - N_{ce})E_b/t_e , \tag{85}$$

where t_e is the 1/e life of the electrons in the higher energy state.

Multiplying both sides of Eq. (79) by I_o, we obtain $I_o t_{oa}$ on the left which is laser energy density or fluence, and the terms on the right hand side are all constants. Thus, the above theory of avalanche ionization predicts a definite avalanche threshold in terms of the laser energy density. Assuming the upperbound yield, the threshold is computed to be 11 MJ/m^2. At this point, it is useful to make comparisons with published theories and experimental results.

It has been suspected by a number of researchers that free electrons play a crucial role in the initiation of the avalanche process. Bass and coworkers,[38-40] in studying the breakdown in crystals, concluded that the process is a probabilistic one which relies on the existence of one or more "lucky" electrons that are able to resonate at the frequency of the laser e-m waves, and thus act as a tuned antenna to concentrate laser energy into a small volume. The energy concentration then spills over to neighboring electrons causing them to also resonate. Thus the excitation spreads as an avalanche.

There are several published measurements of the optical breakdown of water,[41-45] much of it in the field of ophthalmic laser surgery. In most studies, it was assumed that the breakdown threshold is one of intensity or electric field strength. In each case, the experiments were done with a laser pulse of a fixed duration, and therefore it was impossible to separate intensity (irradiance) dependence from energy density (fluence) dependence. The most recent and thorough study is probably that of Docchio et al.[45] using an extremely short laser pulse of 7 ns and a range of spot sizes; the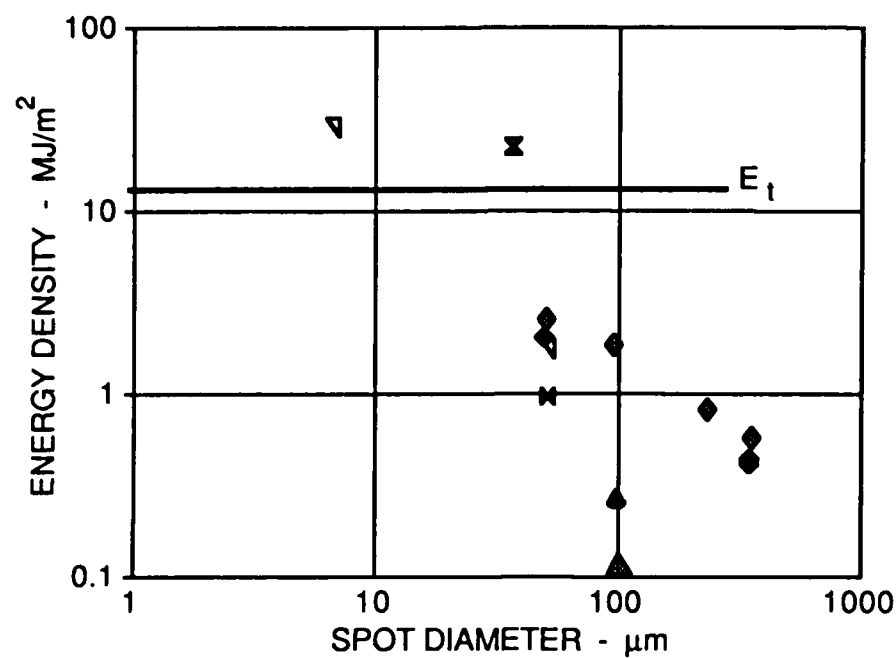 spot size is the diameter of the narrowest part of the focused laser beam. The experiments were carried out at the Center for Fast Kinetics Research, The University of Texas at Austin. In the absence of any definite theoretical model, they took the precaution of presenting their results in all possible forms (intensity, field strength, energy density, etc.). They found that the thresholds, in all the forms used, were not constant but dependent on the spot diameter. The observed intensity thresholds from several sources are plotted as a function of spot diameter as shown in Fig. 44. The estimated dielectric strength of the O-H bond is estimated to be 2.6×10^{10} V/m, which is equivalent to an intensity of $1.3 \times 10^6 TW/m^2$. It is also noted that the *minimum spot diameter is approximately equal to the wavelength of* 1.06μ. It is tempting to speculate that the data points indicate a trend line or curve that terminates at the point of intersection of the smallest spot diameter and the molecular dielectric strength. However, the trend lines in the subgroups are not consistent with this view. The spread of data points is also too large to allow a regression fit of any significant confidence level.

Plotting the breakdown thresholds in terms of energy density appears to be a small improvement in that the spread is now reduced from three decades to two, as shown in Fig. 45. The theoretical energy density threshold is given by the product of the laser intensity and the time it takes to achieve plasma cutoff, $I_o t_{oa}$, which was computed above to be 11 MJ/m^2. The theoretical threshold is shown in Fig. 45 for comparison. Examining the experimental data, it can be seen that the results for distilled water and saline solutions are almost indistinguishable. The data for tap water is seen to be very variable, probably due to the wide variation in the quality of tap water and particularly the presence of dissolved gases; therefore the tap water data are best ignored.

FIGURE 44
BREAKDOWN INTENSITY THRESHOLDS
AS A FUNCTION OF SPOT SIZE
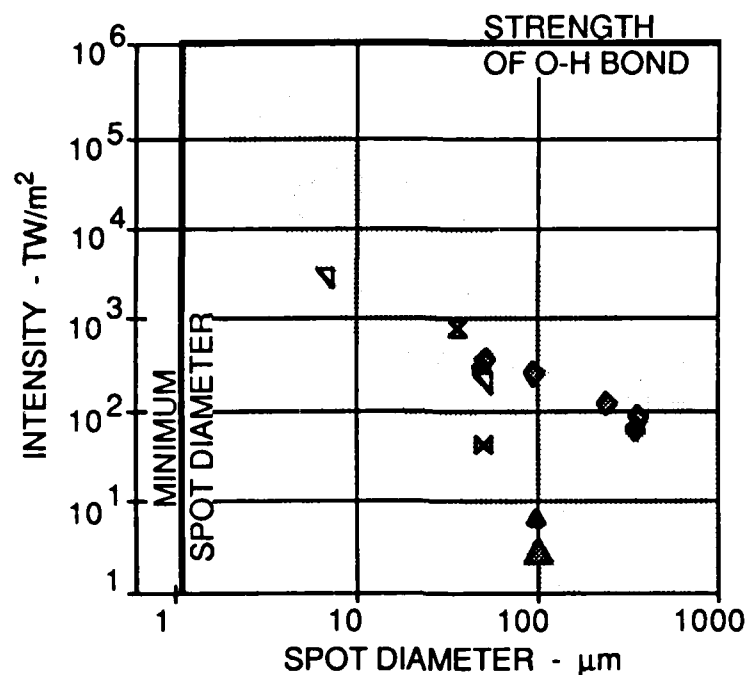
MEDIUM	BREAKDOWN PROBABILITY	SOURCE
TAP WATER	⋈ 50%	Mainster
	◁ >90%	Lörtscher
	⋈ 50%	Pozhidaev
0.9% SALINE SOLUTION	◈ 50%	Docchio
	◆ >90%	Docchio
	▲ 50%	Schmidt-Kloiber
DISTILLED WATER	▲ 50%	Schmidt-Kloiber
	◆ 50%	Docchio

FIGURE 45
ENERGY DENSITY BREAKDOWN THRESHOLDS
AS A FUNCTION OF SPOT SIZE

In order to unravel the apparent disorder in the data for distilled water and saline solutions, let us speculate on the possible explanations for the spot size dependence. The theoretical calculations are based on the assumption of a uniform laser beam profile. This is clearly not the case in practice. Multimode laser beams have a more or less random beam profile, and therefore the energy intensity at any point in a laser beam is a random variable. Focusing the beam increases the mean energy density within a reduced area but the random nature remains. Therefore, the problem may be treated as a probabilistic one.

A laser beam cross-section may be divided into a number of statistically independent resolvable areas. Let n represent the number of independent areas. The random variation is assumed to be the result of the superposition of several modes. Therefore, for large n, the probability density function of the energy density at any point may be approximated by an exponential density function. For a mean energy density E_o, the probability $p(E_o, n)$ that at least one resolvable area has an energy density greater than the threshold E_t is given by

$$p(E_o, n) = 1 - (1 - \exp(-E_t/E_o))^n .$$
(86)

The value of E_t is 11 MJ/m^2 as calculated above. The size of the minimum resolvable region is determined by the laser wavelength. Therefore, at any given spot diameter d_o, the upper bound of n is approximately given by

$$n \leq (2d_o/\lambda)^2 .$$
(87)

The actual value of n is not easily estimated since it must depend on a number of equipment specific factors, such as aperture size, the number of modes, and the lens configuration. The data collected in Fig. 45 suggest that there is a dependence on the spot diameter d_o, but this dependence is probably different for each data set. Let us take the most complete data set, that of Docchio, and see if a plausible relationship between n and d_o can be found that is consistent with the above inequality. Let us assume that n may be approximately related to d_o by a power law,

$$n \approx (d_o/d_1)^m (2d_o/\lambda)^2 \quad ; \quad m > 0 \quad \text{and} \quad d_1 > d_o \ , \tag{88}$$

where m and d_1 are constants to be determined. To be consistent with the above inequality, it is required that d_1 be greater than d_o for positive values of m. Substituting for n from Eq. (88) into (86), an expression for $p(E_o,n)$ is obtained in terms of E_o and d_o, and m and d_1.

An attempt was made to fit this model to the results of Docchio. The results, as shown in Fig. 46, show the energy density thresholds at 0%, 50%, and 100% as measured by Docchio with distilled water and saline solution; the 0% and 100% thresholds are theoretically impossible to measure, and therefore they are interpreted as <10% and >90%, respectively. A reasonably good fit was obtained with m=2, d_1=0.6 mm if, in addition, the energy density E_o is assumed to have a small offset of -0.6 MJ/m^2. The offset may be due to low intensity leakage of laser energy before and after the Q-switched pulse, a well known problem with the Q-switched laser. The 10%, 50%, and 90% thresholds obtained from Eq. (86) at the stated parameter values are compared with the measured values. It is seen that the 50% theoretical curve could be fit quite well to the corresponding measured data points, while the data points at >90% and <10% fall above and below the 90% and 10% curves, respectively. Therefore, it is seen that the theoretical model can be fitted to Docchio's data quite well.

Let us now apply these results to our three numerical case studies, as shown in Table V. Using Eqs. (86) and (88) and the above values for the constants m and d_1, the probabilities of avalanche ionization for the numerical case studies were computed. The results were found to be 0%, 100%, and 100%, to at least the seventh decimal place, for cases 1, 2, and 3, respectively. These results are consistent with the experimental observations, since breakdown was always obtained at energy densities similar to those of cases 2 and 3, but never in case 1.
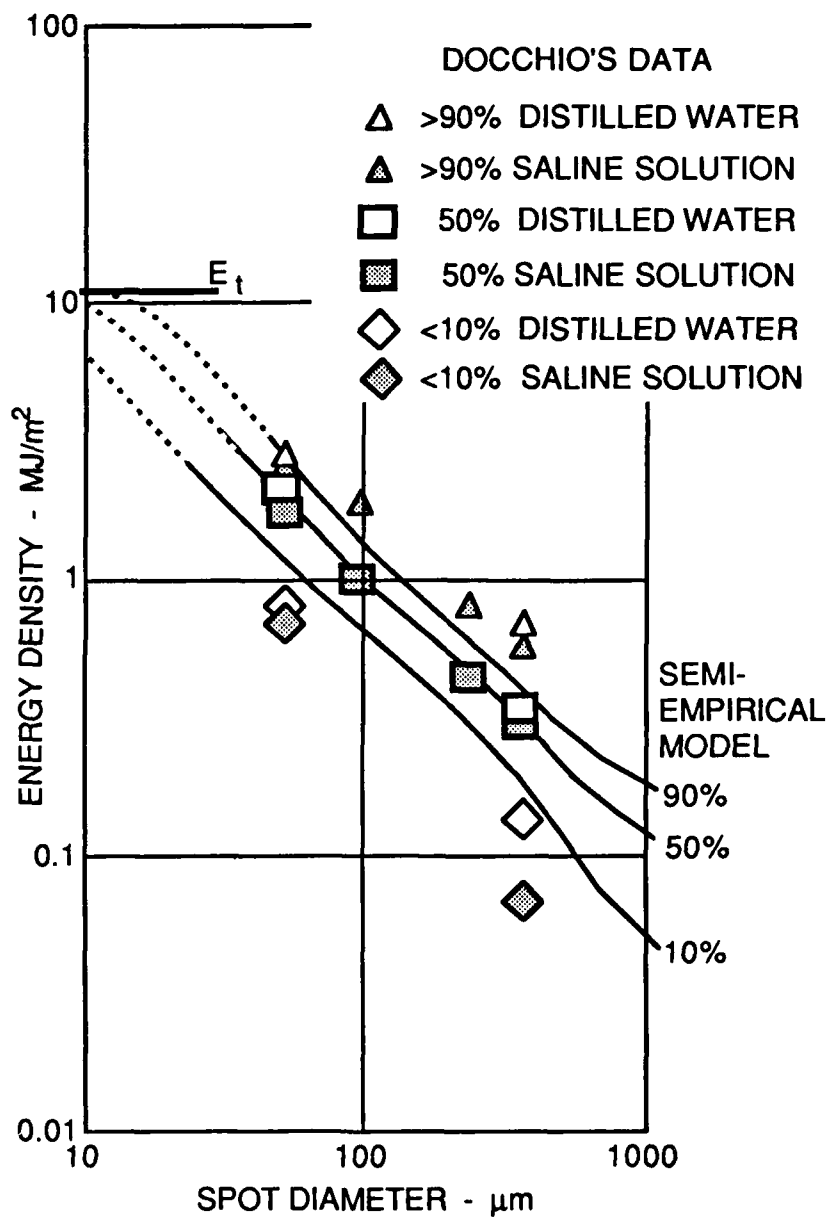
FIGURE 46
MODEL OF ENERGY DENSITY THRESHOLDS
BASED ON DOCCHIO'S DATA

111

D. Plasma Triggered Blast

In the light of the above model, it appears that avalanche ionization may be achieved in small localized areas even when the mean laser energy density is less than the threshold value of 11 MJ/m^2. These "hot" areas will form the nuclei from which ionization may spread. Once the cutoff plasma density is achieved in one small area, it would only take a few picoseconds for the available electrons in that region to achieve a population inversion and radiate energy. Thus, the plasma will redirect the absorbed laser energy to the surrounding molecules. The increased radiation will then energize the electrons in the surrounding molecules. Thus, the cutoff plasma will grow outwards from the nucleation sites and spread over the laser illuminated water surface. This will cause a big increase in the laser absorption. Subsequent laser energy arrivals will be absorbed and concentrated in a very thin surface layer causing it to expand explosively. This forms the one-dimensional stage of the equilibrium blast model. Subsequent reactions can be expected to follow the blast model developed in the preceding sections.

This model provides a more plausible mechanism for triggering the blast process than dielectric breakdown of the water molecule. It also appears to fit the observations. As shown in the photograph of Fig. 22, and in the corresponding recorded optical emission signal in Fig. 35, there is evidence of strong optical emissions indicative of plasma formation.

E. Plasma Sound Source: A New Mechanism

In cases where the mean laser energy density is greater than the threshold of 11 MJ/m^2, such as in case 3, avalanche ionization will be simultaneous. The sequence of events is expected to be as follows. In the initial plasma buildup period ($t < t_{oa}$), laser energy will be absorbed by the water column within the laser beam, down to a depth determined by the absorption coefficient. At the end of the buildup period ($t = t_{oa}$), a thin surface layer will achieve plasma cutoff. A few picoseconds later ($t_{oa} < t < t_{oa} + t_{ob}$) the plasma in this layer will achieve population inversion and begin to radiate energy. Subsequent laser energy

112

arrivals will be absorbed and concentrated in this layer causing an explosive reaction. The shock wave produced is estimated to be strong enough to significantly compress the adjacent water layer beneath and raise its plasma density to the cutoff level by virtue of the reduction in volume. With the reradiated energy from the first ionized layer, the adjacent layer will also go through a similar process of population inversion, energy reradiation, and explosive expansion. The explosive expansion will add energy to the shock front. Therefore, the shock wave is amplified as it propagates vertically downwards through the energized medium. Similar reactions, in which a population inversion wave is preceded by a shock front, are known to form the basic mechanism of certain types of lasers.[46] The effect is also similar to that of a detonation wave traveling vertically downwards through a shaped charge; here, the energized water column functions as the shaped charge. The acoustic effect would be similar to that of an endfire array directed vertically downward. It is speculated that this mechanism will adequately account for the extraordinary acoustic output measured, as shown in Fig. 24, at the laser energy density of 14 MJ/m^2. It is probable that the process may be modeled as an equilibrium blast in which the energy transfer mechanism is not thermal conduction, but secondary emission. The secondary emission is likely to be coherent with the incident laser energy, and therefore the underwater front will be guided along the laser beam. This appears to be a new mechanism of optoacoustic sound generation.

There are a number of observations that tend to support the new mechanism hypothesized here. First of all, the photoconductivity measurements, at the very minimum, indicate that laser excitation of water produces more charge carriers than that expected from simple heating, and that the carriers are quite different from the proton carriers normally found in water. The results suggest the possibility of electron plasma generation through a buildup process. Therefore, electron plasma interactions, rather than dielectric breakdown, are the suggested mechanism for initiating the explosive reaction at the water surface; plasma formation here is taken to mean the liberation of electrons, while dielectric breakdown is the breaking of the O-H bonds.

Observations of the surface ripples show a plume at 14 MJ/m^2, as in Fig. 23, which is characteristic of a strong downward impulse; this tends to support the hypothesis of a vertically directed detonation wave. This contrasts with observations at 1 MJ/m^2 which do not show any plume, as in Fig. 22.

At 14 MJ/m^2, a few photographs of the surface show a luminescent trail indicative of a narrow plasma column penetrating into the water, as shown in Fig. 37. It is not possible to determine from this photograph if the plasma column ignited spontaneously at all points or propagated into the water behind a shock front as postulated above. The acoustic signal directivity may be used to help resolve this ambiguity. Comparing the acoustic signal spectra from various angles, as shown in Fig. 31, it is seen that the spectrum is strongest in the vertical direction, particularly around a frequency of 100 kHz. This suggests a source that behaves as a vertical endfire array whose length is comparable to the acoustic wavelength at 100 kHz. If, in contrast, the plasma ignited spontaneously everywhere in the column, it would have the characteristics of a vertical broadside line array; this model is mathematically similar to the thermoacoustic model. Calculations for the vertical broadside line array show the acoustic energy spectra peaking in a near-horizontal direction, as shown in Fig. 47, which is quite the opposite of the observed directivity as shown in Fig. 31. Thus, the photoconduction, photographic, and acoustic data all appear to be consistent with the new mechanism hypothesized.

The theory of Kranzer and Keller[32] was used to obtain a relationship between the ripple structure and the vertical impact of the laser blast. An optical model of the photographic imaging system was constructed to relate the ripple structure to the observed grid deformations. Thus, the photographic image may be inverted to give an estimate of the magnitude of the vertical impulse and the depth of the central impact crater. Using the wave theory of Kranzer and Keller to fit the grid deformations observed in Fig. 37, the impact crater was found to be long and narrow. The optical model reconstruction of the grid image and impact crater is shown in Fig. 48. This result is also consistent with the hypothesis of a vertical plasma column penetrating into the liquid behind a
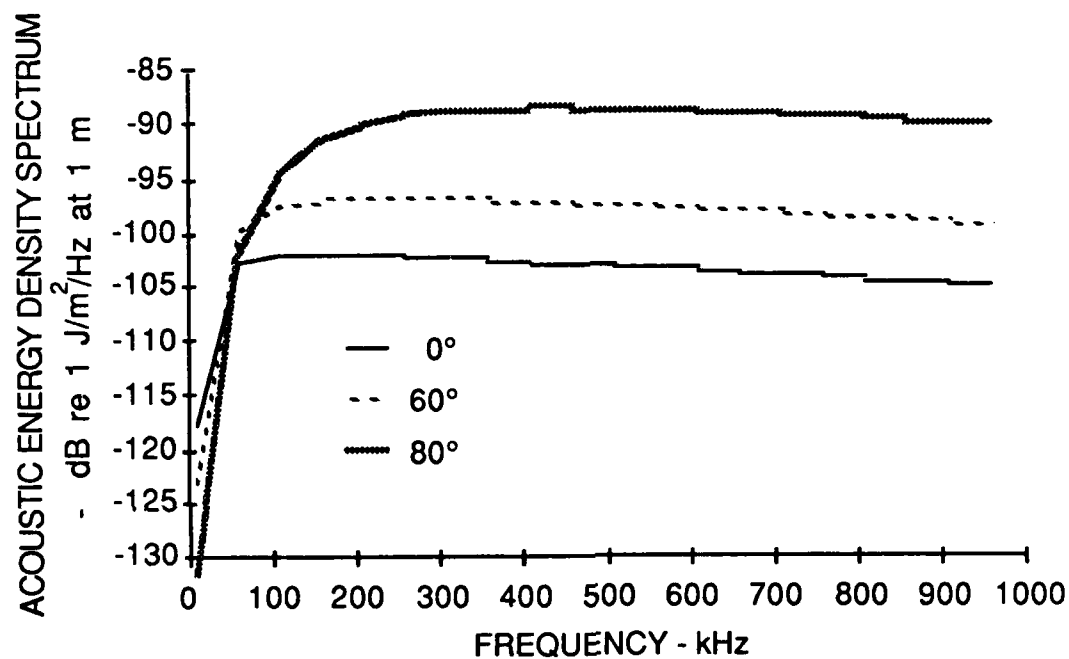
FIGURE 47
CALCULATED ACOUSTIC ENERGY DENSITY SPECTRA
FOR A SPONTANEOUS PLASMA COLUMN
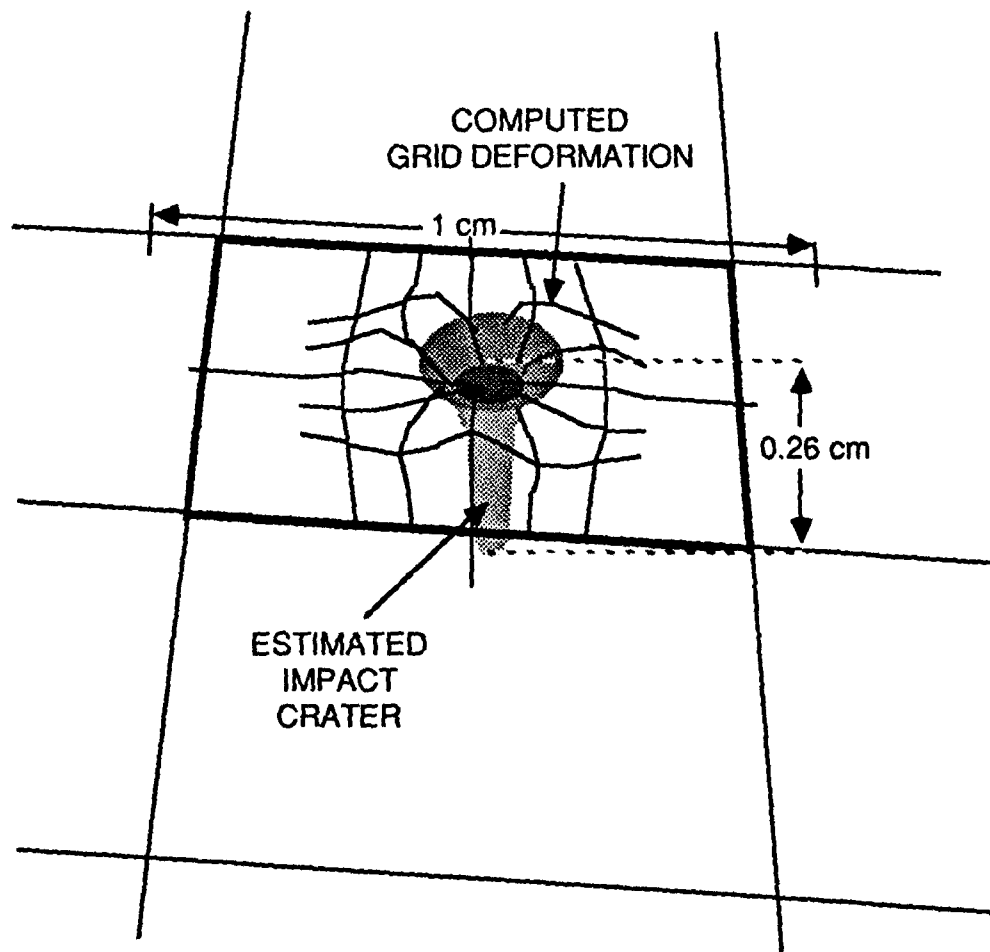
FIGURE 48
COMPUTED IMPACT CRATER AT 0.8 ms
TO FIT THE GRID DEFORMATION IN Fig. 37

shock front. From the photograph, it appears that the penetration of the plasma column is significantly deeper than the depth of the theoretically estimated impact crater.

The new mechanism is different from existing theories because it requires neither a direct dielectric breakdown of the medium nor vigorous evaporation through the direct conversion of laser energy into heat to account for the sudden generation and release of mechanical energy from within a small volume. Although plasmas have been observed in connection with the laser generation of sound in water, they have always been considered as a by-product of the superheating of water. Here, it is postulated that the plasma is an essential part of the mechanism. This new mechanism does not replace the blast model. It is in fact a new variation of the equilibrium blast model in which heat transfer is not conduction limited but secondary emission limited. The conduction limited model is still expected to be valid in many cases, particularly in the case of optoacoustic generation using CO_2 lasers where the absorption coefficient is high enough that direct boiling of the water will be the dominant process.

A new mechanism of optoacoustic generation of sound is put forward. It is only a hypothesis at this stage. It is based on a number of postulates that remain to be proven. All the results obtained appear to support the hypothesis, but more direct and rigorous experimental proofs are needed.

V. CONCLUSIONS

The objective of this study has been to investigate nonlinear optoacoustic generation processes. The initiative for this project arose out of the findings from a previous ONR funded project on the thermoacoustic sound source. While it was found that the thermoacoustic sound source was excessively inefficient, the nonlinear optoacoustic sound source appeared to have some potential as a noncontact underwater acoustic projector. The nonlinear processes are a collection of processes by which a high intensity laser pulse is explosively converted into sound waves. Due to their explosive nature, many aspects of blast theory are applicable.

Work had been initiated under the previous contract to model the blast process at the air-water interface. The validity of this initial model was limited to relatively low laser energy densities where the acoustic propagation could be assumed to be linear. In the present project, a new model was developed which could be coupled to nonlinear acoustic propagation theories. The new model is called the equilibrium blast model. As the name implies, it is based on the hydrodynamic equations of equilibrium. The conditions at the shock fronts are determined by the maximum entropy condition. The distribution of energy within the blast is assumed to be through thermal conduction. Experiments were carried out to test the model, and the model was also compared with published experimental data by Maccabee and Bell. Comparison of the theoretical and experimental data showed that more than one process was involved. So far, three distinct blast processes have been identified, the weak blast, the thermal conduction limited equilibrium blast, and the emission limited equilibrium blast. The model developed in this project pertains to the second process. The first process is thought to be a corruption of the equilibrium blast process in cases where there is not enough intensity to fully develop the equilibrium blast. The third is a new process that had not been anticipated; it was discovered by experiment. The processes occupy mutually exclusive regimes in intensity-energy density space, as mapped in Fig. 49. The boundaries shown are estimates based on theoretical analyses and experimental results obtained at the locations indicated on the map. The

119
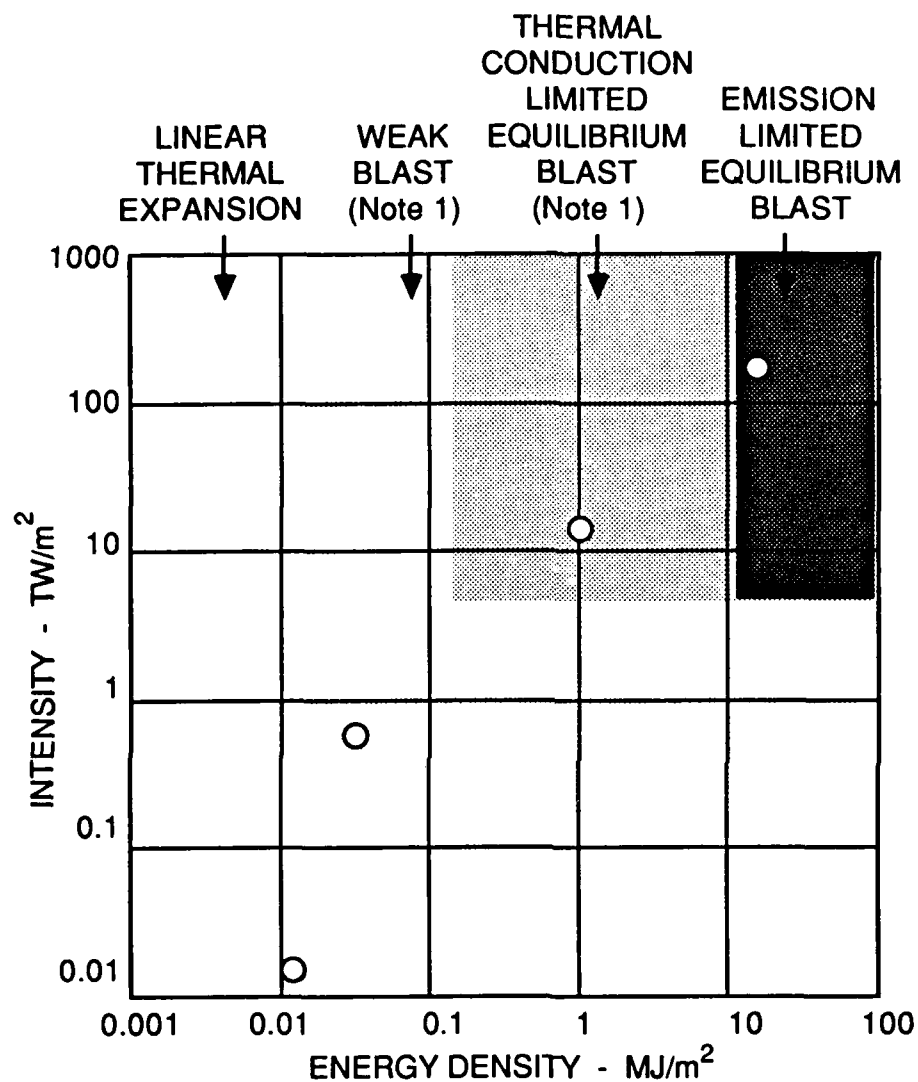
O   LOCATIONS OF OUR EXPERIMENTAL DATA POINTS

Note 1 : Threshold boundaries are dependent on the spot size.
The boundaries shown are for spot diameters in the region of 1 mm

FIGURE 49
OPTOACOUSTIC PROCESSES AT A WAVELENGTH OF 1.06μ

boundary between the weak blast and the equilibrium blast is a rather fuzzy one that is determined by the laser spot size, and possibly certain other equipment specific factors. The diagram also shows that the results obtained so far only represent a single cut through the various regimes.

It was deduced from the experimental results that an essential ingredient of the equilibrium blast processes is plasma formation and subsequent avalanche ionization. To investigate the process of plasma formation, a simple experiment was carried out to study the ionization of water in the presence of laser illumination. Extrapolation of the results indicates that plasma generation and avalanche ionization through a build-up process are plausible. Through the examination of laser induced breakdown data from several sources, a semi-empirical model of the probability of avalanche ionization was formulated. It was concluded that electron plasma interactions, rather than dielectric breakdown, is the more likely mechanism for initiating the explosive reaction at the water surface; plasma formation here refers to the liberation of electrons, while dielectric breakdown is normally taken to mean the breaking of the molecular bonds, in this case O-H bonds.

The emission limited equilibrium blast regime was not anticipated but was discovered experimentally. It is a regime that is deserving of further study from a basic physics point of view and from an applications standpoint. From a basic physics point of view, it is interesting because it probably involves an electronic process of shock wave generation and amplification, rather than the better known hydro- or thermodynamic processes. The acoustic shock wave appears to draw its energy from a plasma column. From the applications standpoint, it appears to be the most efficient of all four optoacoustic generation processes identified. Furthermore, it has the potential to be tuned. The length of the plasma column is expected to control the time constant or resonance frequency of the shock pulse. Thus, the frequency content of the acoustic output may be controlled through the length of the plasma column. In practice, this may be achieved through the proper selection of a laser wavelength with the appropriate absorption coefficient.

Our experimental results of the emission limited equilibrium blast show acoustic spectrum levels over 50 dB greater than that predicted by the thermoacoustic model and, in the region of the spectral peak around 50 kHz, 30 dB higher than that predicted by the conduction limited blast model. With a laser energy of only 0.7 J, the experimental results showed a measured acoustic source level of 200 dB re 1 μPa at 1 m, in the band from 10 to 200 kHz. While the source level is similar to results obtained by Maccabee and Bell with a CO_2 laser of a larger beamwidth, the CO_2 laser data were found to have a spectral peak at a higher frequency of 185 kHz. A spectral peak at 50 kHz makes this mechanism attractive as a potential sonar source. The prospect of being able to control the frequency through the length of the plasma column and perhaps achieving even lower frequencies is worth further investigation. For these reasons, the emission limited blast is potentially able to deliver a breakthrough in optoacoustic sound generation for sonar applications.

APPENDIX I

DATA PROCESSING SOFTWARE

The steps used in processing the data from the experiment are outlined in Fig. 50. All programs were written in FORTRAN and executed on a CYBER 830 computer. Experimental data were collected by a Nicolet 4094A oscilloscope and stored on disk. The data interface program allowed for the transfer of the data from the Nicolet to the CYBER in an integer format. This file was then normalized through the use of a normalization program and output in a floating point format. The floating point data are then processed using a compensation program. The program compensates the data by removing the transfer function of the recording equipment. The gain and phase response of the equipment was measured as a function of frequency using the Nicolet oscilloscope and a variable oscillator. Amplifier and filter effects as well as hydrophone sensitivities were included in the response function. The output of the compensation program is the estimated time history of the acoustic pressure. Finally, the acoustic spectrum estimation program produces a spectral density of the acoustic energy density. Both the pressure signal and the spectrum may be plotted.
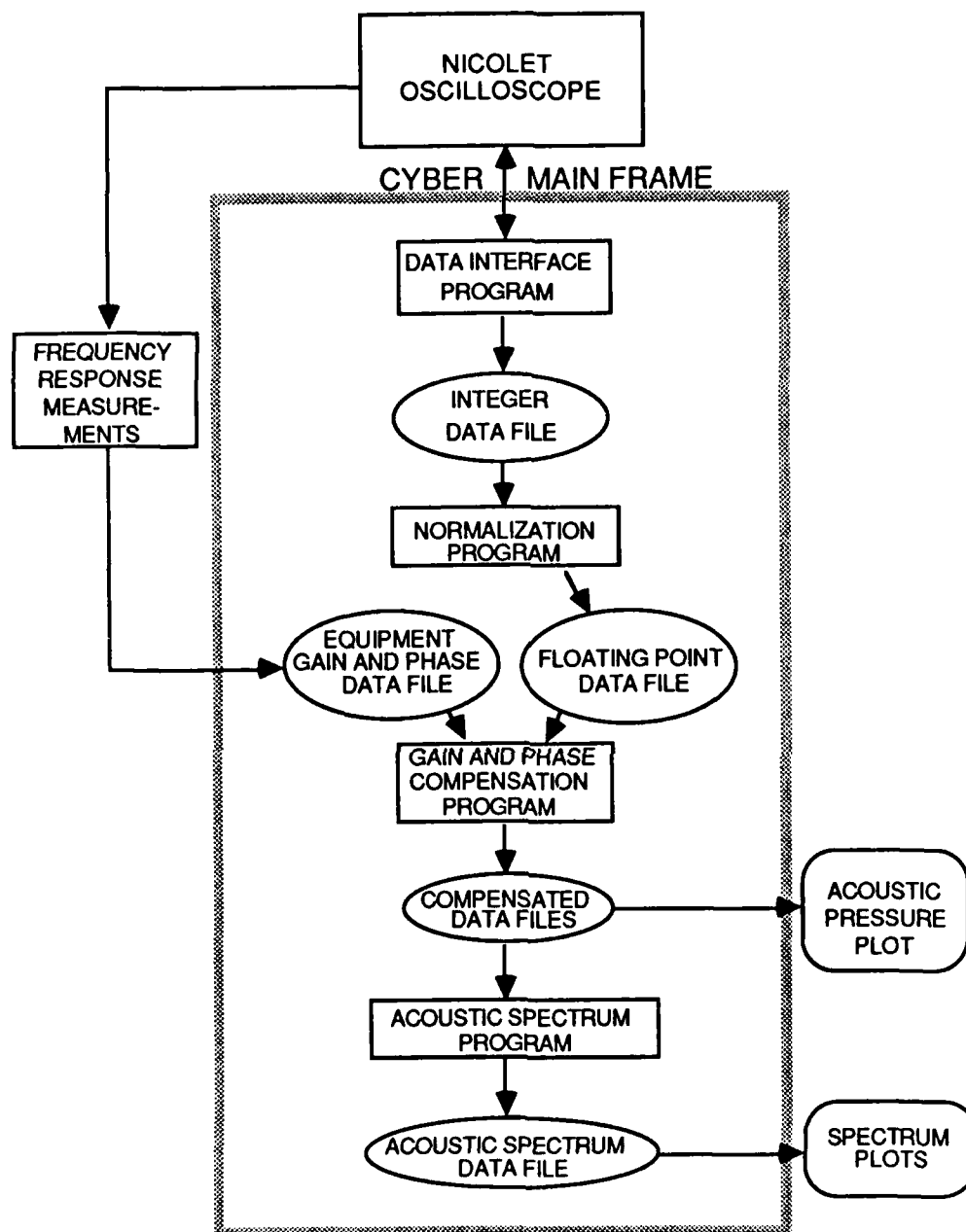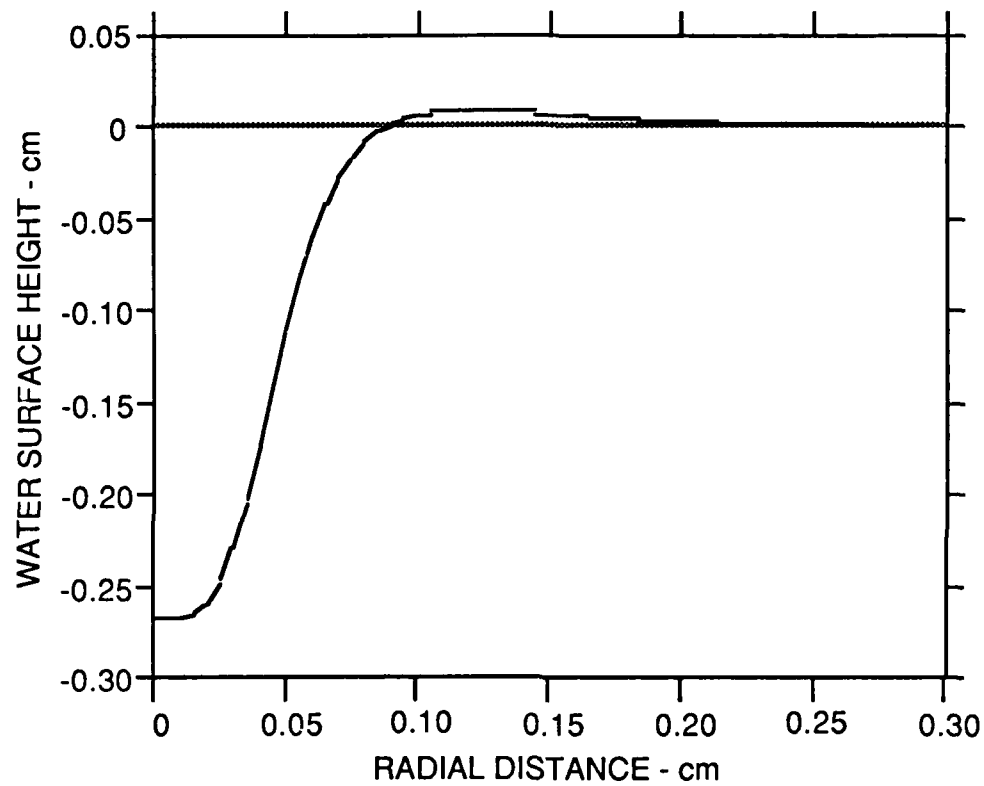
FIGURE 50
DATA PROCESSING FLOWCHART

APPENDIX II

SURFACE DEFORMATION ESTIMATION

Photographic images of the water surface deformation were recorded. A diagram of the photographic apparatus is shown in Fig. 14. The tubing was designed to position the upper and lower lenses for the laser beam as well as to align the camera and the grid imaging lenses. A stroboscope illuminated a grid pattern which was projected onto the water surface. A timing circuit was used to control the time delay between the laser pulse and the flash pulse of the stroboscope. The photographs obtained show a deformation of the grid pattern, which indirectly reflects the deformation of the water surface. A modeling process was undertaken to gain a better understanding of the photographic images observed. The purpose of the model was to numerically simulate the photographic image so that a relationship might be established between the photographic image and the actual surface deformation.

Light rays originating from points on the grid were traced through the first imaging lens to their image points on the water surface, reflected from the water surface, and finally traced through the camera lens onto the final image on the film. The origin of the coordinate system was fixed at the intersection of the grid and the ray that passes through the center of the first imaging lens to the intersection of the laser beam axis and the undisturbed water surface. Basic vector calculus methods were used to trace the incident and reflected rays. The apertures of the lens determined the visibility of each ray.

The equations of Kranzer and Keller[32] were used to model the surface disturbance. Cylindrical symmetry was assumed about the axis of the laser beam. In the case of the results shown in Fig. 48, the process was modeled as a Gaussian shaded impulse. The magnitude of the impulse was adjusted to obtain an image which matched the grid distortions observed in the photographic image. The result was a surface deformation, at a time delay of 0.8 ms, consisting of a bore hole 0.26 cm deep surrounded by a single ripple with a peak height of 0.009 cm at a radius of 0.115 cm. The disturbance decays to zero at a radial distance of 0.675 cm. The profile is shown in Fig. 51.

129

FIGURE 51
ESTIMATED SURFACE RIPPLE PROFILE AT 0.8 ms

REFERENCES

1. L. M. Lyamshev and L. V. Sedov, "Optical Generation of Sound in a Liquid: Thermal Mechanism (Review)," Sov. Phys.-Acoust. 27(1), 4-18 (1981).

2. Y. H. Berthelot, "Generation of Underwater Sound by a Moving High-Power Laser Source," Applied Research Laboratories Technical Report No. 85-21 (ARL-TR-85-21), Applied Research Laboratories, The University of Texas at Austin , 1 August 1985.

3. N. P. Chotiros, "The Moving Thermoacoustic Array: A Theoretical Feasibility Study," Applied Research Laboratories Technical Report No. 85-3 (ARL-TR-85-3), Applied Research Laboratories, The University of Texas at Austin, 17 January 1985.

4. N. P. Chotiros, Ilene J. Busch-Vishniac, and Y. H. Berthelot, "The Moving Thermoacoustic Array, Final Report under Contract N00014-82-K-0425," Applied Research Laboratories Technical Report No. 86-12 (ARL-TR-86-12), Applied Research Laboratories, The University of Texas at Austin, 25 July 1986.

5. L. M. Lyamshev and K. A. Naugolnikh, "Optical Generation of Sound: Nonlinear Effects (Review)," Sov. Phys.-Acoust. 27(5) (1981).

6. D. C. Emmony, B. M. Geerken, and A. Straaijer, "The Interaction of 10.6 μm Laser Radiation with Liquids," in Infrared Physics 16, 87-92 (1976).

7. E. F. Carome, C. E. Moeller, and N. A. Clark, "Intense Ruby-Laser-Induced Acoustic Impulses in Liquids," J. Acoust. Soc. Am. 40(6), 1462-1466 (1966).

8. G. D. Hickman and J. A. Edmonds, "Laser-Acoustic Measurement for Remotely Determining Bathymetry in Shallow Turbid Waters," J. Acoust. Soc. Am. 73(3),840-843 (1983).

9. C. E. Bell and B. S. Maccabee, "Shock Wave Generation in Air and Water by CO_2 TEA Laser Radiation," Applied Optics 13(3), 605-609 (1974).

10. B. S. Maccabee and C. E. Bell, "Acoustic Pressure Scaling of Laser Induced Sound", NSWC TR 82-122, Naval Surface Weapons Center, Silver Spring, Maryland, 1982.

11. B. S. Maccabee and C. E. Bell, NSWC TR 83-130, Naval Surface Weapons Center, Silver Spring, Maryland, 1983.

12. B. S. Maccabee and C. E. Bell, "Experimental Study of Laser-Induced Underwater Sound," J. Acoust. Soc. Am. S103, 77 (1985).

13. A. N. Pirri, R. Schlier, and D. Northam, "Momentum Transfer and Plasma Formation above a Surface with a High-Power Laser," Appl. Phys., Lett., 21, No. 3, 79-81 (1972).

14. A. N. Pirri, "Theory for Momentum Transfer to a Surface with a High-Power Laser," Phys. Fluids 16, 1435 (1973).

15. C. J. Knight, "Theoretical Modeling of Rapid Surface Vaporization with Back Pressure," J. AIAA 17, No. 5, 519-523 (1979).

16. P. K. Wu, "Radiation Induced Acoustic Waves in Water," J. AIAA 15, No. 12, 1809-1811 (1977).

17. L. M. Lyamshev and K. A. Naugol'nykh, "Optical Sound Generation," Sov. Phys.-Acoust. 26(4), 351-353 (1980).

18. F. D. Feiock and L. K. Goodwin, "Calculation of Laser-Induced Stresses in Water," J. Appl. Phys. 43, No. 12, 5061-5064 (1972).

19. M. W. Sigrist and F. K. Kneubuhl, "Laser-Generated Stress Waves in Liquids," J. Acoust. Soc. Am. 64(6), 1652-1663 (1978).

20. C. L. Hu, "Spherical Model of an Acoustical Wave Generated by Rapid Laser Heating in a Liquid," J. Acoust. Soc. Am. 46(3) (Part 2), 728-736 (1969).

21. T. G. Muir, C. R. Culbertson, and J. R. Clynch, "Experiments on Thermoacoustic Arrays with Laser Excitation," J. Acoust. Soc. Am. 59, 735-743 (1976).

22. N. P. Chotiros, "Preliminary Study of Nonlinear Sound Generation Processes," Applied Research Laboratories Technical Report No. 86-11 (ARL-TR-86-11), Applied Research Laboratories, The University of Texas at Austin, 12 August 1986.

23. Yu. P. Raizer, "Heating of a Gas by a Powerful Light Pulse," Sov. Phys. JETP 21, No. 5 (1965).

24. R. H. Cole, Underwater Explosions (Princeton University Press, Princeton, New Jersey, 1948).

25. D. L. Chapman, Phil. Mag. (5), 47-90 (1899).

26. E. Jouguet, Comptes Rendus 132, 673 (1901); J. De Math (Liouville) 6, II, 5 (1905-6).

27. Handbook of Chemistry and Physics, 59th ed.,1978-1979 (The Chemical Rubber Company Press, West Palm Beach, Florida, 1978).

28. R. W. Haywood, Thermodynamic Tables in SI (Metric) Units (Cambridge University Press, Cambridge, ENGLAND, 1968).

29. S. Ramo, J. R. Whinnery, and T. van Duzer, Fields and Waves in Communication Electronics (John Wiley and Sons, New York, 1965).

30. W. R. Smythe, Static and Dynamic Electricity (McGraw-Hill Book Co., Inc., New York, 1950).

31. P. H. Rogers, "Weak-Shock Solution for Underwater Explosive Shock Waves," J. Acoust. Soc. Am. 62(6), 1412-1419 (1977).

32. H. C. Kranzer and J. B. Keller, "Water Waves Produced by Explosions," J. Appl. Phys. 30, No. 3, 398-407 (1959).

33. L. H. van Vlack, Materials Science for Engineers (Addison-Wesley, London, 1970).

34. P. M. Morse and K. U. Ingard, Theoretical Acoustics (McGraw-Hill Book Co., Inc., New York, 1968).

35. J. D. Bernal and R. H. Fowler, "A Theory of Water and Ionic Solution, with Particular Reference to Hydrogen and Hydroxyl Ions," J. Chem. Phys. 1, No. 8, 515-548 (1933).

36. F. F. Chen, <u>Plasma Physics and Controlled Fusion</u>, Vol. 1: Plasma Physics, 2nd ed. (Plenum Press, New York, 1984).

37. A. H. Beck and H. Ahmed, <u>An Introduction to Physical Electronics</u> (Edward Arnold, London, 1968).

38. M. Bass and H. H. Barrett, "Avalanche Breakdown and the Probabilistic Nature of Laser Induced Damage," IEEE J. Quant. Electron. <u>QE-8</u>, 338-343 (1972).

39. D. W. Fradin, E. Yablonovitch, and M. Bass, "Confirmation of an Electron Avalanche Causing Laser-Induced Bulk Damage at 1.06μ," Appl. Opt. <u>12</u>, 700-709 (1973).

40. M. Bass and D. W. Fradin, "Surface and Bulk Laser Damage Statistics and the Identification of Intrinsic Breakdown Processes," IEEE J. Quant. Electron. <u>QE-9</u>, 890-896 (1973).

41. H. Schmidt-Kloiber and E. Reichel, "Die Abhängigkeit der Druckamplitude einer Stossewelle von der Feldstärke beim Laserinduzierten Durchbruch in Flüssigkeiten," Acustica <u>54</u>, 284-288 (1984).

42. M. A. Mainster, D. H. Sliney, C. D. Belcher III, and S. M. Buzney, "Laser Photodisruptors - Damage Mechanisms, Instrument Design and Safety," Ophthalmology <u>90</u>, 973-991 (1983).

43. H. P. Lörtscher, "Laser-Induced Breakdown for Ophthalmic Microsurgery," in S. Srokel, <u>YAG Laser Ophthalmic Microsurgery</u> (Appleton Century Croft, Norwalk, 1983), Ch. 4, pp. 39-66.

44. V. N. Pozhidaev and A. I. Fatievskii, "Optical Breakdown Thresholds in Liquid Water and Microsize Water Droplets," Sov. J. Quant. Electron. <u>11</u>, 56-68 (1981).

45. F. Docchio, L. Dossi, and C. A. Sacchi, "Q-switching Nd:YAG Laser Irradiation of the Eye and Related Phenomena: An Experimental Study. I. Optical Breakdown Determination for Liquids and Membranes," Lasers in Life Sciences, to be published.

46. B. L. Borovich, V.S. Zuev, V. A. Katulin, V. Yu. Nosach, O. Yu. Nosach, A. V. Startsev, and Yu. Yu. Stoilov, "Characteristics of Iodine Laser Short Pulse Amplifier," Sov. J. Quant. Electron. <u>5</u>, No. 6, 697-703 (1976).

DISTRIBUTION LIST FOR
ARL-TR-88-1
FINAL REPORT UNDER CONTRACT N00014-86-K-0176

<u>Copy No.</u>

Office of the Chief of Naval Research
Department of the Navy
Arlington, VA 22217-5000
1 - 2   Attn: M. Blizard, Code 1125
3   R. Fitzgerald, Code 1125AO
4   R. Obrochta, Code 1125AR

Commanding Officer
Naval Research Laboratory
Washington, DC 20375
5 - 10   Attn: Code 2627

Director
Naval Surface Warfare Center
White Oak Laboratory
Silver Spring, MD 20903-5000
11   Attn: B. Maccabee

12 - 23   Commanding Officer and Director
Defense Technical Information Center
Bldg. 5, Cameron Station
5010 Duke Street
Alexandria, VA 22314

Department of Mechanical Engineering
Georgia Institute of Technology
Atlanta, GA 30332
24   Attn: P. Rogers

Department of Mechanical Engineering
The University of Texas at Austin
Austin, TX 78712
25   Attn: I. Busch-Vishniac

	Center for Fast Kinetics Research The University of Texas at Austin Austin, TX 78712
26	Attn: M. Rodgers
	Electrical and Computer Engineering The University of Texas at Austin Austin, TX 78712
27	Attn: M. Becker
28	Nicholas P. Chotiros, ARL:UT
29	David T. Blackstock, ARL:UT
30	C. Robert Culbertson, ARL:UT
31	Thomas A. Griffy, ARL:UT
32	John M. Huckabay, ARL:UT
33	Library, ARL:UT
34 - 43	Reserve, ARL:UT

END

DATE

FILMED

8-88

DTIC